2021

Synthesis, Crystal Engineering, and Material Properties of Small-Molecule Organic Semiconductors

Emma Holland
University of Kentucky, emkathol13@gmail.com
Digital Object Identifier: https://doi.org/10.13023/etd.2021.323

Right click to open a feedback form in a new tab to let us know how this document benefits you.

SYNTHESIS, CRYSTAL ENGINEERING, AND MATERIAL PROPERTIES OF
SMALL-MOLECULE ORGANIC SEMICONDUCTORS

_____

DISSERTATION
_____

A dissertation submitted in partial fulfillment of the
requirements for the degree of Doctor of Philosophy in the
College of Arts and Sciences
at the University of Kentucky

By

Emma Katherine Holland

Lexington, Kentucky

Director: Dr. John E. Anthony, Professor of Chemistry

Lexington, Kentucky

2021

ABSTRACT OF DISSERTATION

SYNTHESIS, CRYSTAL ENGINEERING, AND MATERIAL PROPERTIES OF
SMALL-MOLECULE ORGANIC SEMICONDUCTORS

Small-molecule organic materials are of increasing interest for electronic and photonic devices due to their solution processability and tunability, allowing devices to be fabricated at low temperature on flexible substrates and offering utility in specialized applications. This tunability is the result of functionalization through careful synthetic strategy to influence both material properties and solid-state arrangement, both crucial variables in device applications. Functionalization of a core molecule with various substituents allows the fine-tuning of optical and electronic properties, and functionalization with solubilizing groups allows some degree of control over the solid-state order, or crystal packing. These combinations of core chromophores with varying substituents are systematically evaluated to develop structure-function relationships that can be applied to numerous applications. This is the basis of Chapter 2, which focuses on identifying trends between physical structure and resulting optical and electronic properties in heteroacenes.

In Chapter 3, the chromophores of Chapter 2 are further functionalized with substituents that allow them to work in tandem with inorganic materials for a hybrid singlet fission-triplet harvesting photovoltaic system. Chapter 4 further explores these key chromophores with still other substituents, here for isolated triplet pair generation and eventual quantum computing applications. Finally, Chapter 5 explores a relatively understudied class of formally antiaromatic compounds, the octadehydro[12]annulenes, demonstrating a unique effort at crystal engineering these molecules using similar strategies as in Chapter 2. A comprehensive overview of the physical, optical, and electronic properties is offered, providing a robust basis for future work.

KEYWORDS: Organic materials, semiconductors, synthesis, acenes, crystal engineering

Emma Katherine Holland

July 31, 2021

SYNTHESIS, CRYSTAL ENGINEERING, AND MATERIAL PROPERTIES OF
SMALL-MOLECULE ORGANIC SEMICONDUCTORS

By
Emma Katherine Holland

John E. Anthony
Director of Dissertation

Yinan Wei
Director of Graduate Studies

July 31, 2021
Date

ACKNOWLEDGEMENTS

TABLE OF CONTENTS

LIST OF TABLES

LIST OF FIGURES

LIST OF ABBREVIATIONS

Å – Angstrom
ADT – Anthradithiophene
BDHA – Benzodehydroannulene
BTI - (bis(trifluoroacetoxy)iodo)benzene
BuLi – Butyllithium
C_8-BTBT – 2,7-dioctyl-benzothioenobenzothiophene
CB – Conduction band
CIF – Crystallographic information file
COOH – Carboxylic acid
DCE – 1,2-Dichloroethane
DCM – Dichloromethane
DFT – Density functional theory
DHA – Dehydroannulene
DIBAL-H – Di(isobutyl)aluminum hydride
diox – Dioxolane
ET – Electron transfer
EtOAc – Ethyl acetate
FA – Furanoanthracene
FAQ – Furanoanthracene quinone
FTA – Fluorothienoanthracene
FTDA – Fluorothiophene dialdehyde
GC – Gas chromatography
GCMS – Gas chromatography mass spectrometry
HOMO – Highest occupied molecular orbital
IPD – Interplanar distance
LUMO – Lowest occupied molecular orbital
M – Molar
MALDI – Matrix assisted laser desorption ionization
MeI- Methyl iodide, also called iodomethane
MeOH – Methanol
MOE – Methoxyethyl
MOM – Methoxymethyl
MOO – Methoxyoctyl
MS – Mass spectrometry
NICS – Nucleus independent chemical shift
nm - Nanometer
NMR – Nuclear magnetic resonance
OFET – Organic field effect transistor
OPV – Organic photovoltaic
OSC – Organic semiconductor
PCE – Power conversion efficiency
PLQE – Photoluminescence quantum efficiency
Pn – Pentacene
PV – Photovoltaic

QD – Quantum dot
RT – Room temperature
SF – Singlet fission
SQ – Shockley Queisser
TA – Thienoanthracene
TAQ – Thienoanthracene quinone
TDA – Thiophene dialdehyde
THF – Tetrahydrofuran
TLC – Thin layer chromatography
TMS – Trimethylsilyl
TBDMS – Tert-butyl dimethylsilyl
TBDPS – Tert-butyl diphenylsilyl
TES – Triethylsilyl
TiPS – Tri(isopropyl)silyl
TiBS – Tri(isobutyl)silyl
V_{if} – Electronic coupling
VB – Valence band
XRD – X-ray diffraction
μ – Charge carrier mobility
μM – Micromolar
4F – Tetrafluoro

Chapter 1: Introduction

<u>1.1: Preface</u>

As the basis of all modern electronics, semiconducting materials are of great importance. Silicon is the most commonly employed material for semiconductors, offering exceptional performance and well-established fabrication methods; however, production of silicon-based semiconductors is energy-intensive and requires significant capital investment.[1] Organic semiconductors (OSCs) offer an interesting alternative that has received much attention in both academic research and industrial development. Semiconductors composed of organic materials allow for the possibility of low-temperature solution processing, permitting the devices to be fabricated on substrates that are lightweight and flexible; inorganic semiconductors typically require high-temperature processing steps which often precludes the usage of these flexible substrates.[2] This offers the exciting possibility for applications such as wearable electronic devices and flexible electrodes that can serve in niche applications where incredibly high performance is not required.[3] Further, organic materials can be structurally modified using ever-improving synthetic techniques, allowing the possibility for precise tuning of material properties for specialized applications.[4]

However, organic materials do not exhibit the same charge carrier mobilities as silicon and other inorganic materials. The charge carrier mobility (μ) of crystalline silicon is commonly reported to be over 1000 cm^2/Vs (though mobility is on the order of 1 cm^2/Vs for amorphous silicon),[5] whereas the current top solution-processed OSC materials exhibit mobility values on the order of 1 to 10 cm^2/Vs.[6] While not nearly at the level of crystalline silicon, this is a significant improvement from just twenty years ago, when a mobility of 0.1 cm^2/Vs was considered an exceptional result,[7] showing the rapid development of the field. This improvement is due largely to a combination of synthetic efforts, allowing the production of more varied organic materials, and of the advancement of device fabrication strategies, allowing the best performance possible to be obtained from a given material.

Given these efforts over the past several decades, the field of organic electronic devices has developed significantly, with some materials commercially available.[8] In order for organic devices to find a place in widespread commercial use, performance and

stability must continuously improve, while costs must be lowered and processing simplified and scaled. Replacing silicon is not the goal of organic semiconductors, but rather applying OSCs in niche applications where the high performance of silicon is not required, and instead the processability and tunability of organics can shine. Organic semiconductors are continuously improving, thanks to the efforts of synthetic chemists, device engineers, and physicists collaborating to develop better materials and device fabrication strategies, along with further elucidating the structure-function relationships behind efficient semiconductor performance.

1.2: Solid-State Order in Organic Molecules

Despite the great progress in the realm of OSC materials, predicting a molecule's performance in a device has proven difficult, and the best method to evaluate a material remains synthesizing the compound and fabricating devices. This process is time-consuming and often repetitive; however, there are several indicators that a compound is likely to offer effective device performance that can be evaluated prior to device fabrication and testing. Using simple and scalable synthetic routes allows derivatives to be synthesized and screened relatively rapidly.

The first of these is crystal packing, the arrangement of individual molecules in the solid state. This arrangement is crucial to electronic performance, as the crystalline order may allow or disallow charges to be transported across an organic material. For inorganic semiconductors such as silicon, strong covalent bonds bind atoms and allow electron delocalization throughout the material, which in turn permits the high charge carrier mobility observed in these materials. However, in organic solids, which are bound by weak van der Waals forces, charge transport is dependent on delocalized electrons in a π-system interacting with those in adjacent molecules. In order for a charge to move from one molecule to an adjacent one, there must be some overlap between the π-surfaces of these molecules, typically in a face-to-face or edge-to-face manner as shown in Figure 1.1. The ability of charges to move across an edge-to-edge interaction, as in 1.1(d), has also been computationally predicted. Though edge-to-edge is typically not as strong an interaction as the face-to-face or edge-to-face orientations, the edge-to-edge relationship is still predicted to be a valid charge transport pathway.[9]
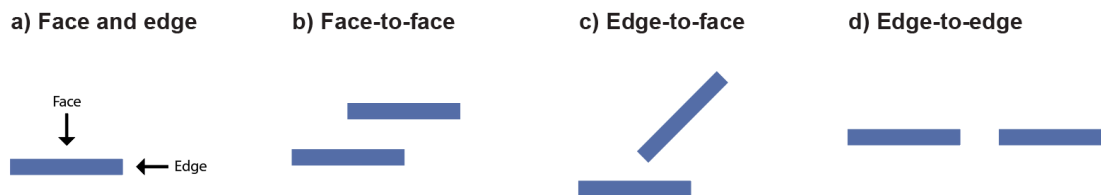
Figure 1.1: (a) Face and edge of a material and (b)-(d) possible π-surface interactions.

This ability to transport charge is not dictated solely by physical proximity; the molecular orbitals must also be in phase. Generally good overlap of the π-surfaces is indicative of strong electronic coupling, but some exceptions to this exist.[10] The true degree of "π-stacking" is a combination of physical overlap and the phase relationship between the frontier orbitals of the molecules, termed electronic coupling, and is highly dependent on solid state ordering, or how the molecule packs in the crystal. As shown in Figure 1.2(a), the transfer integral (which is the degree of electronic coupling between two molecules, denoted here by t) decreases as a function of distance between molecules (interplanar distance); an increase in distance by fractions of an angstrom can decrease the degree of coupling by a significant amount.[11] Note that electronic coupling is commonly represented by V_{if}, as described by the equation for the rate constant (k_{if}) shown in Figure 1.2(c) which is derived from Marcus theory.[12] This equation describes the hopping mechanism of charge transport through successive electron transfer reactions, where the rate of transfer is affected by several variables including the degree of electronic coupling, V_{if}, which is strongly influenced by crystal packing, as well as the Gibbs free energy term (ΔG^0) and the reorganization energy λ. The arrangement of molecules in the crystal determines intermolecular distances and long and short axis displacement, the combination of which dictates the orbital phase overlap, shown in Figure 1.2(b). As such, the crystal packing motif of a material can be related to Marcus Theory and electronic performance, and tuning molecular structure can greatly impact the crystal packing.[13] Building up these structure-function relationships, determining the relationship between a structural change and its resulting crystal packing result, is crucial towards broadening our understanding of the delicate interplay between OSC materials and their performance.

3
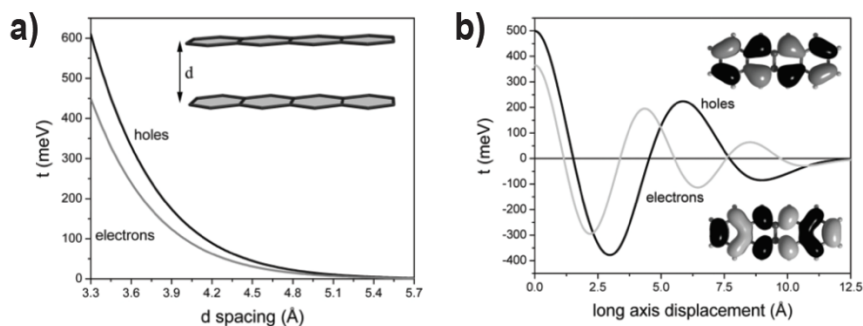
c) Rate of electron transfer:

$$k_{if} = \frac{2\pi}{\hbar} |V_{if}|^2 \sqrt{\frac{1}{4\pi k_B T \lambda}} e^{\frac{-(\Delta G^0 + \lambda)^2}{4 k_B T \lambda}}$$

Figure 1.2: (a) Relationship of electronic coupling to interplanar distance, (b) electronic coupling with long axis displacement, (c) equation for rate constant of electron transfer from Marcus Theory. (a) and (b) are reprinted with permission from reference 11, copyright 2007 American Chemical Society.

There are several types of intermolecular arrangements, or packing motifs, that can facilitate charge transport. A common example, depicted in Figure 1.3(a), is a herringbone arrangement, in which the delocalized π-orbitals of one molecule are adjacent to the edge of the next.

Figure 1.3: Simple representations of (a) herringbone and (b) brickwork packing motifs.

These two-dimensional layers propagate the edge-to-face interactions throughout the solid. While this motif does typically lead to strong electronic coupling, a brickwork arrangement as shown in Figure 1.3(b) allows for stronger face-to-face π-interactions.[14] These 2D π-stacking motifs allow for strong electronic coupling between adjacent molecules in two directions and typically lead to devices with high mobilities. This can be contrasted with 1D π-stacking, where charges only have one direction in which to diffuse through a material, and the mobilities of materials exhibiting a 1D π-stack are typically lower than their 2D counterparts.[15] A 2D π-stack is thus considered more advantageous

for device applications requiring a high mobility, such as field effect transistors (FETs). One such OSC material that packs in a 2D brickwork motif is 6,13-bis(triisopropylsilylethynyl) pentacene (TIPS Pentacene), first synthesized by Anthony in 2001,[16] the structure and crystal packing of which is shown in Figure 1.4(a) and (b). Anthony and coworkers demonstrated that the two-dimensional π-stacking allows the charges more potential pathways across which they can move, yielding much higher mobilities than observed in 1D π-stacked materials. After significant device processing optimization, mobilities up to 12 cm^2/Vs[17] have been reported for TiPS Pn, demonstrating the importance of collaboration between synthetic chemists and device engineers. Another commonly known small-molecule OSC material is 2,7-diocytl-benzothienobenzothiophene, or C$_8$-BTBT, originally synthesized by Takimiya,[18] which packs in a classic edge-to-face herringbone motif as shown in Figure 1.4(c) and (d) and yields a mobility up to 7-8 cm^2/Vs,[19] depending on device processing method. Both of these champion materials demonstrate the benefit of strong π-surface interactions.
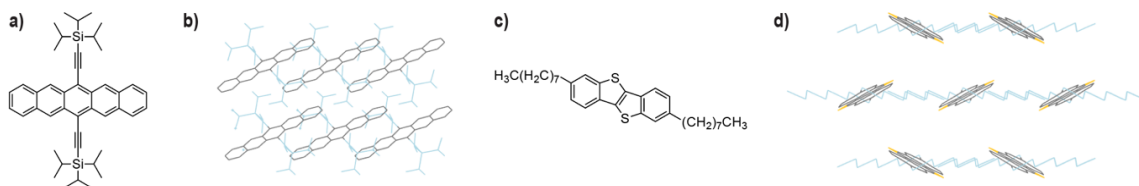
Figure 1.4: (a) Structure of TIPS Pentacene, (b) crystal packing of TiPS Pentacene as viewed down the crystallographic c axis, (c) structure of C$_8$-BTBT, (d) crystal packing of C$_8$-BTBT as viewed down the crystallographic c axis (Obtained from the CCDC Database, CCDC 679293).

Beyond visually evaluating the crystal structure for π-surface overlap, there is a formal definition for so-called "close contacts" in an organic crystal that suggest the possibility for charge transport, where atoms in the π-system are separated by less than the sum of the van der Waals radii for the two atoms involved; thus, a carbon-carbon close contact is present when carbon atoms on adjacent molecules are less than 3.4 Å apart. This is only relevant when discussing atoms that are part of the delocalized π-system,[10] and while there may technically be "close contacts" by definition between the atoms in other parts of the molecule, these are disregarded as they have no bearing on charge transport. Further, charge transport is still possible in systems where the distances between π-systems are greater than 3.4 Å, though a packing motif with formal carbon-carbon close contacts in the π-system is considered ideal.[20]

Optimizing the solid-state order of a core molecule is examined further in the remaining chapters, Chapters 2 and 5 particularly, both of which relate to tuning the crystal packing and maximizing close contacts to offer greater potential for charge transport of a given chromophore, and this principle forms the overall basis of the entirety of this work.

1.3: Material Properties of Organic Semiconductors

An important value for semiconducting materials is the band gap, or the energy difference between the top of the valence and bottom of the conduction bands, and is representative of the energy necessary to generate an electron-hole pair in a material, which is especially relevant to photovoltaics. The band gap may be estimated experimentally through various spectroscopic methods, as it is also somewhat related to the lowest optical transition (known as the optical gap, accessible by absorption of a single photon). The difference between the band gap and the optical gap is a term known as the exciton binding energy, which is typically small (tenths of an eV) in organic semiconductors and nearly negligible in inorganic semiconductor crystals (meV).[21] While the band gap of a material is not directly obtained from the absorption spectrum, trends along both of these phenomena in materials tend to be correlated. For example, along the acene series, there exists a very clear trend in the absorption spectrum: as acene length (number of fused rings) increases, the maximum absorbance red-shifts (moves to longer wavelengths).[22] Similarly, the band gap decreases across the acene series from anthracene to pentacene and higher acenes.[23] Though there is much inconsistency in the literature regarding the terminology used to discuss the band gap of semiconducting materials,[21] it remains a crucial figure of merit, and tuning the band gap of a material is relevant to several device applications, as discussed further in the following sections.

H-aggregate   J-aggregate

Figure 1.5: H- and J-aggregates.

Relating these phenomena back to intermolecular interactions, organic molecules may form aggregates in films or crystals that affect the photophysical properties of these

molecules. These aggregates may take two forms: H-aggregates or J-aggregates, as shown in Figure 1.5. The former is typically present as a sandwich stacked dimer and manifests as a blue-shift (move to shorter wavelengths) in the absorbance spectrum and quenched fluorescence.[24] In a J-aggregate, a head-to-tail orientation is predominant, and there is a red-shift in the absorbance.[25] These types of arrangements are important to take into account when characterizing compounds. Typically, basic photophysical characterization such as absorbance and fluorescence are conducted in solution, while most applications utilize materials in the solid state, whether single crystals or thin films deposited from solution. Solution spectra may be influenced by solvent effects and concentration, while solid-state measurements may be affected by crystalline order or lack thereof. Organic films or crystals may exhibit different polymorphs depending on solvent and deposition or growth method, which may result in variable properties being observed. Both solution and solid-state aspects must be considered to get a full picture of a material's properties.

1.4: Electronic Device Operation and Terminology

This report discusses materials that have the potential for use in several different applications. A brief description of device operation is necessary for context on the motivation for the materials covered in this work.

The key process in electronic devices, organic or inorganic, is the transport of charges, as mentioned in previous sections. The charges may be holes (in p-type devices) or electrons (in n-type devices); the efficiency of charge transport through the material is closely tied to the device's performance. A material's ability to effectively transport charge is dictated by intermolecular interactions in the solid state, as described in Chapter 1.2. Studies demonstrate[26] that very small changes to these intermolecular interactions can lead to dramatically differing device performance; as such, synthetic chemists and device engineers work closely to develop materials with the appropriate intermolecular interactions and to fabricate devices that take full advantage of them.

The first device to be discussed is the transistor. A transistor is, very simply, a switch that can be turned on or off by the application of a voltage. First developed in the early 20th century,[27] it is the basis of all modern electronic devices. The primary type of transistor of interest in this report is the field effect transistor (FET), specifically the organic

analogue (OFET). An OFET device (with bottom gate, bottom contact architecture) is shown in Figure 1.6, consisting of three electrodes- the source (S), gate, and drain (D).
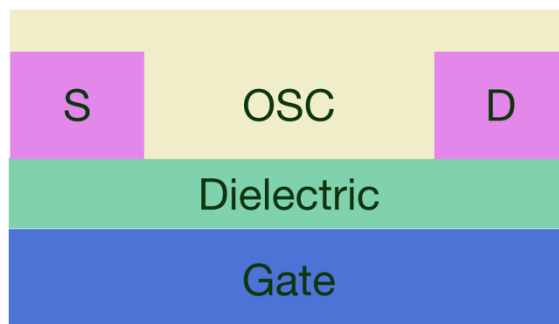
Figure 1.6: General device structure of an OFET.

Charges move through the OSC from the source to the drain when a potential is applied between the gate and the source.[28] The rate at which charges can be transported is known as charge carrier mobility (μ, reported in cm^2/Vs) and is dependent on intrinsic properties of the active material and the device architecture and fabrication method. Charge carrier mobility is typically regarded as the primary figure of merit in determining the performance of an OFET. There are numerous reviews on OFET operation and performance;[29] however, as the materials discussed in this work are still in the very early stages of evaluation for OFET applicability, further discussion of the many intricacies of OFETs is beyond the scope of this introduction.

The next application of interest is a photovoltaic (PV). PVs utilize semiconducting materials to convert light to electricity: a photon is absorbed, exciting the material to promote an electron from the valence band to the conduction band, generating an electron-hole pair. The movement of these charges is exploited to produce a current. The efficiency of this process is the termed the power conversion efficiency, or PCE; increasing this value is the primary goal of research in this field. Silicon-based PVs are the most common commercially available products of this type and give a maximum PCE of approximately 26%, meaning that much of the sunlight that reaches the device is not converted to electricity.[30]

Organic photovoltaics (OPVs) are also a popular innovation area, and years of optimization have yielded top materials reporting a PCE of over 17%.[31] While the performance of OPVs has increased dramatically due to these advancements, issues of stability and scalability with organic materials remain barriers to the widespread

commercialization of OPVs. The work covered in this dissertation, however, focuses on a hybrid model utilizing a silicon PV and an organic material working in tandem in order to improve performance, discussed further in Chapter 3. Thus, extensive background on OPV materials and operation will not be discussed, though many extensive reviews exist on this topic.[32] Instead, this introduction will be focused exclusively on silicon PVs.

The maximum performance in terms of PCE of a silicon solar cell, as determined by a report from Shockley and Queisser, is quite limited, unable to reach values above approximately 30%.[33] This is known as the Shockley-Queisser limit. When a semiconducting material such as silicon is excited by an absorbed photon, an electron is transferred from the valence band (the highest energy occupied electronic states) to the conduction band (the lowest unoccupied electronic states). The energy difference between the valence and conduction bands is known as the band gap, as introduced in Chapter 1.3; in silicon, the band gap is about 1.1 eV.[30] Thus, in order for a photon to successfully excite a material and move an electron from the valence to conduction band, the energy of the photon must be at least that of the band gap energy. Photons that are below 1.1 eV are therefore not capable of being utilized by a silicon solar cell, as shown in Figure 1.7 (a), where the grey dotted line represents the difference between the energy required and the actual energy of the theoretical photon.
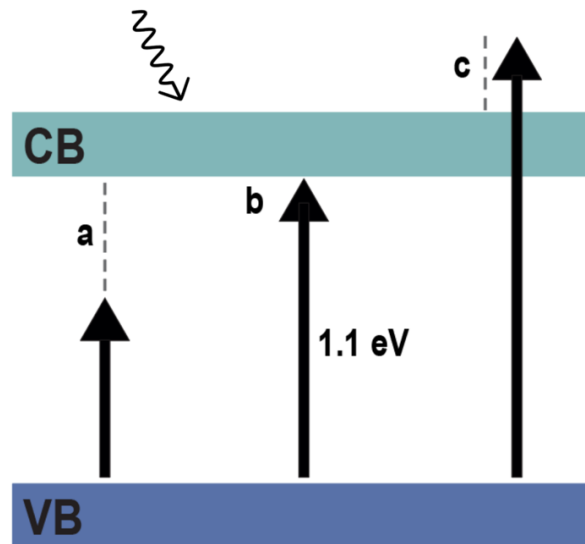
Figure 1.7: Valence and conduction bands in a silicon solar cell, depicting (a) photons that are below 1.1 eV and cannot be utilized by a silicon PV, (b) photons that are exactly 1.1 eV, and (c) photons that are above 1.1 eV, where the excess energy is lost as heat.

The Shockley-Queisser limit takes into account the band gap and the several other factors that limit the amount of sunlight that can be converted to electricity. In addition to a percentage of photons being too low energy, any extra energy from a high-energy photon beyond what is necessary to generate an electron-hole pair is lost as heat, represented in Figure 1.7 (c). This thermalization loss is the primary energy-loss pathway in silicon PVs. Since only photons of at least the appropriate energy can be utilized at all (this "perfect" scenario is represented in Figure 1.7 (b)), and those of higher energy will inevitably lose a portion of their energy as heat, the Shockley-Queisser limit cannot be overcome without incorporating other materials or device architectures that allow a wider energy range of photons to be absorbed and converted from solar to electrical energy. One potential strategy for circumventing the Shockley-Queisser limit takes advantage of singlet fission,[34] discussed in more detail in the following sections and in Chapter 3.

1.5: Photophysical Phenomena and Singlet Fission

Organic materials may undergo a range of photophysical transitions, as depicted below in the Jablonski diagram shown in Figure 1.8. The transitions from ground state to various excited states and back to ground correspond to various absorption and emission phenomena. As shown in Figure 1.8, absorption (a, blue) is represented by the transition from S_0 to vibrationally excited S_1. This corresponds to an excitation due to absorption of a photon. Vibrational relaxations (b, black) occur rapidly between vibrational levels as shown without a change in energy level. From the singlet excited state, there are several possibilities for relaxation. The first of these is emission of a photon, fluorescence (c, pink), which occurs rapidly on the nanosecond timescale. Next is internal conversion (d, grey), or non-radiative decay from an excited to a ground state without emission of a photon, with the excitation energy lost as heat. Intersystem crossing (e, black) from a singlet to triplet state (involving a spin flip) is also possible, though this process is typically slower, on the order of milliseconds. It is not common for organic molecules to reach a triplet excited state through intersystem crossing, though this triplet state may be reached through singlet fission, discussed in more detail below. Excitation directly to the triplet state is spin-forbidden and is generally not observed. Relaxation from the triplet state to ground is known as phosphorescence (f, green); this process is also typically slow.

Absorption (a) and emission (c) are of particular interest to this work, due to the relationship of absorbance to material characteristics such as the band gap (as discussed above, these are related but not equivalent); additionally, several of the compounds discussed in Chapter 2 are highly fluorescent.
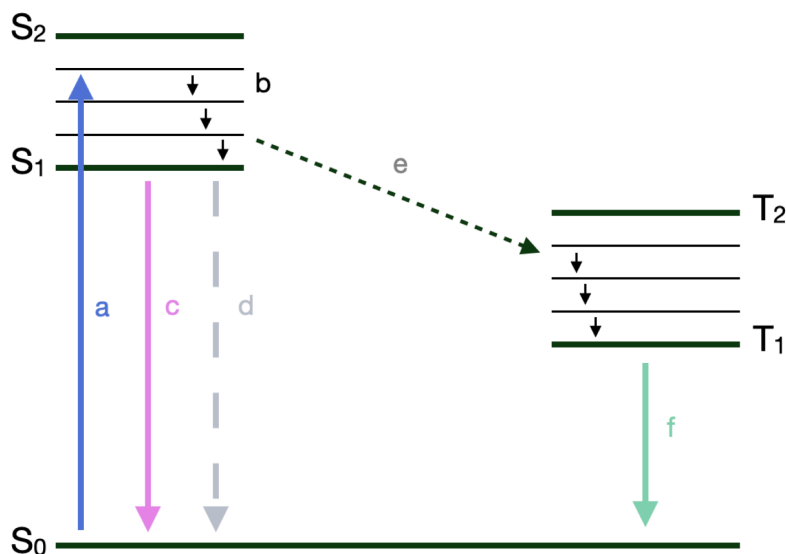
Figure 1.8: Jablonski diagram showing a) absorbance, b) vibrational relaxations, c) fluorescence, d) internal conversion, e) intersystem crossing, and f) phosphorescence.

A process unique to organic materials is singlet fission, which is a bimolecular process by which one singlet exciton is converted to two triplet excitons. It is spin-allowed and occurs rapidly on a pico- or femtosecond timescale; thus, it can be faster than other potential pathways and may give very efficient triplet production.

The equation below describes the process of singlet fission,[35] where S_0 is the ground state on one molecule, S_1 is the singlet excited state on an adjacent molecule, and T_1 is the first triplet excited state. This state is depicted as $2T_1$ in Figure 1.8 and is equivalent to the $T_1 + T_1$ term in the equation below; while one triplet exciton is typically approximately half the energy of the singlet exciton, two triplets are produced during singlet fission, thus the total energy of the two triplets is twice that of T_1. The TT state is an entangled triplet pair with an overall singlet spin. It is a so-called "dark state" that cannot be reached from the ground state but acts as an intermediate in the formation of two free triplet excitons.[36]

$$S_1 + S_0 \rightarrow TT \rightarrow T_1 + T_1$$

There are two types of singlet fission: exothermic, in which the singlet energy is more than double the triplet energy, and endothermic, in which the singlet energy is less than double the triplet energy. The former case allows singlet fission to occur on very rapid timescales, though the excess energy left over after fission is lost via a decay pathway (usually thermalization), while the latter may require thermal activation to overcome the energy barrier to fission. Figure 1.9 shows a diagram of this process and illuminates the energy difference between endothermic and exothermic singlet fission process.
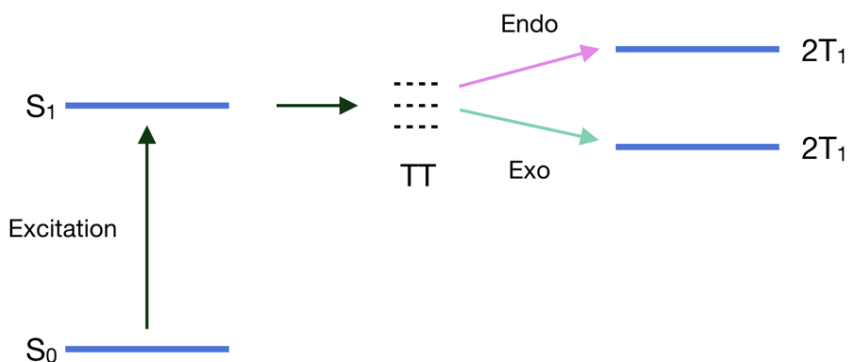
Figure 1.9: Singlet fission diagram, demonstrating the difference in energy in endothermic ("endo") and exothermic ("exo") SF processes.

An important aspect of singlet fission is the rate at which it occurs. In order for a material to undergo singlet fission, the fission process must outcompete other decay pathways, such as radiative and non-radiative recombination or excimer formation.[30] Ideally, singlet fission occurs on the picosecond timescale or faster and produces two triplet excitons for each absorbed photon.

For a material to be able to undergo singlet fission, the singlet energy of the material must be within 200-300 meV of twice the triplet energy.[37] The increase in entropy achieved from endothermic singlet fission has been found to be a sufficient driving force to overcome the energetic barrier even at ambient temperatures, though too large an energy difference is prohibitive to singlet fission.[38] The crystal packing of a material is also quite important; as singlet fission is a bimolecular process involving adjacent molecules, different packing motifs may be favorable or disfavorable towards singlet fission. For example, a slipped-stack packing motif has been found to be preferred in a range of

materials, due to the advantageous overlap of the relevant orbitals, whereas other crystal orientations decrease these interactions.[39]

Energy levels and crystal packing alone are not enough to guarantee that a material will be an efficient singlet fission material in device applications. Materials must also have high absorptivity, sufficient triplet lifetimes, and be stable within the device parameters for extended operative periods. Finding a material that undergoes singlet fission is only the first step in a lengthy process of derivatization and optimization.

1.6: Triplet Harvesting

The idea to utilize singlet fission as a way to improve the efficiency of PV devices was first proposed by Dexter in 1979,[40] with the intent to pair an organic singlet fission material with a traditional inorganic silicon solar cell. This would allow higher energy photons to be harvested by the singlet fission material and converted to triplets, which could then be absorbed by the lower band gap silicon.

There are two ways, in theory, to utilize singlet fission to improve the PCE of a solar cell: through charge transfer or through energy transfer. In the former case, the produced triplets are dissociated at the heterojunction formed between the singlet fission material and the inorganic, and separated charges are transported through the two materials and collected at electrodes.[41] Problems with this method arise from the difficulty of forming a high-quality heterojunction between the organic and inorganic materials, on which there are few extensive reports. Of interest in this dissertation is the latter method, where the singlet fission material is excited by an absorbed photon and fission occurs, and the triplets can be transferred to the low band-gap material. Studies have shown that triplets can be transferred from an organic singlet fission material to inorganic quantum dots via Dexter energy transfer, and that this transfer process can be quite efficient.[42] It was also suggested that this organic/quantum dot system could be paired with a traditional silicon solar cell to increase PCE, potentially doubling the photocurrent produced for each photon initially absorbed.[43] It is this theory that forms the basis for the work discussed in Chapter 3, where an acene chromophore is functionalized with ligand moieties.

Aromaticity and antiaromaticity are foundational concepts in defining π-conjugated systems and are often defined in simple terms: in addition to being cyclic and planar, aromatic compounds possess [4n + 2] π-electrons in the conjugated cycle and antiaromatic compounds possess [4n] π-electrons. However, this definition often proves incomplete and a universally agreed upon set of criteria is constantly debated and evolving.[44] The general characteristics for aromaticity and antiaromaticity have expanded to include energetic, spectroscopic, magnetic, and other properties,[45] rendering the definitive assignment of a compound as aromatic or antiaromatic more involved than simply counting electrons. Introduced in 1967 by Ronald Breslow,[46] antiaromaticity was defined as a system in which the cyclic delocalization of electrons is destabilizing.[47] If aromaticity is the stabilization found in cyclic conjugated compounds, where the linear analogue is treated as the standard, then antiaromaticity may be considered the destabilization of cyclic conjugated systems compared to the linear. This aromatic stabilization[48] often results in structures with delocalized π-electrons, whereas antiaromaticity tends to yield highly localized π-bonds.[49]

Further, aromatic and antiaromatic compounds exhibit distinct magnetic properties; due to the shielding or deshielding of nuclei associated with aromatic or antiaromatic compounds, respectively, ring currents are observed in these molecules that affect how they behave in the presence of a magnetic field. The understanding and quantification of these magnetic properties is a complex and well-studied field itself,[50] but the relevant takeaway can be summarized as follows: the presence of paratropic ring currents (which manifest as an upfield shift in the NMR spectrum relative to the non-aromatic analogue) is considered strong evidence of antiaromaticity[51] while the opposing diatropic ring current and relative downfield shift is a hallmark of aromaticity.[52] These magnetic properties can be computationally determined using nucleus-independent chemical shift (NICS) values, which are a measure of absolute magnetic shielding, typically at ring centers. NICS calculations have become a commonplace method for assigning the degree of aromaticity (denoted by negative values) or antiaromaticity (positive values).[53] Several variations on these calculations exist, such as measuring the ring currents at multiple points across and around the ring, and employing various computational approximations during

calculation,[54] the combination of which offers a robust and well-supported method for determining the degree of aromatic or antiaromatic character.[55]

It is also well known that antiaromatic compounds can be highly reactive, and easily undergo reactions that allow them to adopt a less destabilized form. Additionally, the formation of an antiaromatic compound is often uphill in terms of energy. For example, Breslow demonstrated in his early studies on antiaromaticity that cyclobutadiene rapidly dimerizes via a Diels-Alder to form a non-aromatic tricyclic compound, with relief of antiaromaticity as the driving force.[56] Further establishing the basic characteristics of antiaromatic molecules, Breslow et. al. also reported that the pK_a of the allylic protons in cyclopropene is higher than those of 1-propene, because deprotonation of the cyclic compound gives an antiaromatic [4n] π-electron system,[46] which is disfavored. To avoid the destabilizing effect that is induced by full conjugation and thus antiaromaticity, some molecules that meet the criteria for antiaromaticity experience bond localization,[57] where there is significant alternation in the bond lengths between σ and π bonds, thus preventing true conjugation and formal antiaromaticity. This illustrates a key point in the synthesis of antiaromatic compounds: the formation of an antiaromatic molecule is often less favorable than generating an aromatic or non-aromatic molecule and may require more forceful conditions. This will be examined in more detail in the Chapter 5 regarding the synthesis and properties of dehydroannulenes.

Antiaromatic compounds have attracted recent interest as semiconductor materials. The acene-type aromatic materials typically employed as organic semiconductors often suffer from instability despite their promising electronic properties; unsubstituted derivatives are prone photooxidation or dimerization in ambient conditions[58] and longer acenes are particularly prone to stability issues. It has been proposed that a reduction of aromaticity or an increase in antiaromaticity may increase molecular conductivity[59] and minimize photooxidative decomposition,[60] which points towards exploring antiaromatic compounds as targets for high-mobility semiconductor materials, though this prospect is largely theoretical, and the overall instability of antiaromatic materials must be considered, not just their reduced proclivity these specific decomposition pathways. An additional consequence of increased antiaromatic character is a reduction in the HOMO-LUMO gap[61] due to the destabilization of the HOMO and stabilization of the LUMO.[62] The

lowering of the LUMO may be such that it allows air-stable device operation in n-type semiconductors,[63] which is an attractive, highly-sought feature and is largely dependent on the energetics of the LUMO.

A common strategy thus far has been the fusion of antiaromatic subunits to aromatic rings to form acene analogues, such as Haley's work on the insertion of pentalene or indacene into an acene core leading to an overall reduction of aromaticity of the chromophore.[64] In-depth studies on indacene-fused acenes indicate that while the resulting compounds do possess some degree of antiaromatic character, their paratropicity is highly variable and dependent on structure, while the diatropicity of the aromatic rings remains largely unchanged.[65] Using proven crystal engineering strategies,[66] these indacene-fused acenes were tailored to adopt packing motifs known to give efficient charge transport,[16] leading to impressive device performance and good π-stacking.[60] However, this performance cannot be unambiguously attributed to the antiaromatic character of the chromophore, as they do not accurately represent a pure antiaromatic system, and reports on a fully antiaromatic small-molecule organic compound for semiconductor applications remain very limited.

The primary focus on a molecule's aromatic or antiaromatic character is typically directed towards the ground state, though several reports (notably from Ottosson[49, 67] and Anderson[68]) suggest that antiaromaticity may play an important role in excited state interactions, and may be exploitable for optimizing the electronic and geometric properties in the excited state.[49] This is especially exciting when considering that the performance of electronic and photonic devices rely heavily on excited state interactions, and the ability to tune those properties may have an advantageous impact on material performance. While again, this prospect has not yet been reduced to extensive practice, the theoretical implications are exciting for the field of small-molecule organic semiconductors and point favorably towards the further investigation of antiaromatic molecules in this space.

a. Previous works: dibenzooctadehydro[12]annulenes (12-BDHA)
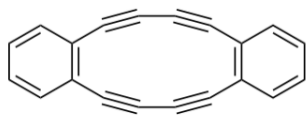
- Properties influenced by aromatic endcaps
- NICS = 22.32[a]

b. This work: octadehydro[12]annulenes (12-DHA)
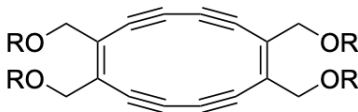
- Properties reflect antiaromatic core
- NICS = 57.36[b]

1a: R = MOM   **1d:** R = TIPS
1b: R = MOE   **1e:** R = TBDMS
1c: R = MOM   **1f:** R = TBDPS

Figure 1.10: (a) Previously reported DHAs with fused aromatic rings, (b) DHAs with only solubilizing substituents. [a]NICS value computed 1 Å above the core. [b]NICS value computed 1 Å above the core for derivative 1d.

Chapter 5 of this work describes the synthesis of octadehydro[12]annulenes (DHAs), shown in Figure 1.10 (b), a class of formally antiaromatic molecules expected to present fascinating electronic and photophysical properties. Despite their promise, the core molecule is seldom explored in the literature without aromatic endcaps (as in Figure 1.9 (a)), and papers resulting from this work are expected to be among the first to present systematic attempts at crystal engineering these molecules to maximize the potential for π-stacking and efficient charge transport.

1.8: Summary

Small-molecule organic semiconductors have widespread application across numerous disciplines, and the foundation of these prospects lie in crystal engineering and optimization of material properties. Through careful synthetic optimization to ensure the routes to these molecules are simple and scalable, one can quickly synthesize and screen a large number of derivatives and systematically evaluate their material properties.

This dissertation covers a range of small-molecule organic materials for multiple applications and is overall focused on developing structure-function relationships, elucidating the connections between core and substituent modifications and the resulting changes in electronic and photonic properties. This introduction serves to briefly cover the

basics of these applications, as well as give context for the materials themselves. Further details on each application, as relevant, can be found in the following chapters. Chapter 2 covers the energetic and photophysical properties of a range of heteroacene compounds, evaluating the effect of differing solubilizing groups and chromophore fluorination. Chapter 3 discusses the use of these heteroacenes as the singlet fission components in a hybrid OSC/QD photovoltaic system, along with the optimization of synthetic strategy to functionalize these molecules with ligand groups. Chapter 4 further explores the thienoanthracene chromophore functionalized with trialkylsilyl substituents for the generation of isolated triplet pairs and the exploration of triplet lifetimes, for eventual evaluation in quantum computing. Chapter 5 covers the synthesis and properties of dehydroannulenes, formally antiaromatic compounds with little literature precedence and a myriad of potential applications. While these topics are broad, all of the projects discussed in this dissertation relate to the synthesis and characterization of small-molecule OSCs and the tuning of their electronic and photophysical properties through derivatization and crystal engineering.

Chapter 2: Tuning the Crystal Packing and Material Properties of Heteroacenes

2.1: Heteroacene Introduction

      As discussed in Chapter 1.2, small organic molecules can be crystal engineered to adopt specific packing motifs and can be readily tuned for specialized applications. This has been extensively demonstrated in the acene series,[1] with functionalized tetracenes and pentacenes in particular employed in a myriad of niche applications across the realm of organic semiconductors.[2] Silylethynyl-substituted acenes are especially prevalent, given that the functionalization of acenes with these groups provides enhanced solubility and stability, while also serving as a method to control the solid-state order,[3] with substituents of different sizes inducing different crystal packing effects.

      One method for further fine-tuning the properties of small organic molecules is the incorporation of heteroatoms into the chromophore; in particular, five-membered heterocycles such as thiophene are commonly fused to linear acenes. It is well-reported that the substitution of thiophene for the terminal benzene rings in an acene tends to offer improved stability without significant impact on basic molecular geometry,[4] allowing an expanded range of chromophores to be investigated. However, the same solubilizing groups do not always induce identical packing on different chromophores; when moving from triisopropylsilylethynyl Pentacene (TiPS-Pn) to TiPS Anthradithiophene (TiPS ADT), both of which offer a similarly sized chromophore, the crystal packing changes from a 2D brickwork motif in TiPS-Pn to a 1D slipstack in TiPS ADT, while using the triethylsilylethynyl (TES) group on ADT returns the packing to 2D brickwork with even closer interplanar spacings than those found in TiPS Pn,[5] as shown in Figure 2.1. Thus, there is an inherent level of unpredictability in crystal engineering; while there are strategies such as that proposed by Anthony in 2002 (relating the silyl group diameter to chromophore length)[6] to induce a desired packing motif, there can be significant variation in the packing motifs caused by relatively minute changes to the solubilizing group or chromophore, or combinations thereof. This demonstrates the importance of simple and scalable syntheses that allow the rapid screening of numerous derivatives to better understand the structure-function relationships that are present (and often unique) for each type of chromophore.
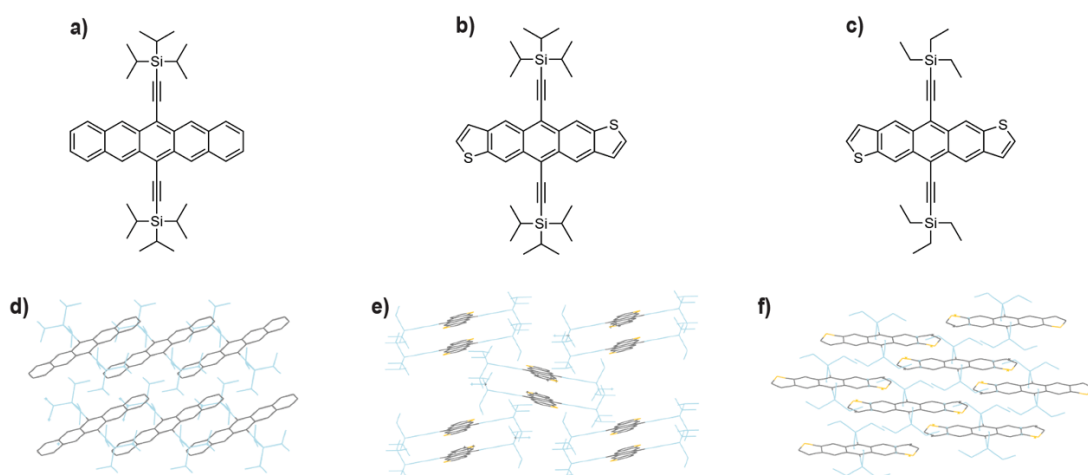
Figure 2.1: Structure (a) and packing (d) of TiPS Pentacene, structure (b) and packing (e) of TiPS ADT, and structure (c) and packing (f) of TES ADT.

Utilizing a library of known solubilizing groups allows rapid screening of derivatives and straightforward comparisons to other known compounds in order to further investigate the interplay between structural modification and resulting material properties. This chapter will explore heteroacenes, particularly thienoanthracenes, to gain insight into the crystal packing and photophysical properties of these chromophores when functionalized with a common set of silylethynyl solubilizing groups and substituted with various moieties to the core.

Thienoanthracenes (TAs) are part of the acene series, and take the general structure shown in Figure 2.2. In this work, they are functionalized with trialkylsilylethynyl substituents at the 5- and 10-positions; multiple other derivatives are also discussed, with the aim of understanding the factors that influence their crystal packing and optical and electronic properties.
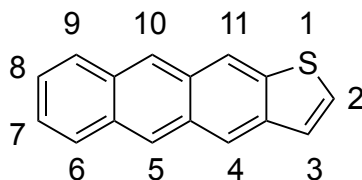
Figure 2.2: Structure and numbering of thienoanthracene.

This chromophore offers roughly similar optical properties as tetracene, a well-studied singlet fission chromophore,[7] with an improvement in stability, demonstrated and discussed further in Chapter 2.7. This makes TAs an advantageous starting point for further

investigation into optical applications, as they are stable, easily synthesized, and respond well to the same crystal engineering strategies employed in other acene chromophores, which have been developed and optimized extensively.[6] Chapters 3 and 4 discuss the singlet fission potential of these compounds and their substituted derivatives, while this chapter focuses solely on the relationship of crystal packing and material properties with solubilizing group and chromophore modification.

2.2: Synthetic Strategy

The synthesis of thienoanthracenes is known in the literature;[8] it employs straightforward and well-established reactions common for acenes and required little optimization for these specific derivatives. This scheme is shown in Figure 2.3.
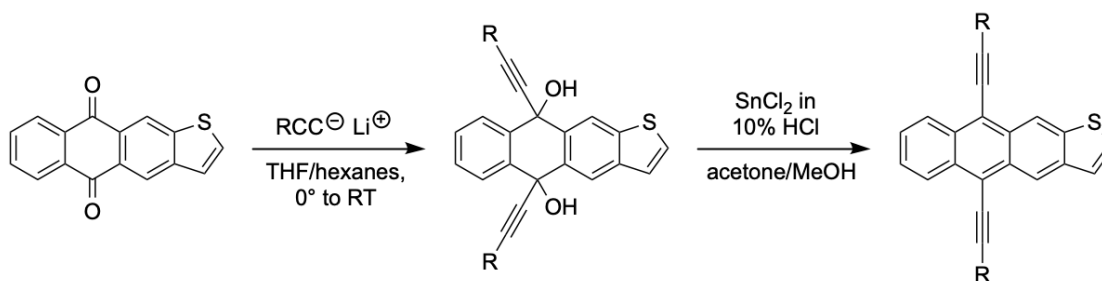
Figure 2.3: General Procedure A, basic synthetic scheme to thienoanthracenes. Further details can be found in the experimental section.

The diol intermediate between the quinone and aromatized product is isolated but is typically used immediately in the next step with little to no purification to minimize potential decomposition. Reductive deoxygenation to the aromatized compound proceeds rapidly according to literature conditions.[4]

The first derivatives to be synthesized were 1a-c, the TES, TiPS, and TiBS derivatives, respectively. These are among the most common silylethynyl groups utilized in our work and were chosen to provide a straightforward comparison to the analogous anthracene and tetracene compounds.
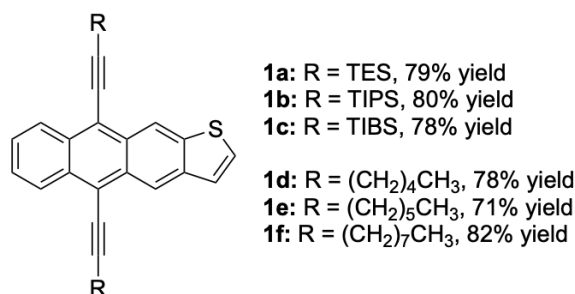
Figure 2.4: Thienoanthracene derivatives 1a-f.

Also of interest were derivatives not containing silicon, using instead straight-chain alkynes as the 5,10-substituents (1d-f). Alkylethynyl-substituted acenes have been previously reported and it is well-established that while linear alkyl groups may positively influence π-surface interaction in the crystal due to alignment of the alkyl chains, there is a maximum chain length at which the alkyl groups begin to lie between the π-surfaces and interrupt any π-surface interaction between adjacent molecules.[9] It was believed that evaluating this relationship in the thienoanthracene chromophore would contribute to our overall understanding of this molecule.

These derivatives 1a-f were obtained in good yield as shown in Figure 2.4, and typically crystallized rapidly from simple recrystallization techniques to yield large yellow or orange crystals. Despite yielding crystals that were visually large and uniform, 1a (TES TA) presented significant disorder when analyzed by X-ray diffraction (XRD), as seen in Figure 2.5. The typical thiophene ring flip disorder[10] that is often observed in thienoacenes is also present here, which makes it unclear whether the sulfur atom is "up" or "down" in the ring, and may also result in a thiophene ring on both "sides" of the anthracene; in reality, this is simply inherent disorder resulting in uncertainty about the location of the atoms in physical space. The ring flip disorder in hidden for clarity in 1b and 1c. Despite the significant disorder, the packing model of 1a proved sufficient to determine that there was not significant interaction between the π-surfaces of the molecules; instead, the silylethynyl groups block any relevant interactions. The TiPS derivative 1b shows minimal π-surface overlap between individual molecule pairs, with these pairs otherwise significantly isolated from other molecules by the silylethynyl groups. The presence or absence of carbon-carbon close contacts was evaluated using Mercury,[11] setting the program to search for contacts between carbon atoms only within a distance of the sum of the van der Waals radii plus 0.2

Å. Using this method, it was determined that C-C close contacts between atoms in the π-surfaces are not present in 1a, though 1b contains contacts between the isolated molecule pairs and 1c contains some carbon-sulfur contacts at the ends of the molecules.
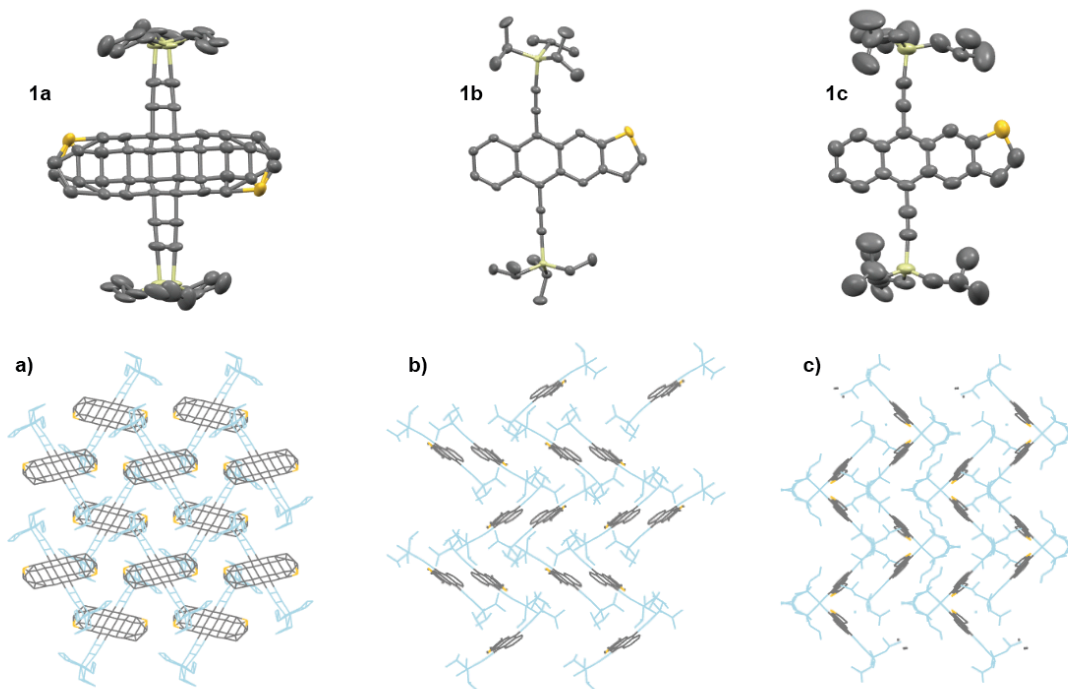
Figure 2.5: Ellipsoid structure and packing of 1a (a), 1b (b), and 1c (c).

Non-silyl derivatives 1d-f all show similar packing (Figure 2.6), where there is some interaction between the π -faces of adjacent molecules; however, as mentioned above, it appears that the alkylethynyl groups do lie between the π-surfaces of the chromophores and prevent good π-π interaction. While it appears that 1e and 1f may have an amount of overlap at the thiophene ends, the molecules that appear to touch are offset in the z-direction (into the plane) in a way that is not easily represented in a single still image. Carbon-carbon close contacts between the relevant atoms of the π-surfaces were not observed for any of 1d-f.
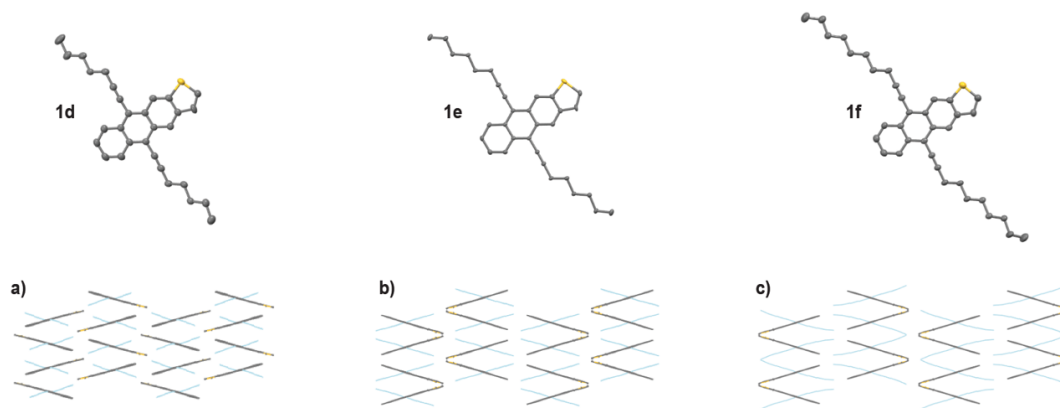
Figure 2.6: Ellipsoid structure and packing of 1d (a), 1e (b), and 1f (c), as viewed down the crystallographic c axis.

2.3: Fluorination of the Chromophore

Fluorination of an acene chromophore is a well-known method to attempt to improve crystallinity and stability and strengthen π-stacking,[12] as well as alter electronic properties.[13] In thienoacenes, this fluorination is typically at the 2-position of the thiophene ring, where F-H and F-S interactions between adjacent molecules can influence and contribute to enhanced crystalline order.[14]

2a: R = TES, 70% yield
2b: R = TIPS, 80% yield
2c: R = TIBS, 75% yield

3a: R = TES, 68% yield
3b: R = TIPS, 72% yield
3c: R = TIBS, 70% yield
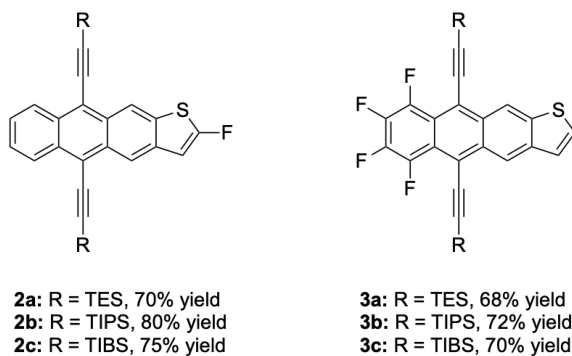
Figure 2.7: Fluorinated thienoanthracene derivatives 2a-c and 3a-c.

Synthesis of the 2-fluoroquinone uses the same literature conditions as the unsubstituted TA quinone, using commercially available 5-fluorothiophene-2,3-dialdehyde (FTDA) instead of unsubstituted thiophene dialdehyde (TDA). Derivatives 2a-c were obtained in good yields from General Procedure A.
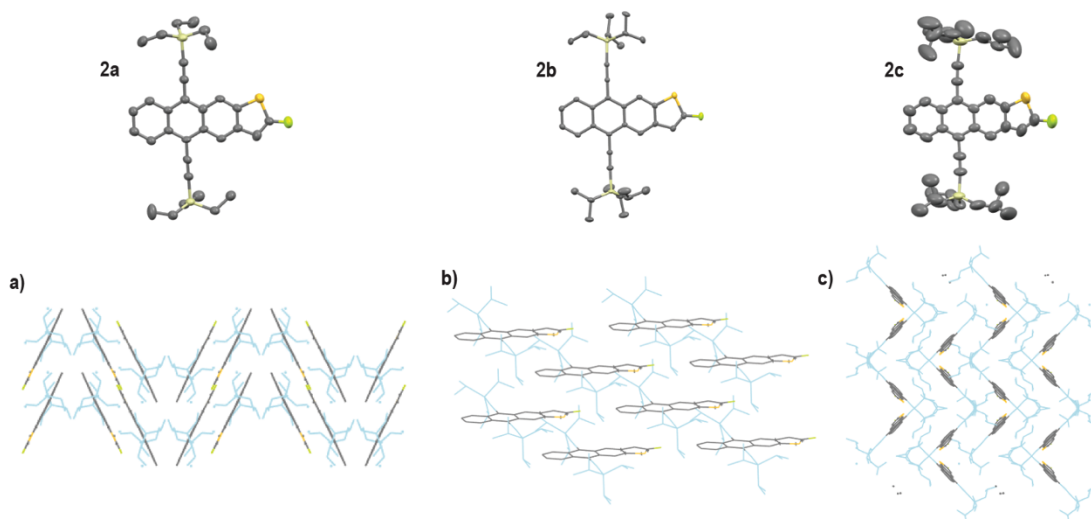
Figure 2.8: Ellipsoid structures and packing of 2a (a), 2b (b), and 2c (c).

The crystal packing motifs of 2a-c were evaluated for π-surface overlap and carbon-carbon close contacts. As shown in Figure 2.8, the packing motifs of 2a-c are varied, with 2a (TES) packing in some version of a 1D slipstack and 2b (TiPS) giving what appears to be a 2D brickwork motif. The interplanar distance (IPD) between the π-surfaces in 2a was measured to be 3.321 Å, which is well within the distance required for carbon-carbon close contacts, and these contacts are observed using the Mercury method described above. The IPD of 2b was calculated to be 3.382 Å and again, close contacts between the π-surfaces are observed. In 2a, there is some alternation in the direction of the fluorine atom, with H-F and S-F interactions between adjacent molecules. In 2b, however, all of the fluorine atoms are aligned to "point" in the same direction in each sheet of the brickwork motif, with each sheet having fluorines that point the opposite direction of the previous sheet. The TiBS groups in 2c were noted to be particularly disordered, as can be seen from the ellipsoid structure in Figure 2.8. This was common to many of the TiBS derivatives discussed in this chapter. Unfortunately, this structure shows no π-surface interaction, as the bulky silylethynyl groups block any communication between adjacent chromophores, and there are no formal close contacts, though the ends of the largely isolated molecules are separated by approximately 3.8 Å.

Fluorination of the carbocyclic end of the TA was also investigated. To the best of our knowledge, neither the tetrafluoro (4F) TA derivatives 3a-c nor the analogous tetracenes have been published, though tetrafluoropentacene (with and without silylethynyl

groups) is known in the literature,[12, 15] and is reported as an ambipolar semiconductor, capable of both p-type and n-type charge transport. The synthetic scheme for 4F TAs is shown in Figure 2.9. Each step was readily adapted from literature precedent, with the desired quinone obtained from commercially available starting material in five steps.
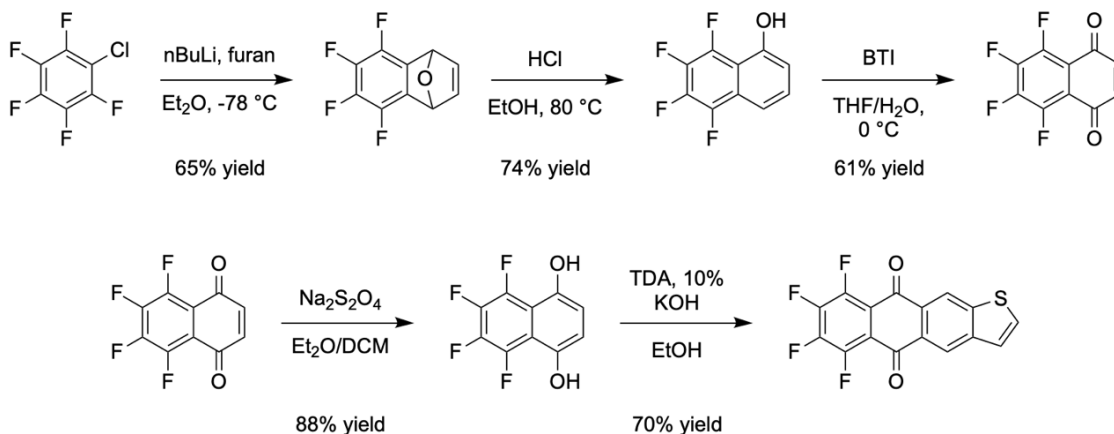
Figure 2.9: Synthetic scheme to 4F TAs. BTI = (bis(trifluoroacetoxy)iodo)benzene, TDA = thiophene dialdehyde. Reaction conditions adapted from literature precedent.[16]

The synthetic route starts from commercially available chloropentafluorobenzene with a butyllithium-mediated metal-halogen exchange to produce benzyne, which undergoes a Diels Alder with furan to yield the ether-bridged compound shown. Cleavage of the ether with hydrochloric acid gives the tetrafluoro-naphthol, which is oxidized to the naphthoquinone with BTI. The naphthoquinone is then reduced to the dihydronaphthoquinone, which reacts readily in an aldol with thiophene dialdehyde to give the tetrafluoroquinone. From the tetrafluoroquinone, the synthesis proceeds according to the conditions of General Procedure A as shown in Figure 2.3. Like the earlier discussed derivatives, 3a-c were readily obtained in good yield. These compounds crystallized as dark orange or red flakes, which were not well-suited to single crystal XRD, and 3c proved especially challenging to obtain suitable crystals. Thus far, crystallization of 3c from several different solvents and crystallization methods has not provided appropriate crystals for XRD analysis.
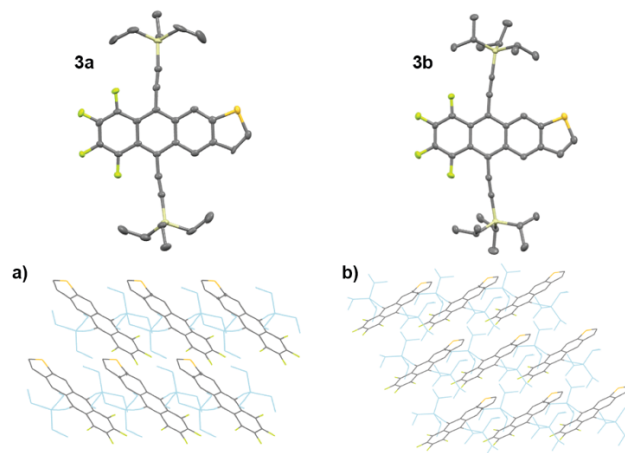
Figure 2.10: Ellipsoid structures and packing of 3a (a) and 3b (b).

Both 3a and 3b show 2D brickwork packing with C-C close contacts. The IPD of 3a was found to 3.201 Å and the IPD of 3b was found to be 3.335 Å, which are among the closest interplanar distances found for the compounds in this chapter. The alkynes are bent away from the fluorinated carbocyclic end, and there is clear alignment of fluorinated ends in the same direction throughout the packing motif.

2.4: Further Modification of Chromophore

Expanding the modifications to the chromophores that were investigated, the dioxolane-fused TAs 4a-c and 5a-c were also prepared, as shown in Figure 2.11.

4a: R = TES, 81% yield
4b: R = TIPS, 83% yield
4c: R = TIBS, 80% yield

5a: R = TES, 75% yield
5b: R = TIPS, 71% yield
5c: R = TIBS, 73% yield
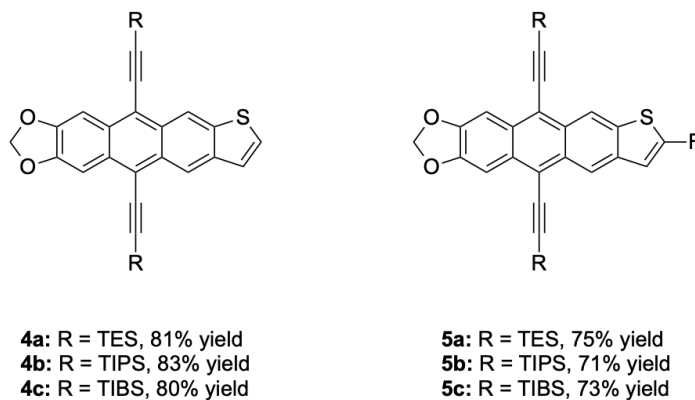
Figure 2.11: Thienoanthracene dioxolane derivatives 4a-c and 5a-c.

While dioxolane-fused TAs have not been published, the analogous anthracene is known in the literature,[17] though only the bare acene, not a silylethynyl substituted derivative, to the best of our knowledge. Synthesis of the dioxolane-fused TA quinone

proceeded from literature adapted steps as shown in Figure 2.12. Benzodioxole is brominated to give the ortho-dibromide. The next step is benzyne formation and a Diels Alder with furan, as in the synthesis of the tetrafluoroquinone, to form the analogous bridged ether. The following steps utilize the same approach as used for the tetrafluoroquinone. From the dioxolane quinone, the synthetic route follows General Procedure A to obtain the silylethynyl derivatives 4a-c. As with the other 2-fluorinated TA derivatives, compounds 5a-c are synthesized via the same conditions, again employing FTDA instead of TDA at the quinone formation stage.
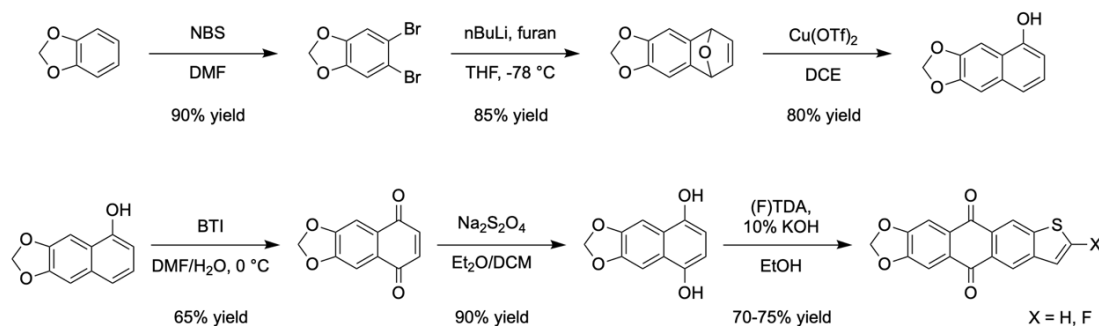
Figure 2.12: Synthetic scheme to dioxolane TAs. BTI = (bis(trifluoroacetoxy)iodo)benzene, TDA = thiophene dialdehyde, FTDA = fluorothiophene dialdehyde. Reaction conditions adopted from literature precedent.[18]

All derivatives crystallized readily and were submitted for XRD analysis. It was noted that while all derivatives yielded a solvable structure, there is significant disorder present. The thiophene ring flip disorder[10] that has been visible in other derivatives is also present here with the added effect of obstructing the dioxolane ring. This disorder has been hidden in the following figures for clarity.
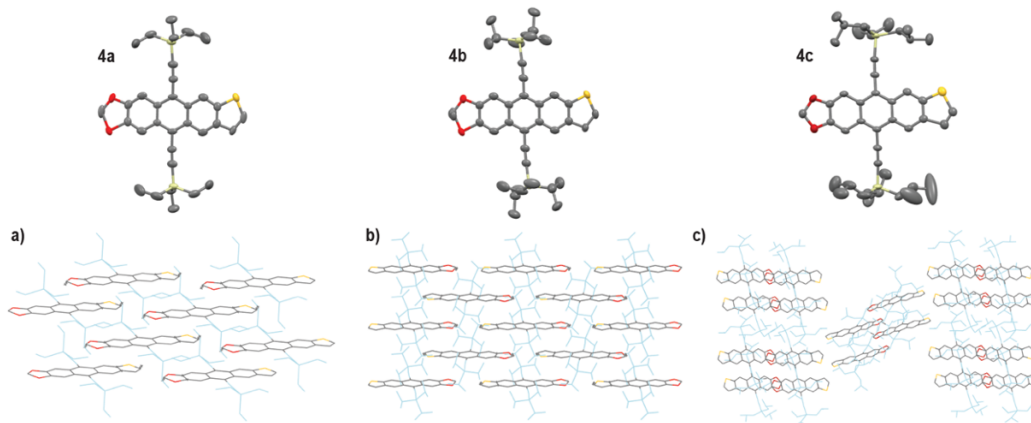
Figure 2.13: Ellipsoid structures and packing of 4a (a), 4b (b), and 4c (c).

As shown in Figure 2.13, both 4a and 4b appear to pack in a 2D brickwork motif. The interplanar distances were found to be 3.414 Å for 4a (which does contain close contacts) and approximately 3.728 Å for 4b. The π-surfaces in 4b are not completely planar, with a 3.49° angle between the planes of adjacent molecules, and thus the IPD is estimated; carbon-carbon close contacts are not observed for this derivative. The TiBS derivative 4c, however, resembles a 1D stack, with minimal overlap between the π-surfaces, an angle of 2.40° between the planes of molecules in each stack, and an estimated IPD of approximately 3.4 Å. Close contacts between π-surfaces of the thiophene end of one molecule and the dioxolane end of the next molecule are observed.

The fluorinated dioxolane derivatives 5a-c similarly show good π-surface overlap, with all of 5a-c packing in a 2D brickwork motif. There is incredible disorder present in 5a and 5b, as shown, so any conclusions drawn from these packing models should be carefully considered.
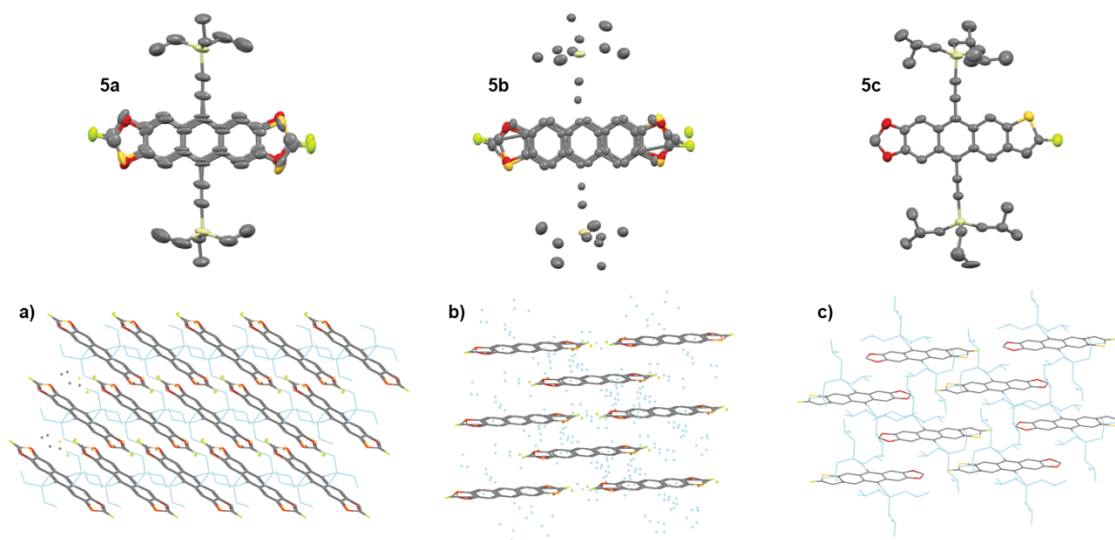
Figure 2.14: Ellipsoid structures and packing of 5a (a), 5b (b), and 5c (c).

The interplanar distances were determined to be approximately 3.35 Å for 5a, with numerous close contacts, approximately 3.4 Å for 5b, which also contained significant close contacts between the π-surfaces, and 3.389 Å for 5c, with some close contacts observed using the method above.

The effect of exploring other heteroatoms in fused acenes has been investigated previously, with several reports describing furanoacenes and selenoacenes with the corresponding thienoacenes, investigating the change in material properties moving down the chalcogen series.[19] Furanoanthracenes (FAs) were synthesized from furan-2,3-dialdehyde[20] and using the same procedure employed for TA quinone, followed by General Procedure A to obtain derivatives 6a-c.

6a: R = TES, 81% yield
6b: R = TIPS, 79% yield
6c: R = TIBS, 75% yield
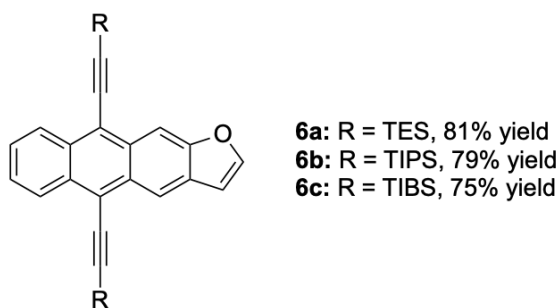
Figure 2.15: Furanoanthracene derivatives 6a-c.

No optimization of conditions was required when moving from thiophene to furan, with good yields obtained for all derivatives using the conditions of General Procedure A. All derivatives yielded large crystals that were suitable for XRD, though 6b is significantly disordered, as shown in Figure 2.16.
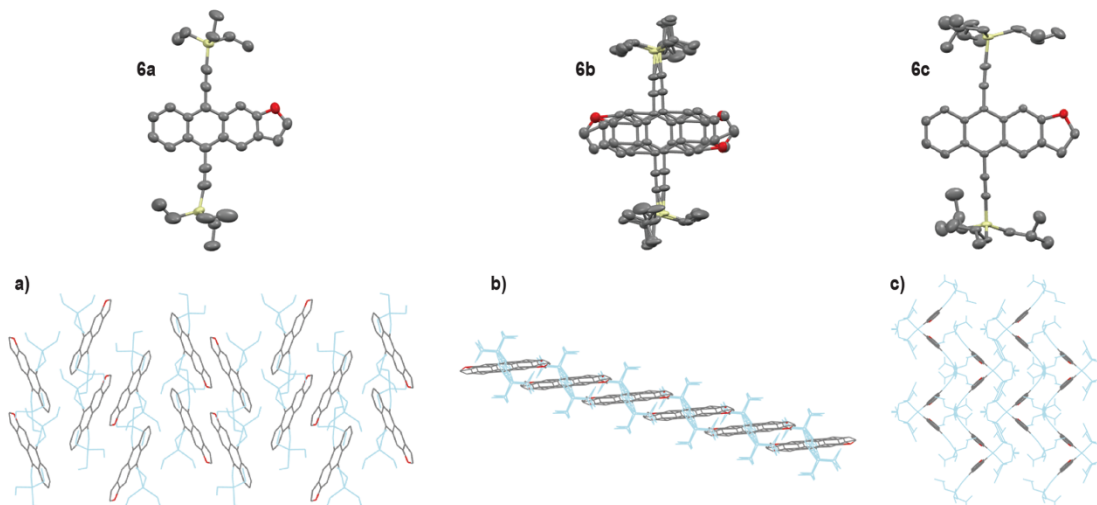
Figure 2.16: Ellipsoid structures and packing of 6a (a), 6b (b), and 6c (c).

Figure 2.16 shows the packing motifs of the furanoanthracene derivatives. Both 6a and 6b show good π-surface overlap, with 6a packing in a version of a 1D stack and 6b packing in what resembles a classic 1D slipstack. The interplanar distances are approximately 3.4 Å for 6a and approximately 3.3 Å for 6b, while 6c does not have any π-surface overlap, with the silylethynyl groups blocking the chromophores from each other. Close contacts are observed for 6a and 6b with the method described above.

2.6: Electronic Coupling in Select Derivatives

The crystal packing of the derivatives discussed above was highly varied, with some examples of classic packing motifs and others that are less easily categorized and described. We observe good π-surface overlap and C-C close contacts in numerous derivatives, despite varied packing motifs and disorder in several of the crystal structures.

The electronic coupling was calculated using DFT for derivatives that appear to exhibit a 2D brickwork motif. Of all the compounds synthesized, seven of the twenty-one compounds resembled 2D brickwork packing. These calculations were performed using the hybrid density functional B3LYP with a 6-31G(d) basis set,[21] courtesy of Dr. Karl Thorley of UK. Unfortunately, the high degree of inherent disorder present in several of the crystals rendered the determination of electronic coupling prohibitive for several derivatives. Efforts are ongoing to identify a way to resolve this disorder to yield an accurate model that represents the true crystal structure of these materials. Thus far, the electronic coupling for only two derivatives, 2b and 5c, has been possible to calculate, and other calculations are ongoing pending the resolution of the significant disorder for the purposes of DFT calculations. The results of the calculations completed to date are shown in Table 2.1.

Table 2.1: Calculated electronic coupling values for heteroacenes.

Compound	HH	HL	LL
2b (F TIPS TA)	2.5 meV	67 meV	44 meV
5c (F TIBS TA diox)	32 meV	44 meV	26 meV

The values shown above are representative of the electronic coupling between molecular pairs. The data here includes the relationship between the HOMO of both molecules (HOMO-HOMO, or HH), the HOMO of one molecule and LUMO of the other (HOMO-LUMO or HL), and the LUMO of both molecules (LUMO-LUMO or LL). The LUMO-HOMO is also calculated but is identical to the HOMO-LUMO for these compounds, and thus is not shown here. The HOMO-HOMO coupling is relevant to p-type semiconductors, the LUMO-LUMO to n-type, and the HOMO-LUMO to optical applications such as singlet fission, which will be discussed further in Chapter 3. In both compounds, it is the HL coupling that is strongest, and these values of 67 meV for 2b (F TiPS TA) and 44 meV for 5c (F TiBS TA dioxolane) are generally on the order of magnitude that is considered strong electronic coupling in organic materials. For example, in TiPS Pentacene, the HH coupling has been cited on the order of 30 meV, and the LL coupling as 80 meV.[22]

2.7: Photophysical Characterization

The energetic and photophysical properties of the heteroacene derivatives were evaluated to continue building our understanding of the effect of functionalization on these chromophores. Solution absorbance of the representative TiPS derivatives was measured and compared to TiPS Tetracene, as shown below in Figure 2.17. TiPS Tetracene has been the benchmark compound for numerous photophysical studies[23] (which will be explored further in Chapter 3), but as discussed previously, its photostability is poor.
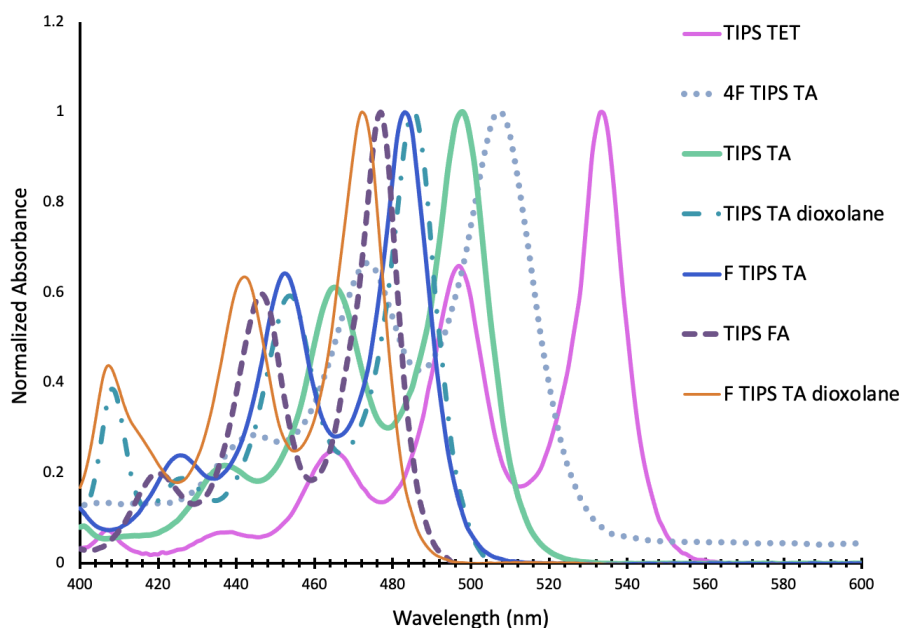
Figure 2.17: Absorbance of representative derivatives 1b, 2b, 3b, 4b, 5b, and 6b. Spectra taken in DCE at RT at approximately 10 μM.

As shown in Figure 2.17, all the heteroacene chromophores are blue-shifted relative to tetracene. The maximum absorbance values are summarized in Table 2.2 below, demonstrating the trends along the series with varying functionalizations. Fluorination at the 2-position induces a consistent blue-shift in the absorbance, while tetrafluorination at the benzene end induces a red-shift relative to the unsubstituted TA. The dioxolane ring also offers a blue-shift, though a smaller one than that resulting from 2-fluorination. Substitution of the sulfur for oxygen in the furanoanthracenes causes a significant blue-shift as well. The combination of 2-fluorination and dioxolane substitution offers the largest blue-shift, pushing the maximum absorbance almost to that of anthracene.[24]

All the derivatives are highly fluorescent in solution, and some of them are also fluorescent in the solid state to varying degrees. The solution fluorescence of each representative TiPS derivative is shown below in Figure 2.18 (a), and the solid-state fluorescence of 6c is shown in Figure 2.18 (b). It has been previously reported that strong π-π interactions in organic molecules can lead to fluorescence quenching,[25] as the aggregation in the solid state allows excited molecules to more easily relax or decay non-radiatively, preventing emission, while in dilute solution the molecules may remain isolated and emit strongly.[26] While some of the compounds listed above that exhibit solid-

state fluorescence do show π-surface interactions in the crystal structure, it is 6c (TiBS FA) that is most strongly solid-state fluorescent, as shown below in Figure 2.18 (b); this derivative contains no π-surface interactions, as can be seen above in Figure 2.16 (c) in section 2.5.
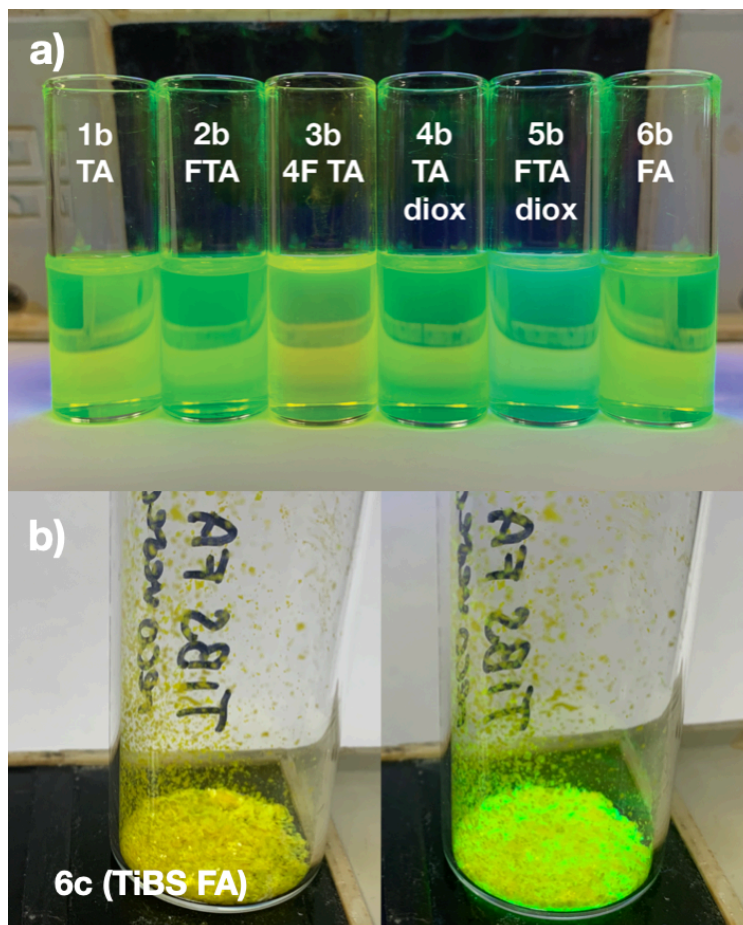
Figure 2.18: Solution fluorescence of representative derivatives (a) and solid-state fluorescence of 6c (b).

Solid-state fluorescence also reveals more about the photophysical properties. Recall the Jablonski diagram; fluorescence is one of the several ways that a molecule may relax from the excited to ground state. Based on the timescales of photophysical events, singlet fission (which is examined in the heteroacene molecules in Chapters 3 and 4) should occur faster than fluorescence. The observation of fluorescence in the solid state, where singlet fission typically occurs, implies that the excited state is not decaying via singlet fission, but rather remains long enough for the molecule to fluoresce.

While not at all intended to be a quantitative assessment of whether a molecule will undergo singlet fission in the solid state, the observation of solid-state fluorescence is a

strong indicator that the molecule will not be a good singlet fission candidate. The following derivatives were evaluated for the presence of solid-state fluorescence. When comparing these derivatives to their crystal packing motifs, shown in section 2.5, these derivatives represent a range of different packing motifs.
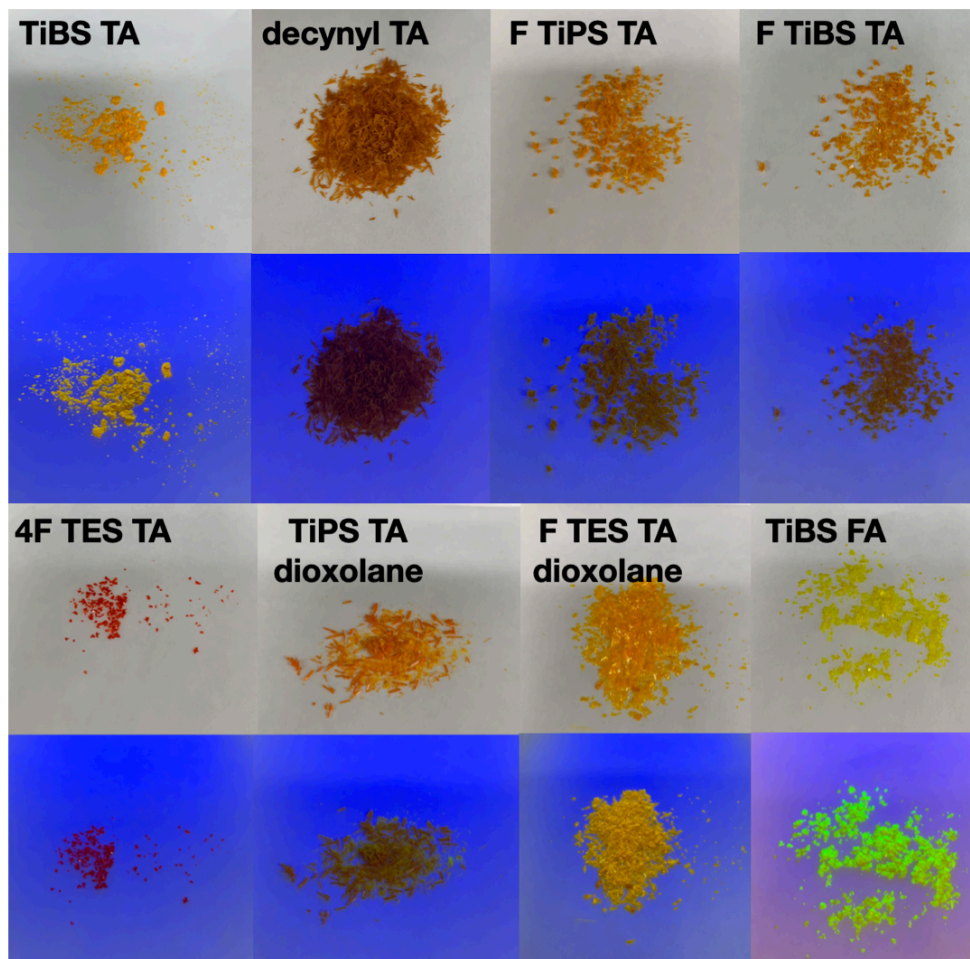
Figure 2.19: Solid-state fluorescence or lack thereof in representative heteroacenes.

As shown in Figure 2.19, TiBS TA (1c) and TiBS FA (6c) exhibit clear solid-state fluorescence, and F TES TA dioxolane (5a) exhibits a very slight fluorescence in the solid-state. In particular, 1c and 6c show very similar packing motifs, with the chromophores largely isolated from each other by the silylethynyl groups. It follows that these two derivatives may not be well-suited to singlet fission applications.

The solution emission spectra of the representative TiPS derivatives were measured and compared to the respective absorption spectra, shown below in Figure 2.20. Similar absorbance and fluorescence features are present in all derivatives.
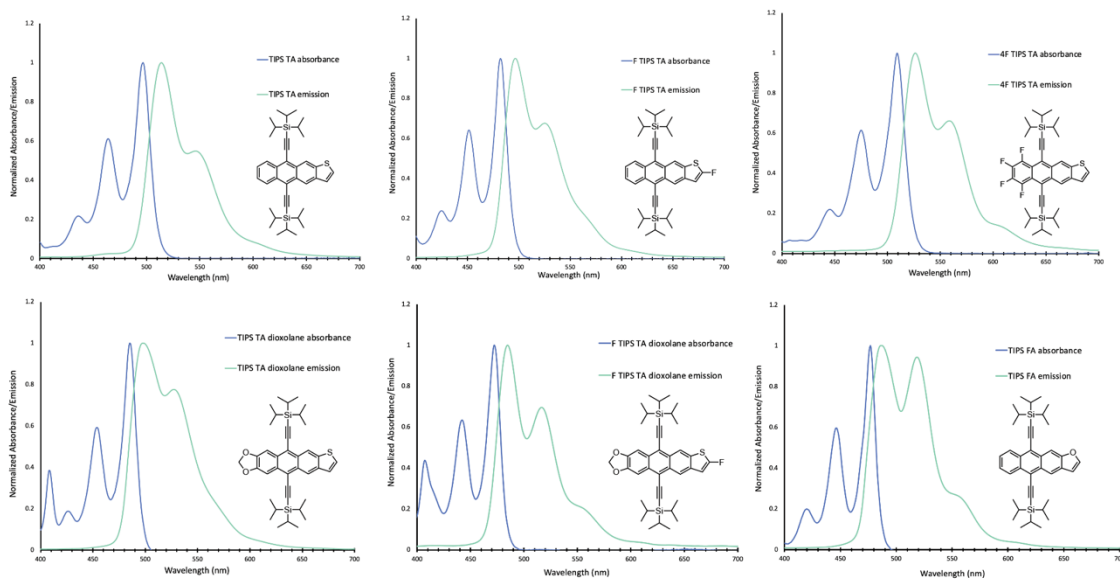
Figure 2.20: Absorbance vs. emission spectra for each of the TiPS derivatives as measured in DCE at approximately 10 μM concentration for absorbance and approximately 1 μM for emission.

As shown in Figure 2.20, fluorescence occurs at a longer wavelength (lower energy) in all derivatives, as expected. The difference between the maximum absorbance peak and maximum emission peak is known as the Stokes shift, and is primarily the result of vibrational relaxation or solvent reorganization. While tuning this feature was not part of the intention of this project, slight variations can be noted between derivatives.

Table 2.2: Maximum absorbance and emission wavelengths and calculated S_0 to S_1 transition energies.

Compound	$\lambda_{max,abs}$ (nm)	$\lambda_{max,em}$ (nm)	S_0 to S_1 (eV)
1b TIPS TA	498	514	2.41
2b F TIPS TA	482	496	2.48
3b 4F TIPS TA	509	526	2.33
4b TIPS TA diox	485	497	2.48
5b F TIPS TA diox	471	485	2.55
6b TIPS FA	477	487	2.53

The photophysical properties of the heteroacene derivatives are summarized in Table 2.2. The absorbance and emission maxima were obtained directly from the respective

spectra, and the S_0 to S_1 transition energy was estimated from the wavelength corresponding to the onset of the primary absorption peak.
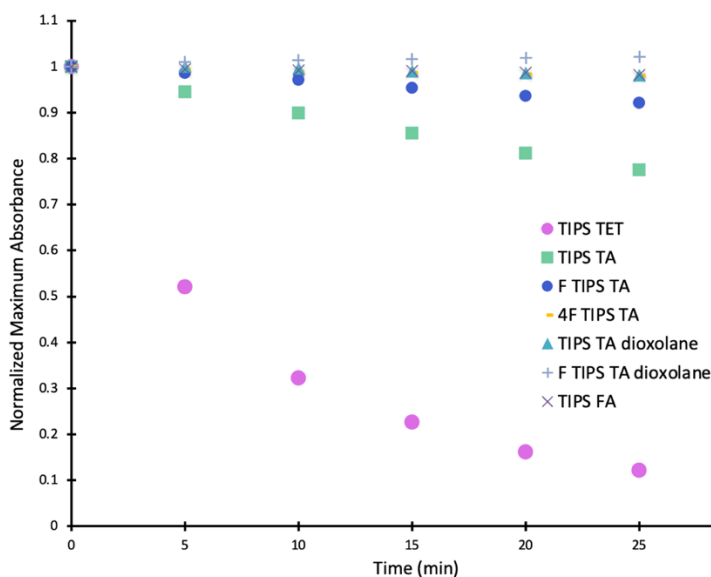
Figure 2.21: Stability of representative heteroacenes derivatives compared to TIPS Tetracene.

Stability of the heteroacenes was evaluated by UV-vis spectroscopy. Solutions at approximately 10 μM in DCE were prepared, using the TiPS derivative of each chromophore. The initial UV-vis spectra were measured, and then the samples were irradiated using a broad spectrum light source for 30 minutes, taking additional spectra every 5 minutes. The decay in the maximum absorbance peak (which is the S_0 to S_1 transition in acenes) was evaluated, and these results are summarized in Figure 2.21. This comparison is meant to examine the relative behaviors of these molecules rather than make a quantitative assessment of their rates of decay. While stability in application will be influenced by numerous factors not reflected in this simple experiment, the data in Figure 2.20 indicates that certain chromophores are more likely to be suitable for applications involving extended exposure to natural light, as will be examined further in Chapter 3.

As shown, TiPS Tetracene decomposes rapidly with exposure to light. This has been well-established in our group for some time. However, this makes tetracene chromophores unideal for any kind of photophysical applications, which will be discussed further in Chapter 3. TiPS TA, 1b, shows an improvement in stability compared to TiPS Tet, but does show some decomposition in solution. F TiPS TA, similarly, offers improved but still imperfect stability. The remaining derivatives (4F TiPS TA, TiPS TA dioxolane,

F TiPS TA dioxolane, and TiPS FA) show very little if any degradation in their absorbance spectra. All heteroacene derivatives are noted to be bench-stable in the solid state when stored in sealed containers over a period of at least several months, though this is not quantitatively shown.

2.8: Conclusions

As described in the prior sections, the heteroacenes synthesized in this work present fascinating properties and easily tunable electronic characteristics, which fall between those of tetracene and anthracene. These compounds are easily synthesized and purified, allowing for the relatively rapid screening of solubilizing substituent groups and other functionalizations that contribute to the relevant electronic, energetic, and photophysical properties.

The crystal packing of the described derivatives was evaluated, with several derivatives exhibiting good π-surface overlap, carbon-carbon close contacts, and moderate electronic coupling. The optical properties reveal a high level of tunability with relatively simple functionalizations, and all derivatives exhibit good stability both in solution and the solid state. These chromophores present an interesting class of compounds along the acene series and may offer utility in numerous applications, described further in the following chapters. Presented here is a robust foundation of how modifications to heteroacenes affect the resulting properties, which provides the basis for future evaluation of other derivatives.

2.9: Experimental

Solvents were purchased in bulk from VWR, and other reagents were purchased from commercial sources (typically Sigma Aldrich) and were used as received. NMR spectra were measured on a 400 MHz Bruker instrument, and chemical shifts are reported in ppm and referenced to the deuterated solvents used. Absorbance was measured with an Agilent Cary 60 UV-vis spectrometer and fluorescence measured with StellarNet Inc. fluorimeter. Crystal structures were collected and refined by Dr. Sean Parkin of UK using a dual-microsource Bruker D8 Venture κ-axis diffractometer (MoKα & CuKα) with large-area 'Photon-II' CMOS detector.

General Procedure A: In a 0.1M solution of hexanes/THF (9:1-3:1 ratio) in a flame-dried flask under nitrogen, 3.5 equivalents of silyl acetylene were dissolved. The reaction solution was cooled to 0 °C and 3 equivalents of LiHMDS were added dropwise. The solution was allowed to stir for 30 minutes to 1 hour, after which the quinone starting material was added in one portion. The reaction solution was stirred overnight, and upon completion as determined by TLC, was quenched with deionized water and extracted with hexanes. The organic layers were dried with magnesium sulfate and concentrated by rotary evaporation. This diol intermediate was typically observed as a yellow or colorless oil and was used immediately without further purification. The diol was dissolved in minimal acetone and diluted with 0.1 M methanol open to air. To this, 6 equivalents of $SnCl_2$ dissolved in minimal 10% H_2SO_4 was added in one portion. The reaction solution was allowed to stir for 1 hour and then was extracted with hexanes. The organic layers were dried with magnesium sulfate and concentrated via rotary evaporation. The resulting yellow, orange, or red solids were purified via chromatography with hexanes and recrystallized with acetone to give yellow or orange crystals.

1a TES TA: Prepared via **General Procedure A**. 79% yield. ^{1}H NMR (400 MHz, CDCl$_3$): δ 9.16 (t, J_{HH} = 0.89 Hz, 1H), 9.11 (d, J_{HH} = 0.49 Hz, 1H), 8.62 (dd, J_{HH} = 6.58 Hz, 3.39 Hz, 2H), 7.59-7.57 (m, 3H), 7.48-7.47 (m, 1H), 1.22 (td, J_{HH} = 7.88 Hz, 2.17 Hz, 18H), 0.89 (q, J_{HH} = 7.9 Hz, 12H). ^{13}C NMR (101 MHz, CDCl$_3$): δ 140.11, 139.75, 132.29, 132.08, 129.94, 129.84, 127.35, 127.30, 126.69, 126.57, 123.79, 121.36, 120.14, 118.74, 117.54,

106.51, 106.25, 103.09, 103.01, 7.85, 4.75. Structure confirmed by single crystal X-ray diffraction.
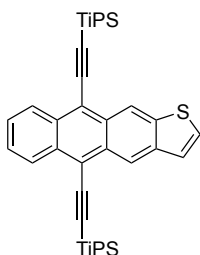
1b TIPS TA: Prepared via **General Procedure A**. 80% yield. ^{1}H NMR (400 MHz, CDCl$_3$): δ 9.20 (s, 1H), 9.15 (s, 1H), 8.64 (dd, J$_{HH}$ = 6.84 Hz, 3.21 Hz, 2H), 7.59-7.55 (m, 3H), 7.44 (d, J$_{HH}$ = 5.66 Hz, 1H), 1.33-1.29 (m, 42H). ^{13}C NMR (101 MHz, CDCl$_3$): δ 140.18, 139.85,132.48, 129.88, 127.47, 127.42, 126.76, 126.64, 123.89, 121.53, 120.26, 118.98, 117.77, 105.60, 105.39, 103.97, 103.89, 19.07, 11.75. Structure confirmed by single crystal X-ray diffraction.
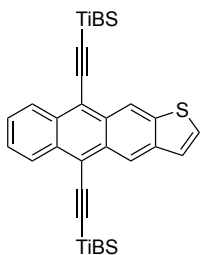
1c TIBS TA: Prepared via **General Procedure A**. 78% yield. ^{1}H NMR (400 MHz, CDCl$_3$): δ 9.17 (s, 1H), 9.11 (s, 1H), 8.6 (dt, J$_{HH}$ = 4.87 Hz, 2.49 Hz, 2H), 7.57-7.54 (m, 3H), 7.43 (d, J$_{HH}$ = 5.48 Hz, 1H), 2.11 (dtd, J$_{HH}$ = 13.33 Hz, 6.67 Hz, 1.46 Hz, 6H), 1.13 (d, J$_{HH}$ = 6.58 Hz, 36H), 0.91 (d, J$_{HH}$ = 6.97 Hz, 12H). ^{13}C NMR (101 MHz, CDCl$_3$): δ 140.13, 139.81, 132.41, 132.24, 130.19, 130.11, 129.92, 127.45, 127.41, 126.63, 126.51, 123.77, 121.48, 120.26, 118.97, 108.35, 108.10, 103.91, 26.63, 26.61, 25.49. Structure confirmed by single crystal X-ray diffraction.
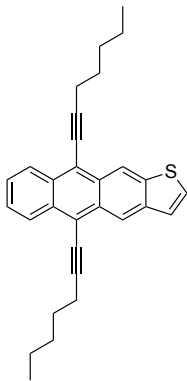
1d Heptynyl TA: Prepared via **General Procedure A**. 78% yield. ^{1}H NMR (400 MHz, C_6D_6): δ 9.509 (s, 1H), 9.364 (s, 1H), 8.922 (m, 2H), 7.388 (dd, J_{HH} = 6.69 Hz, 3.16 Hz, 2H), 7.084 (d, J_{HH} = 5.65 Hz, 1H), 6.896 (d, J_{HH} = 5.64 Hz, 1H), 2.530 (t, J_{HH} = 7.08 Hz, 2H), 2.461 (t, J_{HH} = 7.05 Hz, 2H), 1.603 (dt, J_{HH} = 19.96 Hz, 7.50 Hz, 4H), 1.446 (m, 4H), 1.285 (qd, J_{HH} = 7.34 Hz, 4.34 Hz, 4H), 0.907 (q, J_{HH} = 7.04 Hz, 6H). ^{13}C NMR (101 MHz, C_6D_6): δ 140.37, 139.98, 132.76, 132.64, 130.62, 130.59, 129.74, 126.49, 126.40, 123.80, 121.92, 120.62, 119.53, 118.43, 104.08, 103.95, 78.85, 78.66, 31.65, 29.11, 29.03, 22.62, 20.55, 20.44, 14.32, 14.29. Structure confirmed by single crystal X-ray diffraction.

1e Octynyl TA: Prepared via **General Procedure A**. 71% yield. ^{1}H NMR (400 MHz, C_6D_6): δ 9.524 (s, 1H), 9.385 (s, 1H), 8.937 (m, 2H), 7.396 (m, 2H), 7.095 (d, J_{HH} = 5.65 Hz, 1H), 6.898 (d, J_{HH} = 5.63 Hz, 1H), 2.548 (t, J_{HH} = 7.02 Hz, 2H), 2.478 (t, J_{HH} = 6.94 Hz, 2H), 1.611 (dt, J_{HH} = 20.72 Hz, 7.19 Hz, 4H), 1.486 (dd, J_{HH} = 14.82 Hz, 7.51 Hz, 4H), 1.281 (tdd, J_{HH} = 11.11 Hz, 4.69 Hz, 6.30 Hz, 8H), 0.912 (m, 6H). ^{13}C NMR (101 MHz, C_6D_6): δ 140.39, 140.00, 132.79, 132.64, 130.63, 130.61, 129.77, 126.51, 126.41, 123.79, 121.93, 120.63, 119.54, 118.45, 104.10, 103.98, 78.88, 78.69, 31.74, 29.38, 29.29, 29.16,

23.06, 23.02, 20.59, 20.48, 14.37, 14.33. Structure confirmed by single crystal X-ray diffraction.
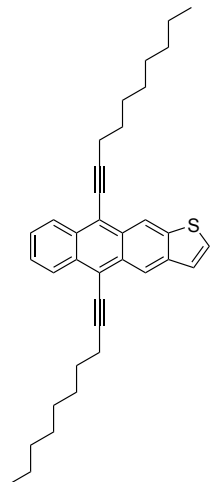
1f Decynyl TA: Prepared via **General Procedure A**. 82% yield. ^{1}H NMR (400 MHz, C_6D_6): δ 9.536 (s, 1H), 9.400 (s, 1H), 8.950 (m, 2H), 7.405 (m, 2H), 7.100 (d, J_{HH} = 5.66 Hz, 1H), 6.899 (d, J_{HH} = 5.64 Hz, 1H), 2.569 (t, J_{HH} = 7.03 Hz, 2H), 2.498 (t, J_{HH} = 6.97 Hz, 2H), 1.638 (td, J_{HH} = 14.21 Hz, 7.04 Hz, 4H), 1.517 (s, 4H), 1.297 (s, 12H), 0.915 (d, J_{HH} = 6.83 Hz, 6H). ^{13}C NMR (101 MHz, C_6D_6): δ 140.40, 140.01, 132.80, 132.66, 130.65, 130.62, 129.77, 126.52, 126.43, 123.80, 121.95, 120.65, 119.55, 118.46, 104.13, 104.00, 78.90, 78.71, 32.28, 32.26, 29.77, 29.72, 29.57, 29.53, 29.52, 29.45, 29.35, 23.12, 20.62, 20.51, 14.41, 14.38. Structure confirmed by single crystal X-ray diffraction.
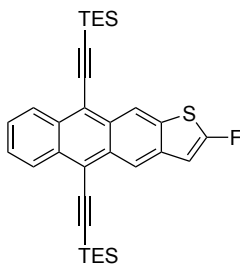
2a F TES TA: Prepared via **General Procedure A**. 70% yield. ^{1}H NMR: (400 MHz, C_6D_6): δ 9.21 (s, 1H), 9.04 (s, 1H), 8.96-8.90 (m, 2H), 7.37-7.32 (m, 2H), 6.25 (d, J_{HH} = 2.6 Hz, 1H), 1.22 (dt, J_{HH} = 16.15 Hz, 8.01 Hz, 18H), 0.82 (dq, J_{HH} = 21.1 Hz, 7.9 Hz, 12H). ^{13}C NMR (101 MHz, CDCl$_3$): δ 161.77, 132.89, 132.62, 130.99, 130.48, 130.45, 128.69, 128.18, 127.94, 127.71, 127.60, 127.23, 17.16, 121.43, 121.34, 120.94, 106.56,

106.51, 103.98, 102.95, 8.06, 8.01, 5.12, 5.04. 19F NMR (376 MHz, C_6D_6): δ -117.72. Structure confirmed by single crystal X-ray diffraction.
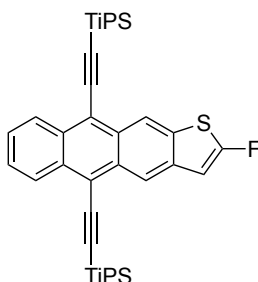
2b F TIPS TA: Prepared via **General Procedure A**. 80% yield. ^{1}H NMR (400 MHz, C_6D_6): δ 9.24 (s, 1H), 9.07 (s, 1H), 8.97-8.91 (m, 2H), 7.37-7-31 (m, 2H), 6.34 (d, J_{HH} = 2.56 Hz, 1H), 1.34-1.26 (m, 42H). ^{13}C NMR (101 MHz, $CDCl_3$): δ 167.51, 164.56, 137.16, 137.09, 134.45, 132.95, 132.68, 131.15, 130.66, 130.63, 128.70, 127.66, 127.55, 127.23, 127.17, 121.42, 121.34, 120.94, 118.89, 118.88, 118.27, 105.55, 105.50, 104.63, 104.42, 103.08, 102.97, 19.14, 19.10, 11.96, 11.92. 19F NMR (376 MHz, C_6D_6): δ -117.68. Structure confirmed by single crystal X-ray diffraction.
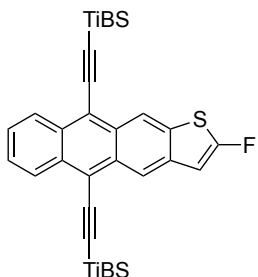
2c F TIBS TA: Prepared via **General Procedure A**. 75% yield. ^{1}H NMR (400 MHz, C_6D_6): δ 9.23 (s, 1H), 9.06 (s, 1H), 8.95-8.89 (m, 2H), 7.39-7.33 (m, 2H), 6.44 (d, J_{HH} = 2.50 Hz, 1H), 2.17 (dsextet, J_{HH} = 13.38 Hz, 6.69 Hz, 6H), 1.19 (dd, J_{HH} = 6.59 Hz, 1.11 Hz, 36H), 0.92 (dd, J_{HH} = 13.9 Hz, 6.93 Hz, 12H). ^{13}C NMR (101 MHz, $CDCl_3$): δ 167.66, 164.71, 137.12, 137.05, 134.40, 132.99, 132.68, 131.15, 130.67, 130.64, 127.67, 127.59, 127.15, 127.10, 121.42, 121.33, 121.01, 118.91, 118.33, 108.39, 108.26, 104.56, 104.38, 102.96, 102.85, 26.713, 26.69, 25.73, 25.65. 19F NMR (376 MHz, C_6D_6): δ -117.56. Structure confirmed by single crystal X-ray diffraction.
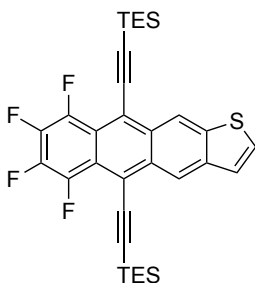
3a 4F TES TA: Prepared via **General Procedure A**. 68% yield. ^{1}H NMR (400 MHz, C$_6$D$_6$): δ 9.684 (s, 1H), 9.461 (s, 1H), 7.060 (dd, J_{HH} = 5.64 Hz, 0.50 Hz, 1H), 6.870 (d, J_{HH} = 5.62 Hz, 1H), 1.256 (dt, J_{HH} = 9.37 Hz, 7.89 Hz, 18H), 0.844 (dq, J_{HH} = 16.12 Hz, 8.01 Hz, 12H). ^{13}C NMR (101 MHz, C$_6$D$_6$): δ 143.49, 141.98, 138.57, 131.85, 131.44, 125.31, 125.19, 123.72, 121.59, 120.43, 118.53, 95.46, 93.68, 7.96, 4.93. Structure confirmed by single crystal X-ray diffraction.
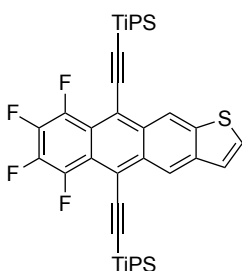
3b 4F TIPS TA: Prepared via **General Procedure A**. 72% yield. ^{1}H NMR (400 MHz, CD$_2$Cl$_2$): δ 9.376 (s, 1H), 9.317 (s, 1H), 7.689 (d, J_{HH} = 5.64 Hz, 1H), 7.471 (dd, J_{HH} = 5.65 Hz, 0.51 Hz, 1H), 1.266 (dd, J_{HH} = 5.40 Hz, 2.13 Hz, 42H). ^{13}C NMR (101 MHz, CD$_2$Cl$_2$): 141.88, 141.65, 140.72, 131.80, 131.20, 130.98, 127.41, 127.28, 123.97, 121.67, 120.46, 115.57, 115.44, 111.32, 108.51, 93.78, 92.00, 18.92, 11.95. Structure confirmed by single crystal X-ray diffraction.
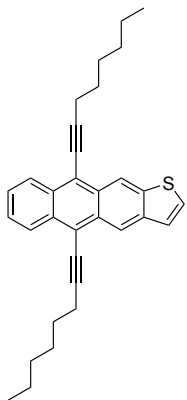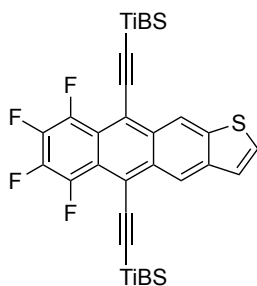
3c 4F TIBS TA: Prepared via **General Procedure A**. 70% yield. ^{1}H NMR (400 MHz, CD$_2$Cl$_2$): δ 9.342 (s, 1H), 9.260 (s, 1H), 7.694 (d, J_{HH} = 5.61 Hz, 1H), 7.478 (dd, J_{HH} = 5.65 Hz, 0.52 Hz, 1H), 2.072 (dquintet, J_{HH} = 13.34 Hz, 6.68 Hz, 0.93 Hz, 6H), 1.093 (dd, J_{HH} = 6.59 Hz, 0.74 Hz, 36H), 0.894 (dd, J_{HH} = 6.94 Hz, 2.34 Hz, 12H). ^{13}C NMR (101 MHz, CD$_2$Cl$_2$): 147.79, 141.81, 141.61, 135.69, 131.84, 130.90, 130.41, 128.35, 123.87, 123.57, 121.59, 120.44, 118.05, 115.13, 112.74, 110.04, 101.34, 100.52, 26.52, 25.62, 25.61, 25.41.
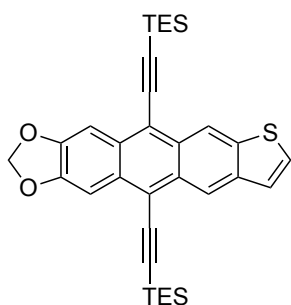
4a TES TA dioxolane: Prepared via **General Procedure A**. 81% yield. ^{1}H NMR (400 MHz, C$_6$D$_6$): δ 9.514 (s, 1H), 9.351 (s, 1H), 8.260 (s, 1H), 8.254 (s, 1H), 7.060 (dd, J_{HH} = 5.64 Hz, 0.54 Hz, 1H), 6.861 (d, J_{HH} = 5.62 Hz, 1H), 5.152 (s, 2H), 1.215 (dt, J_{HH} = 13.19 Hz, 7.89 Hz, 18H), 0.787 (m, 12H). ^{13}C NMR (101 MHz, C$_6$D$_6$): δ 149.897, 149.819, 140.215, 139.978, 138.217, 132.094, 131.775, 131.615, 129.731, 129.563, 123.810, 121.418, 120.206, 120.126, 117.823, 116.819, 102.429, 102.320, 101.454, 8.081, 8.052, 5.085, 5.013. Structure confirmed by single crystal X-ray diffraction.
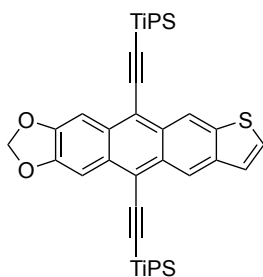
4b TIPS TA dioxolane: Prepared via **General Procedure A**. 83% yield. ^{1}H NMR (400 MHz, CDCl$_3$): δ 9.093 (s, 1H), 9.051 (s, 1H), 7.892 (s, 2H), 7.537 (d, J$_{HH}$ = 5.64 Hz, 1H), 7.429 (d, J$_{HH}$ = 5.64 Hz, 1H), 6.128 (s, 2H), 1.287 (d, J$_{HH}$ = 4.70 Hz, 42H). ^{13}C NMR (101 MHz, CDCl$_3$): δ 149.29, 149.19, 139.57, 131.17, 130.94, 130.92, 129.30, 129.23, 123.87, 121.05, 119.75, 117.38, 116.25, 104.49, 104.26, 104.11, 104.03, 102.20, 102.09, 101.59, 101.58, 19.05, 11.67. Structure confirmed by single crystal X-ray diffraction.
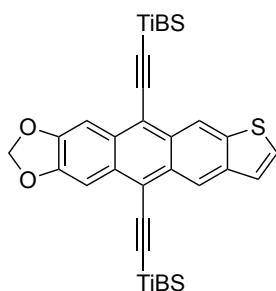
4c TIBS TA dioxolane: Prepared via **General Procedure A**. 80% yield. ^{1}H NMR (400 MHz, CDCl$_3$): δ 9.07 (s, 1H), 9.0 (s, 1H), 7.85 (s, 2H), 7.53 (d, J$_{HH}$ = 5.59 Hz, 1H), 7.41 (d, J$_{HH}$ = 5.63 Hz, 1H), 6.12 (s, 2H), 2.07-2.13 (m, 6H), 1.12 (d, J$_{HH}$ = 6.58 Hz, 36H), 0.89 (d, J$_{HH}$ = 6.93 Hz, 12H). ^{13}C NMR (101 MHz, CDCl$_3$): δ 148.85, 148.74, 139.06, 138.60, 130.67, 128.82, 128.75, 123.27, 120.51, 119.26, 116.87, 115.77, 106.75, 106.54, 103.56, 103.48, 101.62, 101.55, 101.12, 26.11, 24.98, 24.94, 24.92. Structure confirmed by single crystal X-ray diffraction.
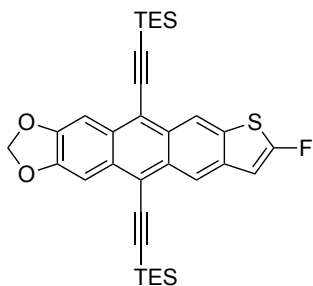
5a F TES TA dioxolane: Prepared via **General Procedure A**. 75% yield. ^{1}H NMR (400 MHz, C$_6$D$_6$): δ 9.176 (d, J$_{HH}$ = 0.74 Hz, 1H), 9.016 (s, 1H), 8.252 (s, 1H), 8.234 (d, J$_{HH}$ = 0.33 Hz, 1H), 6.278 (d, J$_{HH}$ = 2.65 Hz, 1H), 5.152 (s, 2H), 1.206 (dt, J$_{HH}$ = 16.97 Hz, 7.90 Hz, 18H), 0.785 (m, 12H). ^{13}C NMR (101 MHz, CD$_2$Cl$_2$): 149.88, 149.85, 136.37, 133.46, 131.21, 130.99, 129.69, 129.18, 120.74, 120.65, 120.29, 116.94, 116.33, 106.14, 105.92, 103.13, 103.01, 102.28, 102.16, 102.08, 100.37, 7.89, 4.95. Structure confirmed by single crystal X-ray diffraction.
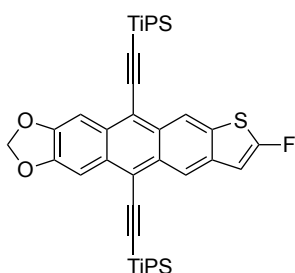
5b F TIPS TA dioxolane: Prepared via **General Procedure A**. 71% yield. ^{1}H NMR (400 MHz, CDCl$_3$): δ 8.864 (s, 1H), 8.804 (s, 1H), 7.867 (s, 2H), 6.771 (d, J$_{HH}$ = 2.37 Hz, 1H), 6.123 (s, 2H), 1.271 (d, J$_{HH}$ = 5.79 Hz, 42H). Structure confirmed by single crystal X-ray diffraction.
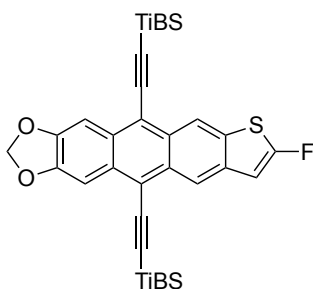
5c F TIBS TA dioxolane: Prepared via **General Procedure A**. 73% yield. ^{1}H NMR (400 MHz, CDCl$_3$): δ 8.850 (s, 1H), 8.767 (s, 1H), 7.834 (d, J$_{HH}$ = 3.05 Hz, 2H), 6.759 (d, J$_{HH}$

= 2.37 Hz, 1H), 6.131 (s, 2H), 6.12 (s, 2H), 2.084 (dt, J_{HH} = 13.29 Hz, 6.64 Hz, 6H), 1.118 (d, J_{HH} = 6.60 Hz, 36H), 0.879 (d, J_{HH} = 6.95 Hz, 12H). ^{13}C NMR (101 MHz, CDCl$_3$): δ 149.39, 149.34, 131.06, 130.78, 130.76, 129.68, 129.20, 129.13, 121.09, 120.55, 120.44, 120.12, 120.09, 116.28, 107.29, 107.12, 103.70, 102.15, 102.09, 101.66, 26.59, 25.48, 25.46, 25.36. Structure confirmed by single crystal X-ray diffraction.
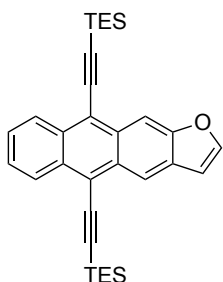
6a TES FA: Prepared via **General Procedure A**. 81% yield. ^{1}H NMR (400 MHz, CDCl$_3$): δ 8.876 (s, 1H), 8.697 (s, 1H), 8.613 (q, J_{HH} = 4.63, 2H), 7.799 (d, J_{HH} = 2.31 Hz, 1H), 7.56-7.59 (m, 2H), 6.964 (dd, J_{HH} = 2.36 Hz, 0.98 Hz, 1H), 1.216 (t, J_{HH} = 7.88 Hz, 18H), 0.881 (q, J_{HH} = 7.53 Hz ,12H). ^{13}C NMR (101 MHz, CDCl$_3$): δ 154.90, 148.95, 132.08, 131.65, 130.97, 130.58, 129.85, 127.33, 127.14, 126.65, 126.40, 118.71, 118.25, 106.75, 106.09, 105.92, 103.36, 103.18, 7.95, 4.80. Structure confirmed by single crystal X-ray diffraction.
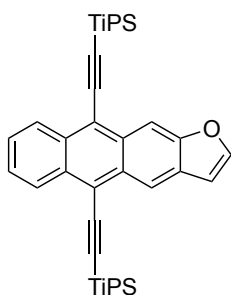
6b TiPS FA: Prepared via **General Procedure A**. 79% yield. ^{1}H NMR (400 MHz, CDCl$_3$): δ 8.919 (s, 1H), 8.731 (s, 1H), 8.651 (q, J_{HH} = 4.83 Hz, 2H), 7.801 (d, J_{HH} = 2.40 Hz, 1H), 7.581 (m, 2H), 6.950 (d, J_{HH} = 1.81 Hz, 1H), 1.302 (m, 42H). ^{13}C NMR (101 MHz, CDCl$_3$): δ 154.89, 148.92, 132.19, 131.74, 130.56, 129.99, 127.35, 127.15, 126.62, 126.36, 118.68, 118.36, 106.75, 105.91, 105.06, 104.89, 104.11, 103.94, 19.06, 11.68. Structure confirmed by single crystal X-ray diffraction.
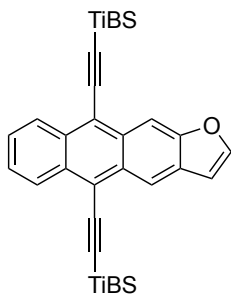
6c TiBS FA: Prepared via **General Procedure A**. 75% yield. ^{1}H NMR (400 MHz, CDCl$_3$): δ 8.874 (s, 1H), 8.687 (s, 1H), 8.597 (dd, J$_{HH}$ = 9.02 Hz, 4.83 Hz, 2H), 7.798 (d, J$_{HH}$ = 2.31 Hz, 1H), 7.555 (m, 2H), 6.925 (d, J$_{HH}$ = 2.36 Hz, 1H), 2.099 (dquintet, J$_{HH}$ = 13.31 Hz, 6.66 Hz, 6H), 1.122 (dd, J$_{HH}$ = 6.61 Hz, 0.75 Hz, 36H), 0.900 (d, J$_{HH}$ = 6.97 Hz, 12H). ^{13}C NMR (101 MHz, CDCl$_3$): δ 154.91, 148.96, 132.17, 131.69, 131.06, 130.50, 129.98, 127.35, 127.15, 126.48, 126.23, 118.71, 107.83, 107.70, 106.64, 105.91, 104.06, 103.85, 26.61, 25.45, 25.41. Structure confirmed by single crystal X-ray diffraction.

Chapter 3: Heteroacenes with Ligand Groups for Singlet Fission

3.1: Singlet Fission of Heteroacenes

As introduced in Chapter 1.6, singlet fission may be advantageously applied to photovoltaics by pairing a singlet fission material with a triplet acceptor. This system allows the Shockley Queisser limit to be circumvented to increase the maximum PCE of a single junction solar cell by more efficiently utilizing higher energy photons.

Singlet fission is well-documented among acenes;[1] in TiPS Tetracene, this process is endothermic by approximately 200-300 meV.[2] Recall that for singlet fission, endothermic means that the singlet energy is less than double the triplet energy. Some thienoanthracenes also exhibit singlet fission (SF), and this process has been found by collaborators to also be endothermic by varying amounts, depending on the derivative. This chapter will discuss the synthesis of heteroacenes with carboxylic acid groups, allowing them to function as ligands on quantum dots that act as triplet acceptors.

3.2: Incorporation of Ligand Moieties for Triplet Transfer

Organic semiconductor materials that exhibit singlet fission can be utilized in conjunction with a triplet acceptor, such as lead sulfide quantum dots (PbS QDs). Work by the Rao group at Cambridge has recently shown that tetracene-based ligands, specifically carboxylic acid-functionalized TiPS tetracene (TiPS Tet COOH) undergoes singlet fission and transfers the produced triplets to PbS QDs very efficiently.[2] The stages of this process are shown in Figure 3.1, below.
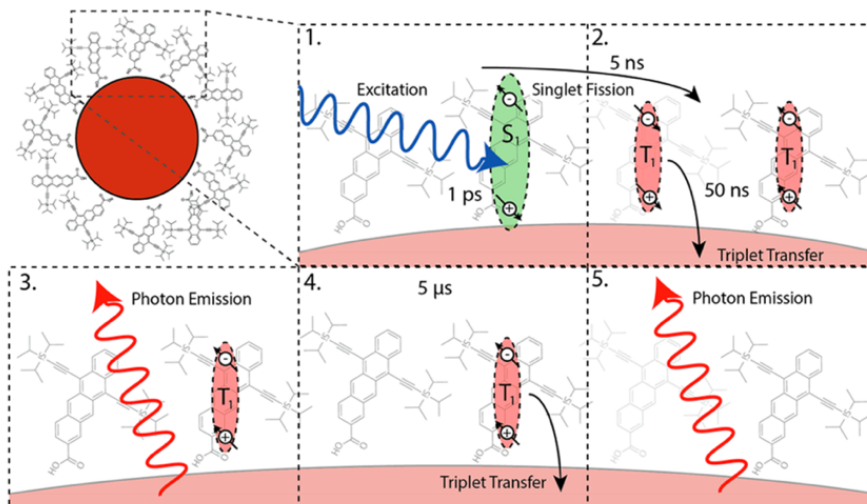
Figure 3.1: Process of singlet fission and triplet transfer in TiPS Tet COOH.[2]
Reprinted with permission from Davis et. al. 2018, DOI: 10.1021/acs.jpclett.8b00099. Copyright 2018 American Chemical Society.

The first step, shown in Panel 1 of Figure 3.1, is the excitation of TiPS Tet COOH by an absorbed high-energy photon, producing an excited singlet (S_1). This singlet exciton can be reversibly converted to an entangled triplet pair (TT) with overall singlet spin, and this pair may then split to form two triplet excitons on adjacent molecules in the T_1 state. The first of the triplets is transferred to the QD, and a low-energy photon is emitted from the QDs, as shown in Panels 2 and 3. The second triplet is then transferred and a second photon is emitted; a successful triplet transfer is always sequential and not simultaneous, as the latter could lead to triplet-triplet annihilation. These emitted photons may then be absorbed by a traditional inorganic solar cell, if it has the appropriate band gap for these photons. In theory, each high-energy photon absorbed by the singlet fission material leads to the emission of two lower-energy photons from the QDs.

Efficient transfer of triplets from acenes to quantum dots has been previously demonstrated,[3] though it is not necessarily expected that all acenes attached as ligands to QDs would undergo singlet fission, given the sensitivity of fission to the material's photophysical properties and crystal packing[4] (which may be influenced by the presence of the additional functional groups necessary for the acenes to act as ligands). However, TiPS Tetracene and TiPS Tet COOH have proven capable of undergoing singlet fission, and thus it is hoped that other acene ligands will do so as well.

Further demonstration of this system is shown in Figure 3.2. The photoluminescence quantum efficiency (PLQE, a ratio of the photons emitted per photons absorbed) of this PbS QD-tetracene system was found to be 9% when excited at 785 nm (where photons would only be absorbed by the QDs and TiPS unaffected) and 17% at 532 nm, where instead photons are primarily absorbed by TiPS Tet COOH and allowing for singlet fission and transfer of the produced triplets to the QD, and finally emission, which overall increases the PLQE. Because the PLQE is very nearly doubled, it is apparent that singlet fission and triplet transfer are occurring. This is depicted in Figure 3.2. Despite the PLQE doubling due to the singlet fission and triplet transfer of TiPS Te COOH, it is noted that the overall PLQE is low due to poor ligand coverage on the quantum dots, and it is suspected that a compound that gives better ligand coverage could lead to higher PLQE values.[5] Further, the maximum luminescence at approximately 1250 nm corresponds to emitted photons of 0.99 eV, which is lower than desired for incorporation with silicon. The energy levels of both the ligand molecule and the quantum dots must be carefully tuned to produce photons of the desired energy.
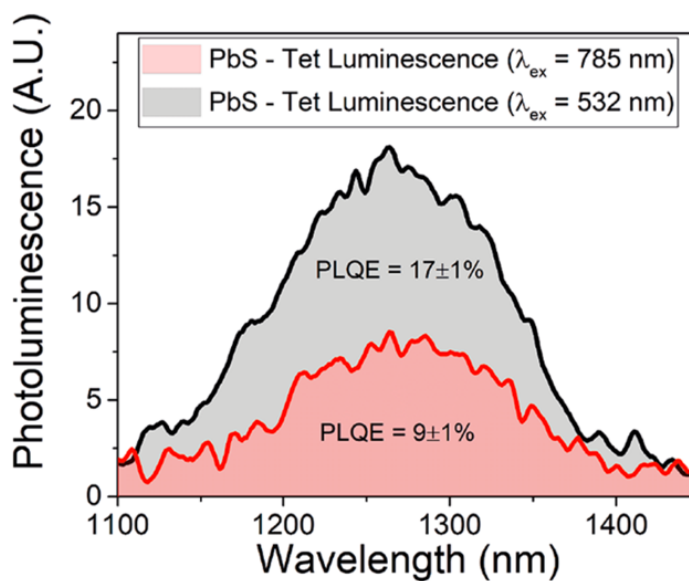
Figure 3.2: PLQE of PbS QD-tetracene.[2] Reprinted with permission from Davis et. al. 2018, DOI: 10.1021/acs.jpclett.8b00099. Copyright 2018 American Chemical Society.

In order for this system to work in conjugation with a silicon photovoltaic, which is the end goal, the energy levels of the organic material and the emission wavelength of the quantum dots must be carefully controlled to complement that of silicon. If we consider

that the photons emitted by the quantum dots need to be at least 1.1 eV to be utilized by silicon, and assume that there may be some energy loss between the QDs absorbing the produced triplets and emitting photons, then the target triplet energy should be at least 1.3 eV. Further assuming that the organic material undergoes endothermic SF, then the target singlet energy for the organic material should be approximately double the triplet energy minus 0.2-0.3 eV to account for the endothermicity, which is preferred over exothermic SF to avoid too much energy loss. This puts the target singlet energy at approximately 2.3-2.5 eV. Obviously, there are many assumptions being made here, but aiming for this general value should put the synthesized materials in the correct energy range.

While the organic SF material/QD system appears to have significant potential, tetracene is typically quite unstable to prolonged exposure to light, as shown in the stability data in Chapter 2 (and shown again in the following sections). This is obviously unideal for photovoltaic applications, and thus a different chromophore with improved stability was sought for future work on this hybrid OSC/QD system. This led to our increasing interest in thienoanthracenes and other heteroacenes, which exhibit higher stability than tetracenes. The following sections outline efforts to functionalize TAs with carboxylic acid moieties, to compliment the previous work on TiPS Tet COOH, and develop similar structure-function relationships as those established in the heteroacenes of Chapter 2.

3.3: Initial and Optimized Synthetic Strategy

The TAs described in this chapter were synthesized according to General Procedure A, as shown below in Figure 3.3. All test reactions at this stage were conducted using R = TiPS, due to the availability and ease of storage of TiPS acetylene.
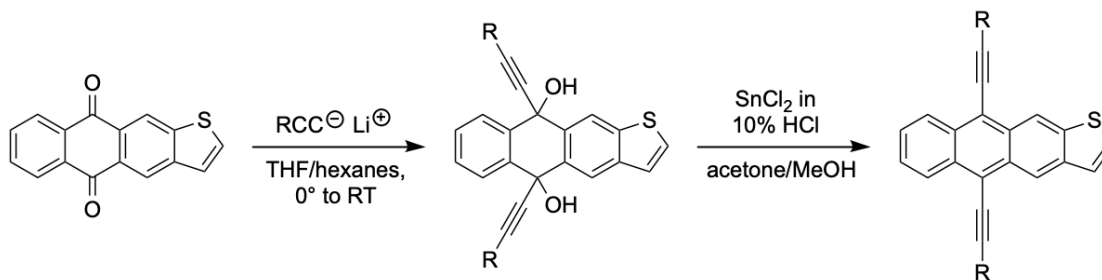
Figure 3.3: General Procedure A, the basic synthetic scheme to thienoanthracenes.

It was initially intended to directly functionalize the TAs with carboxylic acid groups with a simple metal-halogen exchange using butyllithium followed by quenching with carbon dioxide. As shown in Figure 3.4, this carboxylation strategy would provide a simple, one-step route to TA carboxylic acids. In order to install the halogen at the 2-position of the thiophene ring, 2-bromo- or 2-iodothiophene dialdehyde were synthesized according to literature conditions[6] and the corresponding quinones were prepared via the standard method.[7] The silylethynyl TAs were prepared according to General Procedure A as shown above, and the attempted carboxylation via metal-halogen exchange followed the conditions shown below in Figure 3.4.
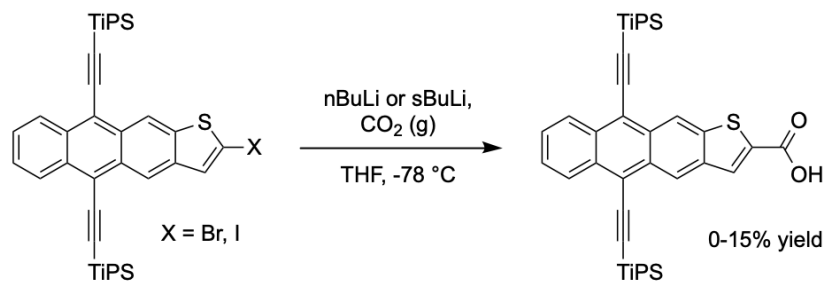
Figure 3.4: Initial carboxylation procedure.

However, it was quickly determined that these conditions were too aggressive, as the TAs decomposed during the reaction. Monitoring the reaction by TLC showed a bright yellow, highly fluorescent spot for the starting material and a lower-running, non-fluorescent spot for the reaction mixture. Unfortunately, using either the bromide or iodide with *n*-butyllithium or *sec*-butyllithium did not improve results. Only trace amounts of product were observed by TLC, along with significant decomposition.

Based on precedence from other similar syntheses in the group, it was decided to attempt the reaction on a methyl-protected intermediate rather than the aromatized TA. The methyl protection is straightforward and high yielding, as shown in Figure 3.5.
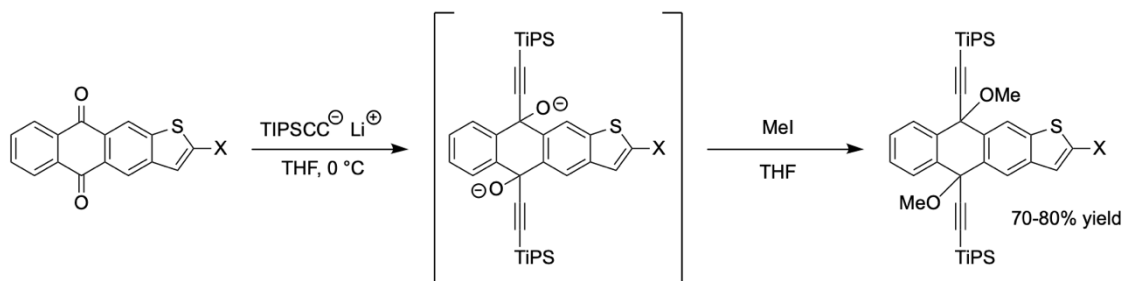
Figure 3.5: Synthesis of dimethoxy intermediate.

Additionally, n- or sec-BuLi were substituted for the gentler LiMg(n-butyl)$_2$-(iso)propyl),[8] which has been previously observed in our group to be an efficient and highly selective reagent for metal-halogen exchange. This scheme is shown in Figure 3.6.
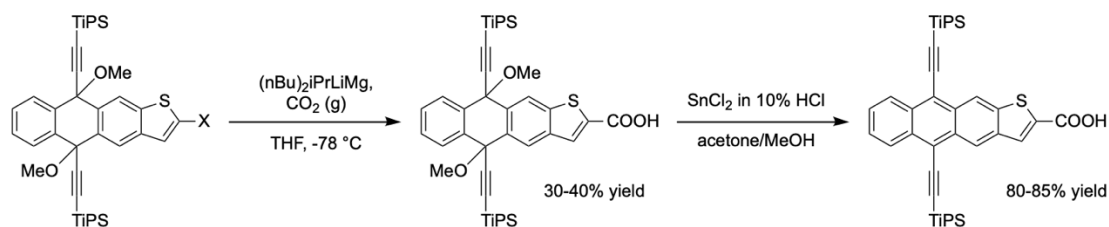
Figure 3.6: Synthesis of TiPS TA COOH via the dimethoxy intermediate.

These conditions afforded an isolable 30-40% yield of product at the carboxylation step, which was a notable improvement from the previous conditions, though still low overall. Concurrently, we sought a route to install the halogen later in the synthesis, as halogenating thiophene dialdehyde adds several steps to the reaction sequence. A method to brominate thienoanthracene quinone was identified in the literature.[9] This method was readily employed and found to be high-yielding, as reported.
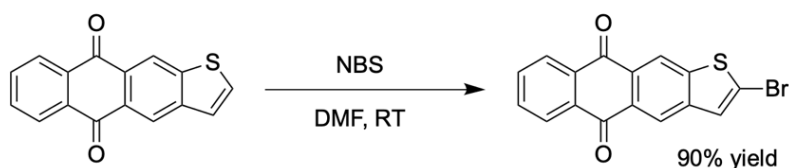
Figure 3.7: Bromination of TA quinone and expected product according to Ref. 8.

Conducting metal-halogen exchange on the brominated TAs, following the metal-halogen exchange procedure of Figure 3.6, yielded a red crystalline solid that was submitted for XRD and NMR. XRD revealed that the crystals submitted contained the

compound shown in Figure 3.8, with the carboxylic acid at the 2-position and a bromide at the 3-position. Unfortunately, this structure was solvable in terms of bare structural information, but was not able to be refined, leaving some ambiguity of what mix of compounds the crystals contained. Interestingly, the carbon NMR spectrum showed an impure mix of compounds with two distinct carboxylic acid peaks, and thus it was suspected that there was also some amount of another COOH isomer, though it was not clear if this was the 2-COOH without a bromide, or 3-COOH. Either would be possible from the reaction conditions used.
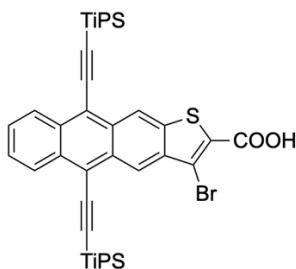
Figure 3.8: Unintended brominated product.

In an effort to clearly identify what went wrong, the TMS derivative of the brominated TA was synthesized and crystallized. From XRD, we were able to identify unambiguously that the bromide was indeed at the 3-position prior to carboxylation, demonstrating that the published reaction for brominating thienoanthracene quinone is, in fact, selective for the 3-position, not the 2-position as published. The reference paper did not include single crystal XRD analysis, only proton NMR, which is not sufficient to distinguish between the two different isomers.
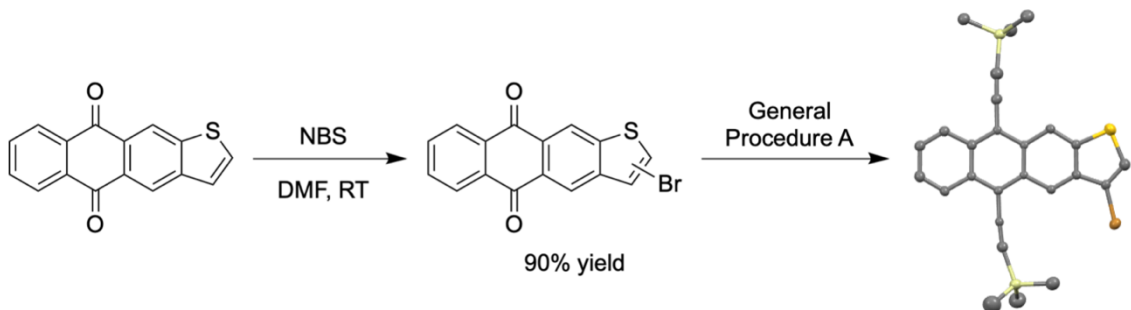
Figure 3.9: Actual bromination of TA quinone, followed by General Procedure A with TMS acetylene to obtain the crystal structure showing the unambiguous position of the bromide.

Despite the good yield of this bromination strategy, it was clear that attempting to carboxylate from the 3-bromide gave a mix of products and left an undesired bromide behind. Thus, we returned to halogenating at the thiophene dialdehyde stage. However, yields were still poor and this route required many synthetic steps, and alternative methods continued to be explored. To reduce the number of steps in the reaction sequence, we investigated deprotonation on the fully aromatized compound. Since it was previously determined that butyllithium reagents led to decomposition of the aromatized TAs when attempting metal-halogen exchange, lithium diisopropylamide (LDA) was used for deprotonation instead, which is gentler than butyllithium reagents and non-nucleophilic. Gratifyingly, this method worked quite well, with good conversion and minimal decomposition. While yields typically do not exceed about 60%, the starting material that remains is recoverable, and the carboxylic acid is obtained in only three steps from the quinone.
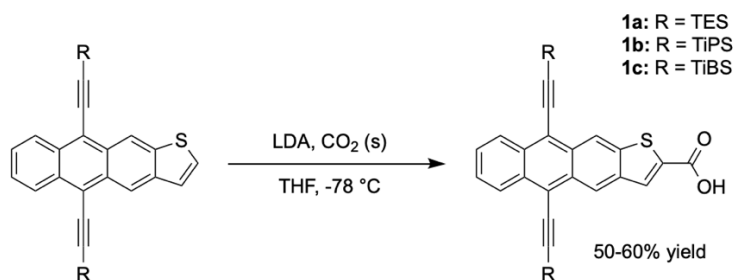
Figure 3.10: General Procedure B, carboxylation with LDA.

This carboxylation method proved the most successful, and a crystal structure of 1c was obtained. While purity was confirmed by NMR, 1a and 1b do not give crystals suitable for XRD, despite recrystallization in several different solvents. Efforts are ongoing to grow suitable crystals of 1a and 1b.
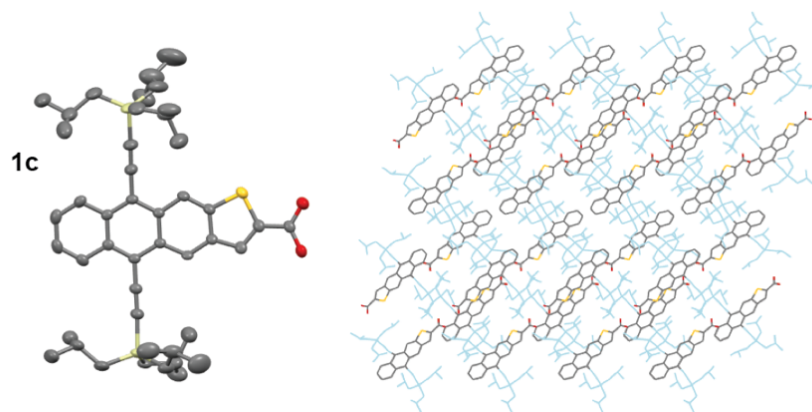
Figure 3.11: Ellipsoid structure and packing of 1c.

The structure and packing of 1c are shown in Figure 3.11. The packing shows a repeating pattern of four molecules with moderate π-surface overlap, with each group of four blocked from extended π-stacking by the next adjacent and perpendicular group of four molecules. Because each group of four is isolated, there is not true π-stacking in the structure of 1c. Within the group of four, the interplanar distance is approximately 3.5 Å, and there are some carbon-carbon close contacts observed. The carboxylic acid groups on adjacent molecules point towards each other, where O-H hydrogen bonding encourages this interaction through the packing motif.

3.4: Other Heteroacene Chromophores

Once carboxylation conditions were optimized, other chromophores were investigated. The TiPS TA dioxolane derivative reacted readily in the conditions of General Procedure B to give 2b, as shown in Figure 3.12. The TES and TiBS derivatives 2a and 2c have thus far not been prepared for other chromophores to simplify the investigations of the TA carboxylic acids, as the solubilizing groups do not have a significant, if any, effect on the energy levels of these materials, which are the primary interest.
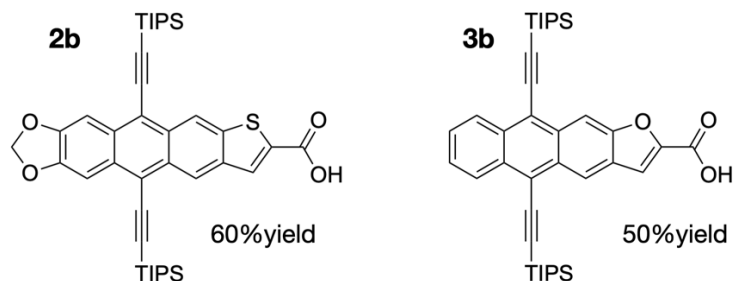
Figure 3.12: Structures of other heteroacene carboxylic acids.

The TA dioxolane 2b yielded a crystal structure, despite crystallizing in very fine needles. The ellipsoid structure and packing of 2b is shown in Figure 3.13 below.
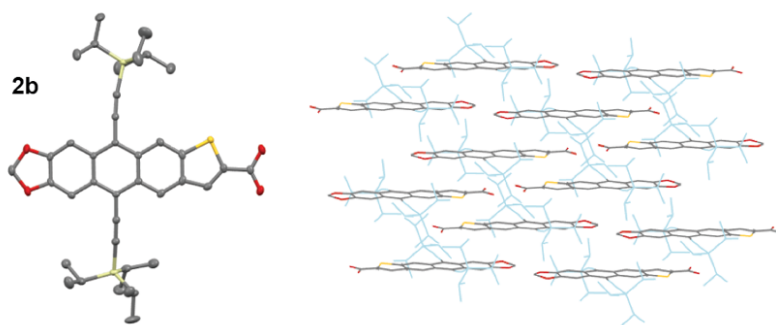
Figure 3.13: Ellipsoid structure and packing of 2b.

The packing of 2b appears to be 2D brickwork, with an interplanar distance of 3.441 Å. There are C-C close contacts (using the sum of the van der Waals plus 0.2 Å) between all of the molecules shown in the packing motif of Figure 3.12 and good π-surface overlap throughout the motif, with the carboxylic acids on adjacent molecules pointing towards each other, with hydrogen bonding enforcing this orientation.

The TiPS furanoanthracene carboxylic acid 3b was also prepared via the same route, as shown in Figure 3.12 on the right. Unfortunately, crystals of this compound have not been suitable for single crystal XRD analysis, and a crystal structure has not yet been obtained. Efforts to grow suitable crystals are ongoing.

Both of the crystal structures obtained, 1c and 2b, pack such that there is significant hydrogen bonding interaction between the carboxylic acid groups. This is depicted in Figure 3.14, and it is expected that the other acids will pack similarly, even if the overall orientation of the motif varies.
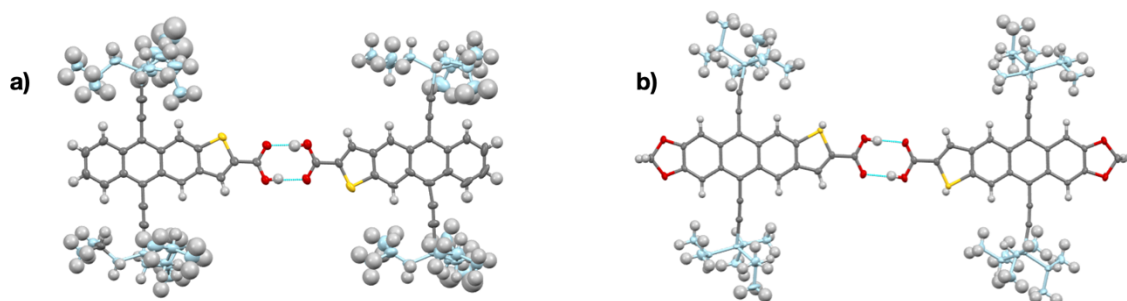
Figure 3.14: Hydrogen bonding between the carboxylic acid groups of 1c (a) and 2b (b).

3.5: Photophysical Characterization

The absorbance spectra of the carboxylic acids were obtained and compared to those of the parent molecules. The carboxylic acid group induces a clear red shift in each derivative, with the maximum absorbance of each of the carboxylic acids shifted relative to the parent molecule by approximately 20 nm. The absorbance of the synthesized derivatives 1a-c, 2b, and 3b is shown in Figure 3.14. The absorbance spectra of TiPS TA and TiPS Tet are also included for comparison.
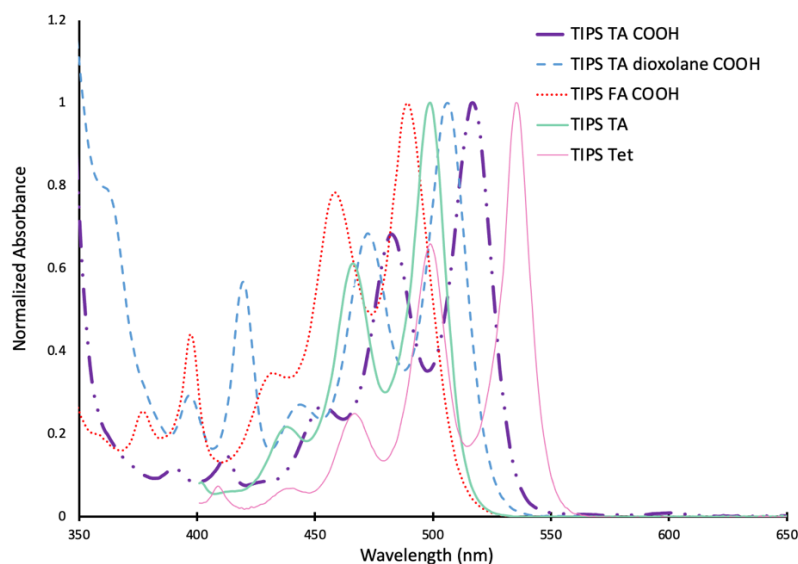
Figure 3.15: Absorbance spectra of the heteroacene carboxylic acids. Spectra were taken in DCE at RT at approximately 10 μM concentration.

As with the parent heteroacenes in Chapter 2, the presence or absence of solid-state fluorescence was noted for the carboxylic acids. Figure 3.15 shows the appearance of 1a, 1b, 1c, and 2b under long-wave UV light. As can be seen, none of the carboxylic acid

derivatives exhibit solid-state fluorescence. Following the assumption introduced in Chapter 2, but this is a preliminary indication that these molecules have the potential to undergo singlet fission.
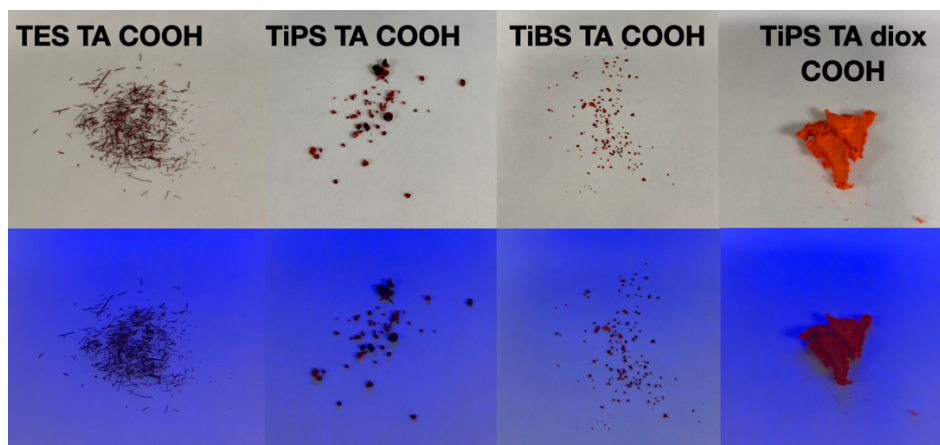
Figure 3.16: Absence of solid-state fluorescence in the carboxylic acids.

The solution fluorescence spectra were also measured. These are similarly shifted compared to the parent molecules, and the Stokes shift in both the carboxylic acids and the unsubstituted heteroacenes is approximately the same. The compared absorbance and fluorescence of each of the carboxylic acids is shown in Figure 3.16.
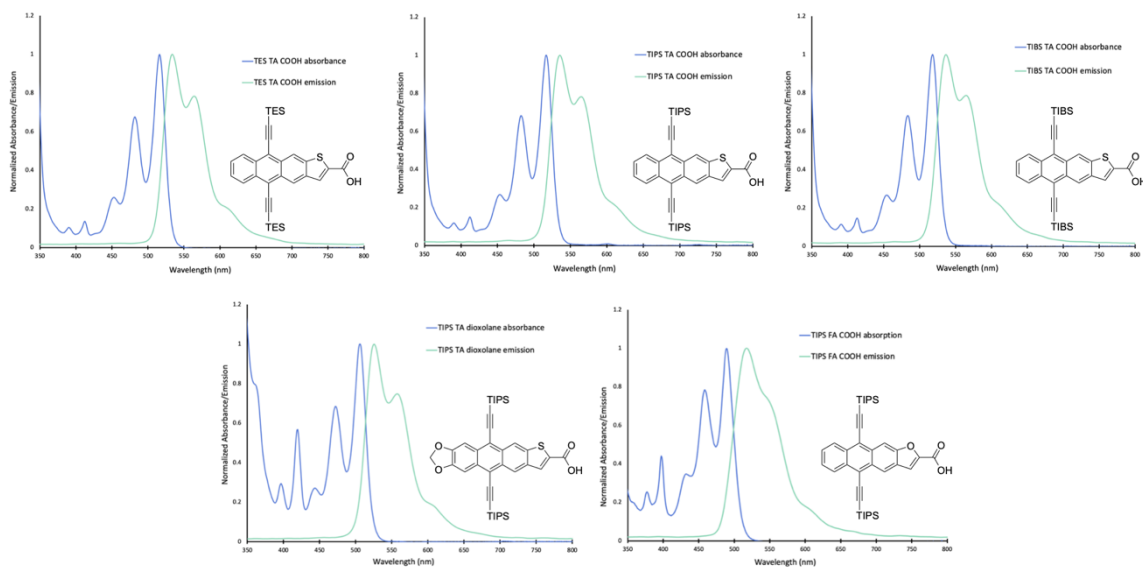
Figure 3.17: Absorbance vs emission spectra of the heteroacene carboxylic acids. Spectra were taken in DCE at RT at approximately 10 μM concentration.

Finally, the stability of the carboxylic acids was evaluated using the same method described in Chapter 2. The carboxylic acid group does not appear to have a negative effect on the stability of the compounds, with the TA derivatives exhibiting some decomposition

in solution, and the TA dioxolane derivative exhibiting no decomposition. The stability data are shown below in Figure 3.17 compared to TiPS TA and TiPS Tet, demonstrating the improved stability of the carboxylic acids compared to these two parent molecules, and illustrating the suitability of the heteroacene chromophores for photophysical applications over tetracenes, which exhibit poor stability upon exposure to light.
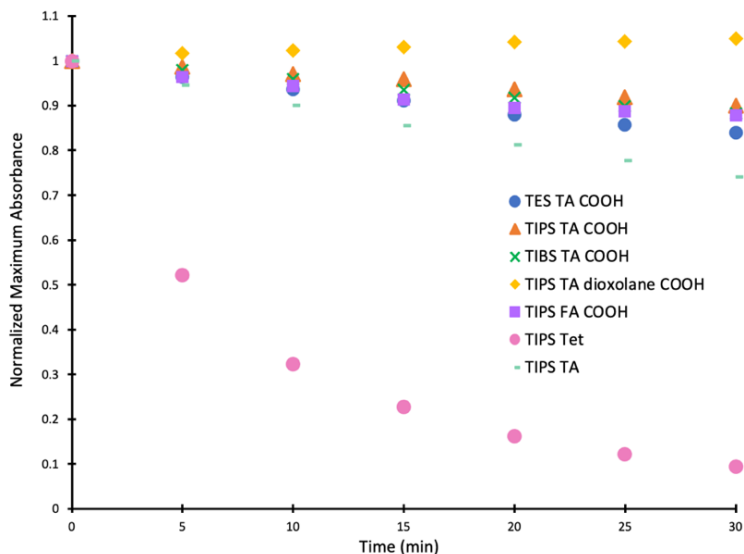
Figure 3.18: Stability of the heteroacene carboxylic acids. Spectra were taken in DCE at RT at approximately 10 μM concentration and the maximum absorbance was measured every five minutes for 30 minutes.

Using DFT calculations,[10] the triplet energies of the carboxylic acids and select parent molecules were determined. We expect that the computational values will differ from the experimental measurements but seek to identify trends along the heteroacene series. These triplet energies were obtained using DFT (tuned ωB97XD/6-31G*) and applying the Tamm-Dancoff Approximation[11] and were performed by Dr. Karl Thorley at UK. These values are summarized below, along with experimental singlet energies as estimated from the absorption edge. The properties of the parent molecules and TiPS Tetracene are shown in Table 3.1.

Table 3.1: Summary of optical properties of heteroacene parent molecules, along with experimentally calculated singlet energies and computationally determined singlet and triplet energies.

Compound	$\lambda_{max,abs}$ (nm)	$S_1 - S_0$ (eV) experimental	$S_1 - S_0$ (eV) computational	$T_1 - S_0$ (eV) computational
TiPS Tet	535	2.25	2.277	1.279 (1.25)
TiPS TA	498	2.41	2.515	1.524
F TiPS TA	482	2.48	2.570	1.570
4F TiPS TA	509	2.33	2.436	1.462
TiPS TA diox	485	2.48	2.606	1.647
F TiPS TA diox	471	2.55	2.658	1.692
TiPS FA	477	2.53	2.592	1.573

As can be determined from Table 3.1, singlet fission is predicted to be endothermic in the parent molecules. The computationally determined triplet energies scale predictably with the experimental properties; compounds with higher singlet energies are also predicted to have higher triplet energies. The experimental triplet energy of TiPS Tetracene is shown in parentheses and agrees well with the computational value. While the carboxylic acid analogues of all of these chromophores have not yet been prepared, we suspect that the relative energy levels will continue to scale in predictable ways based on the computational data. The experimental and computed values for the carboxylic acid derivatives synthesized are shown below in Table 3.2.

Table 3.2: Summary of optical properties of heteroacene carboxylic acids with experimentally calculated singlet energies and computational singlet triplet energies, and predicted endothermicity based on computational values.

Compound	$\lambda_{max,abs}$ (nm)	$S_1 - S_0$ (eV) experimental	$S_1 - S_0$ (eV) computational	$T_1 - S_0$ (eV) computational	Endothermicity (meV) computational
TiPS Tet COOH	570	2.17	2.247	1.264	281
TiPS TA COOH	517	2.28	2.424	1.465	506
TiPS TA diox COOH	506	2.34	2.511	1.585	659
TiPS FA COOH	489	2.38	2.498	1.498	498

As shown in Table 3.2, the singlet fission process is predicted to be highly endothermic in the carboxylic acids, as it is also predicted to be in the parent molecules. Considering the values shown, one might assume the singlet fission process to be prohibited due to the degree of endothermicity, though of course some variation between experimental and computational data is expected, as discussed below. Just as the carboxylic acid moiety induces a red-shift in the absorbance spectra, it is computationally predicted that it also lowers the triplet energy relative to the parent chromophore. Following the assumptions made above in section 3.2, these heteroacene carboxylic acids should, in theory, be capable of producing triplets of the energy that could be utilized in the QD/PV system. It is expected that much optimization will be required to apply this system in practice, but the potential utility of these materials is promising.

3.6: Experimental Singlet Fission Data

Data from collaborators on this project has indicated that one of the parent molecules, F TiBS TA, does undergo singlet fission, and that this process is endothermic. The triplet energy of F TiBS TA was found by transient absorption to be approximately 1.3 eV. Comparing this to the computational data in Table 3.3, there is significant discrepancy between the endothermicity using the DFT-calculated energy levels and those found experimentally. It this thus believed that the derivatives synthesized may yet be promising for endothermic singlet fission.

Table 3.3: Computational and experimental data for F TiBS TA.

Compound	S_0 to S_1 (eV) computational	S_0 to T_1 (eV) computational	Endothermicity (meV)	S_0 to S_1 (eV) experimental	S_0 to T_1 (eV) experimental	Endothermicity (meV)
F TiBS TA	2.570	1.570	570	2.48	1.3	120

Given the difference between computational and experimental data for this compound, it is expected that the carboxylic acids in Table 3.2 may show a similar difference when experimental data is obtained, though predictable trends cannot presently be established with only one compound to consider. Further collaborator data on other compounds, particularly the carboxylic acids synthesized in this chapter, has not yet been obtained, but it expected to shed light on the true energy levels of the singlet fission processes of these molecules.

3.7: Conclusions

These compounds and their parent molecules have been shipped to our esteemed collaborators at Cambridge University and are currently undergoing further study. Given the length of time and volume of material required for the completion of these studies, these molecules are expected to yield exciting results and be of the utmost importance towards advancing the hybrid organic SF/QD photovoltaic system.

This chapter presents an effective synthesis to carboxylic acid-functionalized heteroacenes and offers basic optical and energetic characterization. These data begin to demonstrate correlations between the carboxylic acid moiety and resulting properties, along with investigating the effect of the carboxylic acid on multiple chromophores.

3.8: Experimental

Solvents were purchased in bulk from VWR, and other reagents were purchased from commercial sources (typically Sigma Aldrich) and were used as received. NMR spectra were measured on a 400 MHz Bruker instrument, and chemical shifts are reported in ppm and referenced to the deuterated solvents used. Absorbance was measured with an Agilent Cary 60 UV-vis spectrometer and fluorescence measured with StellarNet Inc. fluorimeter. Crystal structures were collected and refined by Dr. Sean Parkin of UK using

a dual-microsource Bruker D8 Venture κ-axis diffractometer (MoKα & CuKα) with large-area 'Photon-II' CMOS detector.

General Procedure A: In a 0.1 M solution of hexanes/THF (9:1-3:1 ratio) in a flame-dried flask under nitrogen, 3.5 equivalents of silyl acetylene were dissolved. The reaction solution was cooled to 0 °C and 3 equivalents of LiHMDS were added dropwise. The solution was allowed to stir for 30 minutes to 1 hour, after which the quinone starting material was added in one portion. The reaction solution was stirred overnight, and upon completion as determined by TLC, was quenched with deionized water and extracted with hexanes. The organic layers were dried with magnesium sulfate and concentrated by rotary evaporation. This diol intermediate was typically observed as a yellow or colorless oil and was used immediately without further purification. The diol was dissolved in minimal acetone and diluted with 0.1 M methanol open to air. To this, 6 equivalents of $SnCl_2$ dissolved in minimal 10% H_2SO_4 was added in one portion. The reaction solution was allowed to stir for 1 hour and then was extracted with hexanes. The organic layers were dried with magnesium sulfate and concentrated via rotary evaporation. The resulting yellow, orange, or red solids were purified via chromatography with hexanes and recrystallized with acetone to give yellow or orange crystals.

Carboxylation via metal-halogen exchange: Iodo- or bromo-thienoanthracenes were dissolved in 0.1M anhydrous THF under nitrogen. The solution was cooled to -78 °C, and 1-2 equivalents of butyllithium were added dropwise. The reaction mixture was allowed to stir for 1-2 hours while cold, and then gaseous carbon dioxide was bubbled through. Completion of metal-halogen exchange (or decomposition) was evaluated by TLC. The reaction mixture was then quenched with 10% hydrochloric acid and extracted with ethyl acetate. The organic layers were dried with magnesium sulfate and concentrated by rotary evaporation. If any product was obtained, it was purified on silica using a gradient of hexanes and ethyl acetate.
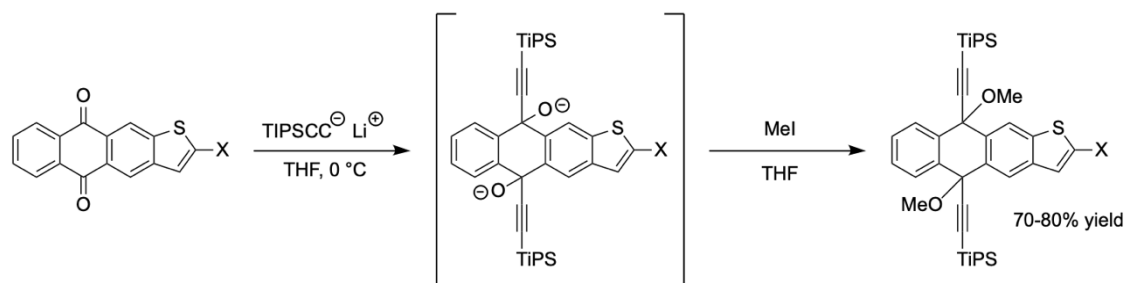
Dimethoxy TA intermediate: In a 0.1M solution of hexanes/THF (9:1-3:1 ratio) in a flame-dried flask under nitrogen, 3.5 equivalents of silyl acetylene were dissolved. The reaction solution was cooled to 0 °C and 3 equivalents of LiHMDS were added dropwise. The solution was allowed to stir for 30 minutes to 1 hour, after which the quinone starting material was added in one portion. The reaction solution was stirred overnight, and upon completion as determined by TLC, was quenched with methyl iodide and allowed to stir for an additional 30 minutes. Upon complete methylation by TLC, the reaction was extracted with hexanes and dichloromethane. The organic layers were dried with

66

magnesium sulfate and concentrated by rotary evaporation. The product was typically observed as a white or light pink solid.
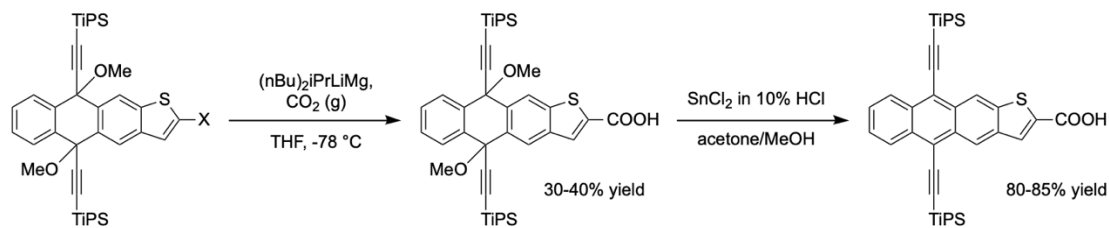
Carboxylation via dimethoxy intermediate: The dimethoxy starting material was dissolved in anhydrous THF under nitrogen in a flame-dried flask. The "LiMg reagent" (LiMg(n-butyl)$_2$-(isopropyl)) was prepared according to the method of Reference 7. The acene reaction mixture was cooled to -78 °C, and the LiMg reagent was added dropwise. The reaction mixture was stirred for approximately 1 hour, and then gaseous carbon dioxide was bubbled through. The reaction mixture was then quenched with 10% hydrochloric acid and extracted with ethyl acetate. The organic layers were dried with magnesium sulfate and concentrated by rotary evaporation. The dimethoxy-protected carboxylic acid was used in the next step without purification. The dimethoxy carboxylic acid was dissolved in minimal acetone and diluted with 0.1 M methanol open to air. To this, 6 equivalents of $SnCl_2$ dissolved in minimal 10% H_2SO_4 was added in one portion. The reaction solution was allowed to stir for 1 hour and then was extracted with ethyl acetate. The organic layers were dried with magnesium sulfate and concentrated via rotary evaporation. The resulting red solid was purified via chromatography with hexanes and ethyl acetate and isolated as a red powder.
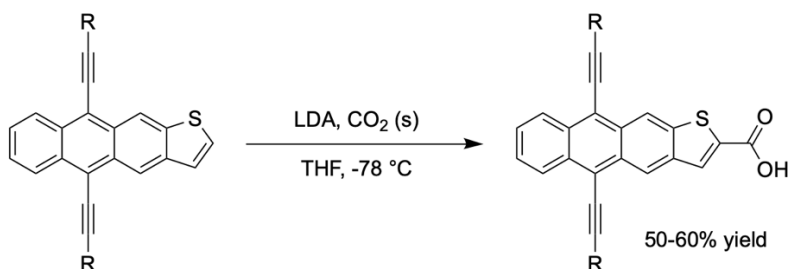
General Procedure B: In a flame-dried flask, the silylethynyl thienoanthracene was dissolved in 0.5M THF under nitrogen. The reaction mixture was cooled to -78 °C and 5

equivalents of 1M LDA were added dropwise, and the reaction mixture was stirred for approximately 45 minutes. Solid CO_2 (dry ice) was added in excess, and the reaction mixture was stirred for an additional 20 minutes. The reaction was quenched with 10% HCl and extracted with ethyl acetate. The organic layers were combined, dried with magnesium sulfate, and concentrated via rotary evaporation. The product was purified on silica with ethyl acetate and recrystallized with acetone to give small red crystals.
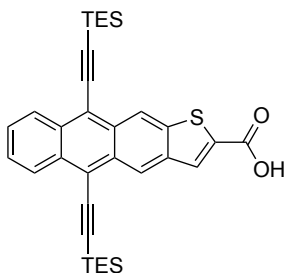
1a TES TA COOH: Prepared via **General Procedure B**. 50% yield. ^{1}H NMR (400 MHz, C_6D_6): δ 9.377 (s, 1H), 9.342 (s, 1H), 8.807 (dd, J_{HH} = 4.83 Hz, 3.56 Hz, 2H), 8.084 (s, 1H), 7.341 (d, J_{HH} = 9.51 Hz, 2H), 1.236 (q, J_{HH} = 7.65 Hz, 18H), 0.840 (dt, J_{HH} = 14.08 Hz, 7.34 Hz, 12H). MS calculated: 554.8896, found: 554.438.
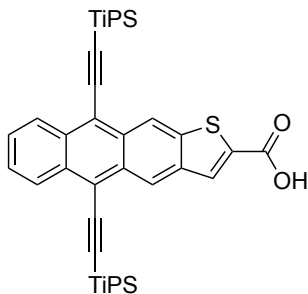
1b TIPS TA COOH: Prepared via **General Procedure B**. 52% yield. ^{1}H NMR (400 MHz, C_6D_6): δ 9.389 (d, J_{HH} = 0.95 Hz, 1H), 9.374 (s, 1H), 8.807 (m, 2H), 8.159 (s, 1H), 7.352 (s, 2H), 1.304 (d, J_{HH} = 4.37 Hz, 42H). ^{13}C NMR (101 MHz, $CDCl_3$): δ 166.569, 149.627, 140.551, 138.920, 135.157, 133.178, 132.824, 132.500, 131.263, 130.162, 127.553, 127.089, 125.376, 120.781, 119.806, 117.927, 106.672, 106.128, 103.442, 19.070, 18.862, 11.714, 11.351. MS calculated: 639.0491, found: 639.513.
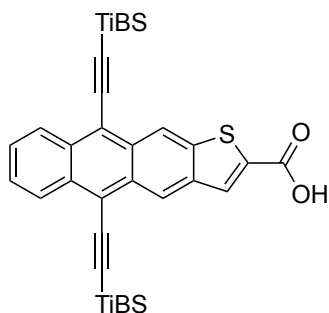
1c TIBS TA COOH: Prepared via **General Procedure B**. 55% yield. ^{1}H NMR (400 MHz, C$_6$D$_6$): δ 9.280 (d, J$_{HH}$ = 4.61 Hz, 2H), 8.671 (dd, J$_{HH}$ = 5.56 Hz, 3.05 Hz, 2H), 8.149 (s, 1H), 7.370 (m, 2H), 2.117 (dt, J$_{HH}$ = 13.31 Hz, 6.65 Hz, 6H), 1.155 (dd, J$_{HH}$ = 6.57 Hz, 0.63 Hz, 36H), 0.906 (dd, J$_{HH}$ = 6.86 Hz, 5.97 Hz, 12H). Structure confirmed by single crystal X-ray diffraction.
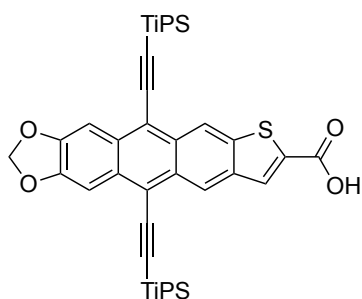
2b TIPS TA dioxolane COOH: Prepared via **General Procedure B**. 60% yield. ^{1}H NMR (400 MHz, CDCl$_3$): δ 9.190 (s, 1H), 9.088 (s, 1H), 8.252 (s, 1H), 7.878 (s, 2H), 6.141 (s, 2H), 1.287 (dd, J$_{HH}$ = 5.10 Hz, 2.79 Hz, 42H). Structure confirmed by single crystal X-ray diffraction.
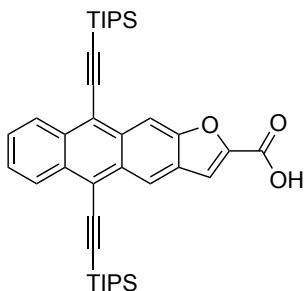
3b TIPS FA COOH: Prepared via **General Procedure B**. 50% yield. ^{1}H NMR (400 MHz, CDCl$_3$): δ resubmitted. MS calculated: 622.9835, found: 622.261.

Chapter 4: Heteroacenes for Isolated Triplet Pair Generation

Quantum computing involves the utilization of quantum states and the principles of quantum superposition and entanglement to allow greater computing efficiency than classical computers,[1] where the basic unit of information is the qubit, the quantum analogue to the classical binary bit. A theoretical quantum computing system must meet numerous requirements for physical implementation,[2] and finding systems appropriate for use as qubits is a popular innovation area. Photons, electrons, quantum dots, and other two-level quantum mechanical systems can serve as the physical basis for qubits.[3] Molecular-based qubit systems offer the exciting possibility for room-temperature operation, as opposed to the extremely cold temperatures required by other systems,[4] and provide the additional advantage of being highly tunable through structural modification. Quantum computing and the development of physical systems to act as qubits is a rapidly developing field. The prospect of room-temperature operation of quantum computers through the use of molecular qubits is an attractive goal; numerous recent publications have focused on this effort.[5] This chapter describes the synthesis and initial evaluation of heteroacenes with a desired crystal packing motif that is theorized to generate isolated triplet pairs, which may be suitable to serve as the basis for a qubit in future work.

4.2: Desired Crystal Packing for Isolated Triplet Pairs

Heteroacenes, as discussed in Chapters 2 and 3, are well-established as highly stable and tunable semiconductors, and many derivatives undergo singlet fission in both their bare and substituted forms. This chapter discusses silylethynyl thienoanthracenes functionalized with trialkylsilyl groups at the 2-position of the thiophene ring. The analogous thienotetracenes were also prepared by other researchers in our group and are briefly discussed in this chapter as a reference.

The compounds synthesized herein are evaluated for a specific crystal packing which is believed to be conducive to isolated triplet pair generation. The trialkylsilyl substitution at the 2-position of TAs forces a larger intermolecular distance than found in the unsubstituted analogue and is thought to induce a parallel alignment of the magnetic axes all the molecules in the crystal's unit cell. These features are necessary to generate

and maintain a high degree of spin polarization. Further, the end substitution should lead to an alignment of the energy levels between the triplet pair and the emissive singlet state, which permits the low temperature emission from the triplet pair. As will be shown in the following sections, careful tuning of the size of the 2-substituent as well as the silylethynyl group is necessary to reliably produce the desired effect.

One of the compounds that exhibits the desired packing is TiPS Thienotetracene 2-TES (TiPS TT 2-TES), prepared by Dr. Karl Thorley of UK and shown in Figure 4.1. As shown in Figure 4.1 (a), the TES-substituted thiophene ends force increased spacing between molecules (compared to the 2-H derivative), with an interplanar distance of approximately 5 Å between the two molecules shown. Figure 4.1 (b) and (c) show the relative positioning of these pairs relative to other pairs, with the desired overlap at the benzene end, and all of the π-surfaces parallel to each other, without any edge-to-face type interactions.
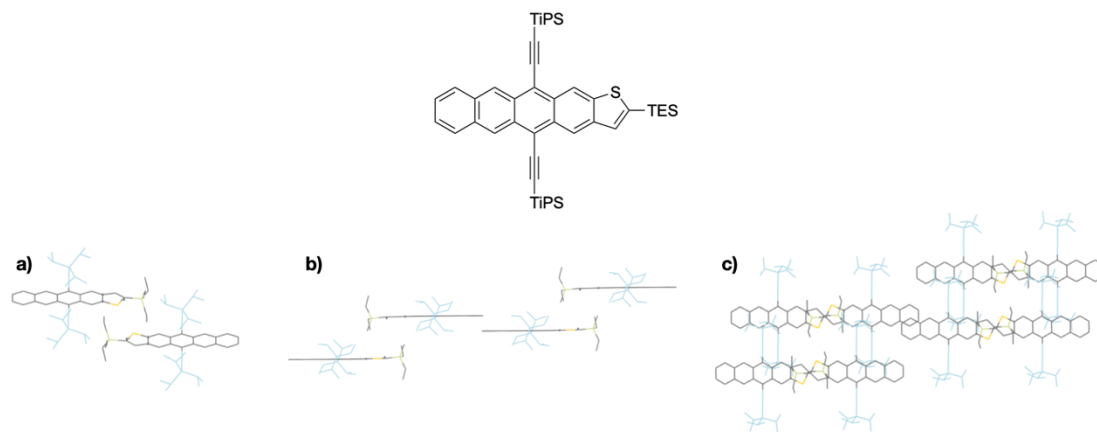
Figure 4.1: Structure and packing of TiPS TT 2-TES. (a) shows how the 2-substitution forces a larger intermolecular distance, (b) shows how the benzenoid ends show some π-overlap, and (c) shows the full packing motif.

The desired motif has pairs of molecules strongly coupled through the benzene ends, while isolated from other pairs by the increased spacing induced by the 2-position substituent. While TiPS TT 2-TES does show overlap of the benzenoid ends of the molecule with an interplanar distance of 3.504 Å, the goal of future work is to attain increased overlap of the benzenoid ends and stronger electronic coupling between the central pair, while maintaining isolation from other coupled pairs through the larger distances induced by the 2-position substituents.

The synthesis of the parent silylethynyl heteroacenes proceeded as described in Chapter 2 and is shown below in Figure 4.2. Further details on these steps can be found in the Experimental section.
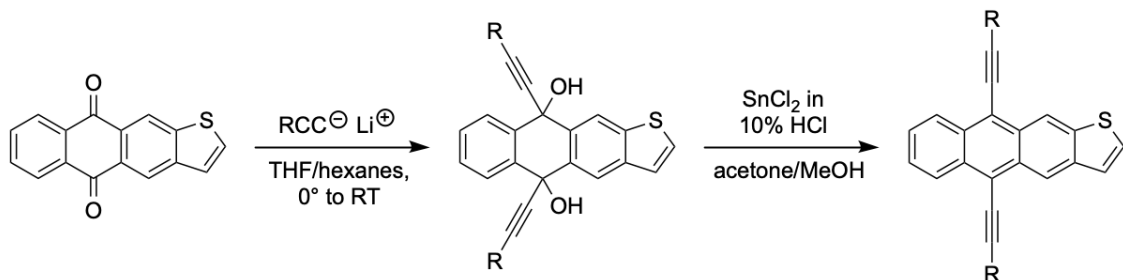
Figure 4.2: General Procedure A, the basic synthetic scheme to thienoanthracenes.

Functionalization at the 2-position followed the optimized protocols of Chapter 3 using LDA; fortunately, these conditions were even more effective to functionalize TAs with trialkylsilyl substituents.
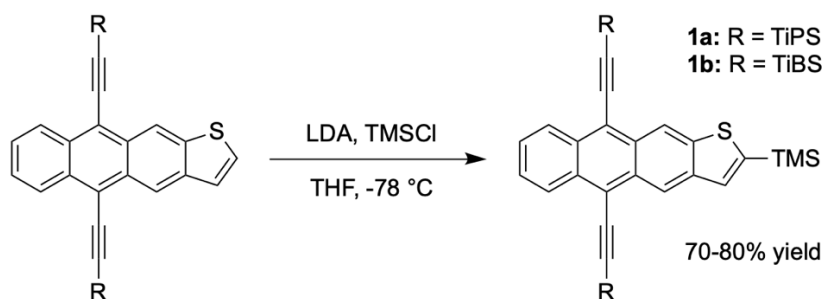
Figure 4.3: General procedure B, the synthetic scheme to 2-TMS functionalized compounds.

As shown in Figure 4.3, this procedure is typically high yielding. The reaction is typically complete in approximately two hours, and any unreacted starting material was easily recovered. The product molecules were obtained as yellow to orange crystals or flakes. The crystal structure of the TiPS derivative 1a was obtained readily, though the TiBS derivative 1b has not yet yielded crystals suitable for XRD, as it crystallized in fine flakes regardless of solvent that are too thin to be solved. The crystal packing of all derivatives will be discussed in section 4.5.

4.4: Functionalization of Other Chromophores

In order to contribute to a broader understanding of the packing and properties of 2-substituted heteroacenes, the trialkylsilyl substituted derivatives of other chromophores were also prepared, many of which were initially developed for other projects, as in Chapters 2 and 3. However, given the ease of synthesizing these starting materials, we determined it worthwhile to investigate them here as well.

The 2-TMS derivatives 2, 3, and 4 were prepared from TiPS FA, TES TA dioxolane, and 4F TES TA using the method of General Procedure B, as shown in Figure 4.4. Despite the lower yields of these derivatives, starting material was easily recovered with no decomposition for 2 and 3 and products were easily isolated. The reaction to produce compound 4 resulted in some decomposition in addition to product.
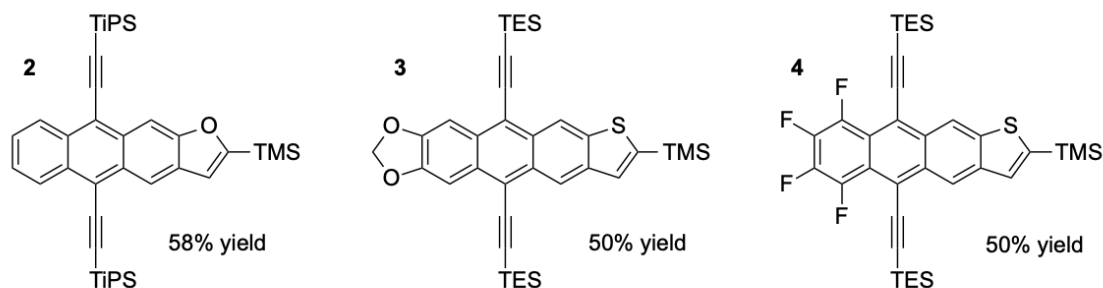
Figure 4.4: Structures and yields of derivatives 2, 3, and 4.

Compound 2 crystallized readily in large plates and a crystal structure was obtained. The packing of this derivative is described in the following section. Compounds 3 and 4 has not yet yielded crystals suitable for XRD, though efforts to grow such crystals are ongoing.

4.5: Analysis of Crystal Packing

The crystal packings of the prepared derivatives were closely analyzed in comparison to the representative compound, TiPS TT 2-TES. Thus far, only crystal structures of 1a and 2 have been obtained. The structure and packing of 1a are first evaluated and are shown below in Figure 4.5.
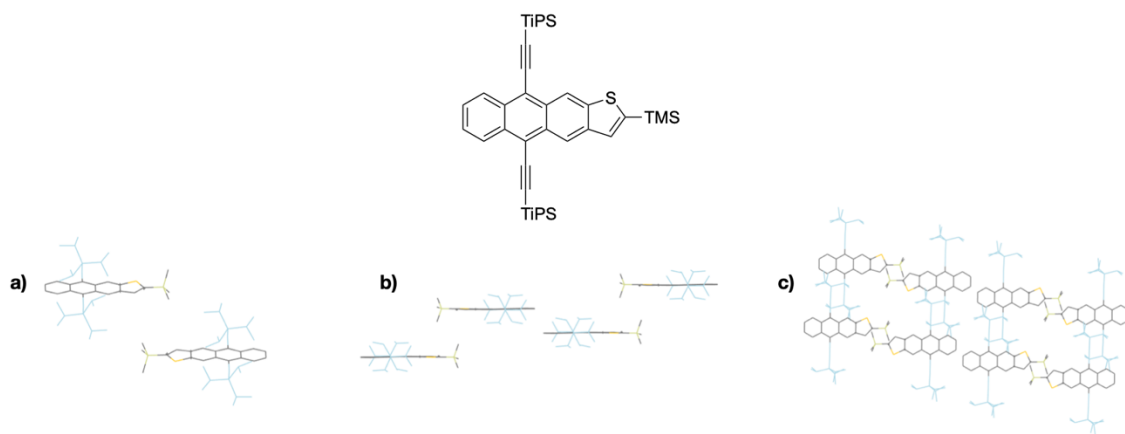
Figure 4.5: Structure and packing of TiPS TA 2-TMS. (a) shows how the 2-substitution forces a larger intermolecular distance, (b) shows the benzenoid ends where π-overlap is sought, and (c) shows the full packing motif.

As shown in Figure 4.5, 1a shows significant spacing between the thiophene ends, with the interplanar distance between the molecules in 4.5 (a) measured as 5.488 Å. Figure 4.5 (b) and (c), however, show that while there is not physical overlap of the π-surfaces at the benzenoid ends, there is a close interplanar distance of 3.232 Å and formal carbon-carbon close contacts.
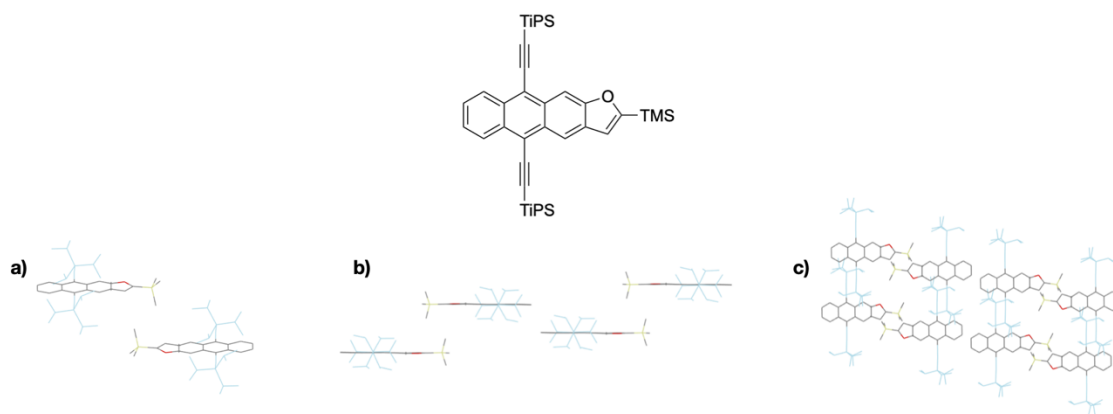
Figure 4.6: Structure and packing of TiPS FA 2-TMS. (a) shows how the 2-substitution forces a larger intermolecular distance, (b) shows the benzenoid ends where π-overlap is sought, and (c) shows the full packing motif.

TiPS FA 2-TMS, Compound 2, exhibits the desired increased spacing between the thiophene ends with an interplanar distance of 5.292 Å. The central pair of molecules in Figure 4.6 (b) are separated by 3.226 Å, which is quite close, but the physical overlap is not present, as can be seen in Figure 4.6 (b) and (c). However, in both Compounds 1a and 2, lack of physical overlap does not preclude strong electronic coupling, which will be explored further in section 4.7.

4.6: Photophysical Characterization

The absorbance spectra of the 2-TMS derivatives and their parent compounds are shown in Figure 4.7. As shown, the 2-TMS substituent induces a very small red-shift, approximately 5-10 nm in all derivatives.
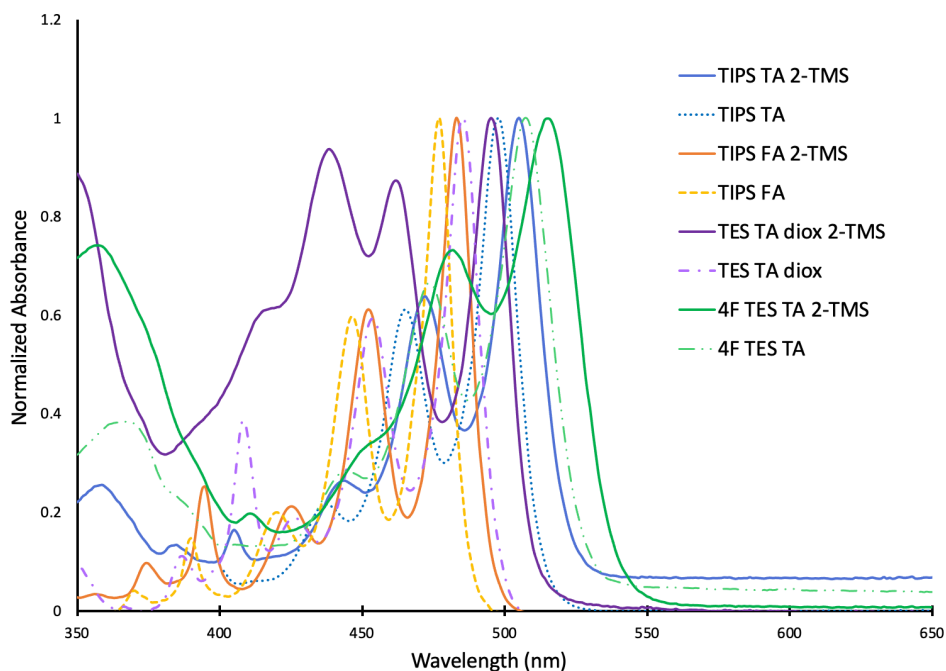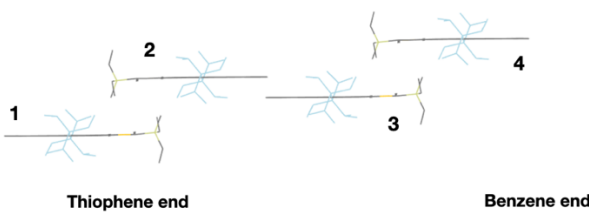
Figure 4.7: Absorbance spectra of the 2-TMS substituted heteroacenes and their parent molecules.

From the absorbance spectra, the singlet energies are estimated from the absorption edge to be approximately 2.33 eV for 1a (TiPS TA 2-TMS), 2.46 eV for 2 (TiPS FA 2-TMS), 2.38 eV for 3 (TES TA dioxolane 2-TMS), and 2.25 eV for 4 (4F TES TA 2-TMS).

4.7: Electronic Coupling of the Isolated Pair

Using DFT,[6] electronic coupling of each derivative was calculated. The couplings between HOMO-HOMO, HOMO-LUMO, and LUMO-LUMO were all computed and are shown in Figure 4.8 below. Since these molecules are being used in singlet fission applications, we are primarily interested in the HOMO-LUMO coupling. Further, the coupling is determined between the thiophene ends (denoted as molecules 1 and 2 or 3 and 4 in Figure 4.8) and the benzene ends (molecules 2 and 3).

| Compound | Thiophene end | | | Benzene end | | |
	HH	HL	LL	HH	HL	LL
TIPS TT 2-TES	0.4 meV	2.2 meV	3.2 meV	4.7 meV	41.4 meV	24.9 meV
TIPS TA 2-TMS	0.05 meV	0.009 meV	0.1 meV	6.1 meV	7.8 meV	5.1 meV
TIPS FA 2-TMS	1.2 meV	0.2 meV	1.4 meV	7.3 meV	38.5 meV	16.5 meV

Figure 4.8: Electronic coupling of select derivatives.

As shown in Figure 4.8, the electronic coupling between the thiophene ends, where increased spacing has been induced with the 2-substituent, is quite low. This suggests there is little communication between the molecules with this orientation, as predicted. However, the coupling at the benzene ends is higher. Particularly in TiPS TT 2-TES, the HL coupling is quite strong at 41.4 meV. While the electronic coupling is low in TiPS TA 2-TMS at the carbocyclic ends (between molecules 2 and 3, as depicted in Figure 4.8), it several orders of magnitude higher than at the thiophene end, and suggests that the desired molecules are in some degree of electronic communication, even if that coupling is not strong, and further suggests that the molecules overlapping at the thiophene end are quite isolated. The coupling calculations for TiPS FA 2-TMS show strong electronic coupling at the benzene end, similar to TiPS TT 2-TES, with minimal coupling at the thiophene end. Future derivatives will be synthesized with the goal of strengthening the electronic coupling between the benzene ends of the molecules while maintaining isolation from other pairs.

4.8: Conclusions

In conclusion, we present a simple synthetic route to trialkylsilyl substituted heteroacenes. Electronic coupling has been calculated for the isolated pairs, and future work will be focused on further increasing the electronic coupling between the carbocyclic ends of the molecules. The compounds that meet the desired packing requirements have

been shipped to collaborators at NREL for evaluation of triplet lifetimes and we expect that the results from these molecules will provide more insight into what structural modifications are most ideal to tune the crystal packing for the desired result. We can begin to utilize the structure-function relationships developed in Chapters 2 and 3 for heteroacenes to predict which derivatives will exhibit desired energy levels.

4.9: Experimental

Solvents were purchased in bulk from VWR, and other reagents were purchased from commercial sources (typically Sigma Aldrich) and were used as received. NMR spectra were measured on a 400 MHz Bruker instrument, and chemical shifts are reported in ppm and referenced to the deuterated solvents used. Absorbance was measured with an Agilent Cary 60 UV-vis spectrometer and fluorescence measured with StellarNet Inc. fluorimeter. Crystal structures were collected and refined by Dr. Sean Parkin of UK using a dual-microsource Bruker D8 Venture κ-axis diffractometer (MoKα & CuKα) with large-area 'Photon-II' CMOS detector.

General Procedure A: In a 0.1M solution of hexanes/THF (9:1-3:1 ratio) in a flame-dried flask under nitrogen, 3.5 equivalents of silyl acetylene were dissolved. The reaction solution was cooled to 0 °C and 3 equivalents of LiHMDS were added dropwise. The solution was allowed to stir for 30 minutes to 1 hour, after which the quinone starting material was added in one portion. The reaction solution was stirred overnight, and upon completion as determined by TLC, was quenched with deionized water and extracted with hexanes. The organic layers were dried with magnesium sulfate and concentrated by rotary evaporation. This diol intermediate was typically observed as a yellow or colorless oil and was used immediately without further purification. The diol was dissolved in minimal acetone and diluted with 0.1 M methanol open to air. To this, 6 equivalents of $SnCl_2$ dissolved in minimal 10% H_2SO_4 was added in one portion. The reaction solution was

allowed to stir for 1 hour and then was extracted with hexanes. The organic layers were dried with magnesium sulfate and concentrated via rotary evaporation. The resulting yellow, orange, or red solids were purified via chromatography with hexanes and recrystallized with acetone to give yellow or orange crystals.

General Procedure B: In a 0.1M solution of THF under nitrogen, the heteroacene starting material was dissolved. This solution was cooled to -78 °C, and 5 equivalents of 1M LDA were added dropwise. The reaction mixture was stirred for approximately 1 hour, and 3 equivalents of trimethylsilylchloride were added in one portion. The reaction mixture was stirred overnight and allowed to warm to room temperature. Upon completion, the reaction mixture was quenched with DI water and extracted with hexanes. The organic layers were dried with magnesium sulfate and concentrated via rotary evaporation. The product was purified on silica with hexanes and recrystallized with acetone to give yellow or orange crystals.
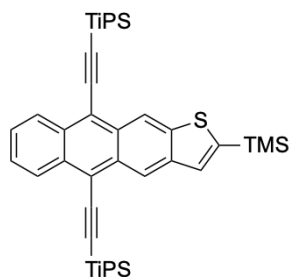
1a TIPS TA 2-TMS: Prepared via **General Procedure B**. 80% yield. ^{1}H NMR (400 MHz, C$_6$D$_6$): δ 9.660 (s, 1H), 9.521 (s, 1H), 8.980 (dd, J_{HH} = 9.90 Hz, 4.61 Hz, 2H), 7.593 (s, 1H), 7.350 (d, J_{HH} = 9.95 Hz, 2H), 1.320 (d, J_{HH} = 7.42 Hz, 42H), 0.247 (s, 9H). ^{13}C NMR (101 MHz, C$_6$D$_6$): δ 147.35, 143.70, 142.41, 133.09, 132.93, 130.93, 130.82, 130.78, 127.08, 126.93, 121.58, 120.08, 119.56, 118.37, 105.48, 105.38, 104.96, 104.81, 19.17, 19.14, 11.96, 11.93, 0.73. Structure confirmed by single crystal X-ray diffraction.
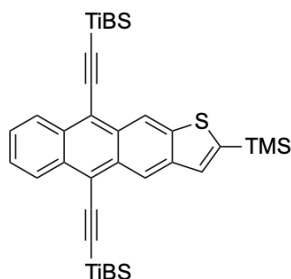
1b TIBS TA 2-TMS: Prepared via **General Procedure B**. 70% yield. ^{1}H NMR (400 MHz, C₆D₆): δ 9.646 (s, 1H), 9.506 9s, 1H), 8.961 (d, J_{HH} = 6.73 Hz, 2H), 7.600 (s, 1H), 7.357 (d, J_{HH} = 3.32 Hz, 2H), 2.206 (dd, J_{HH} = 13.28 Hz, 6.65 Hz, 6H), 1.221 (d, J_{HH} = 1.69 Hz, 18H), 1.205 (d, J_{HH} = 1.74 Hz, 18H), 0.967 (d, J_{HH} = 6.96 Hz, 6H), 0.925 (d, J_{HH} = 6.94 Hz, 6H), 0.261 (s, 9H). ^{13}C NMR (101 MHz, CDCl₃): δ 147.282, 142.900, 141.738, 132.487, 132.206, 130.569, 130.181, 130.086, 127.426, 127.387, 126.568, 126.409, 121.138, 119.589, 119.057, 117.743, 108.261, 107.966, 103.950, 103.886, 26.638, 26.622, 25.491, 25.486, -0.416.
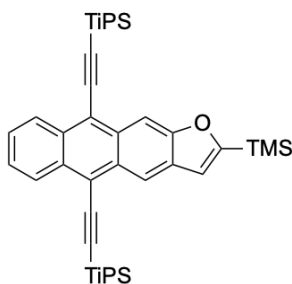
2 TIPS FA 2-TMS: Prepared via **General Procedure B**. 58% yield. ^{1}H NMR (400 MHz, C₆D₆): δ 9.295 (s, 1H), 9.177 (s, 1H), 8.999 (td, J_{HH} = 7.03 Hz, 3.07 Hz, 2H), 7.372 (d, J_{HH} = 9.96 Hz, 2H), 6.960 (s, 1H), 1.348 (d, J_{HH} = 4.62 Hz, 21H), 1.279 (d, J_{HH} = 5.49 Hz, 21H), 0.203 (s, 9H). ^{13}C NMR (101 MHz, C₆D₆): δ 168.92, 158.27, 132.95, 132.39, 132.15, 131.97, 130.65, 127.58, 127.47, 126.91, 126.63, 119.28, 118.93, 118.82, 116.52, 105.90, 105.30, 104.92, 104.87, 19.19, 19.15, 11.98, 11.89, -2.07. Structure confirmed by single crystal X-ray diffraction.
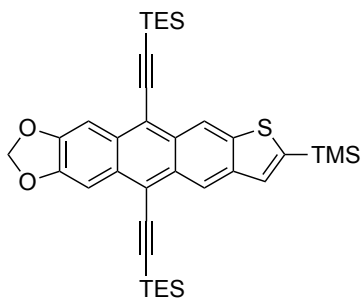
3 TES TA dioxolane 2-TMS: Prepared via **General Procedure B**. 50% yield. ^{1}H NMR (400 MHz, C_6D_6): δ resubmitted. MS calculated: 751.3802, found: 751.235.
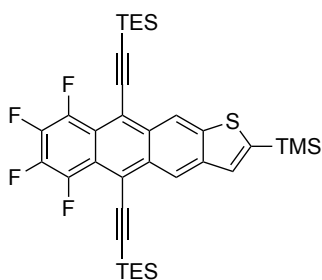
4 4F TES TA 2-TMS: Prepared via **General Procedure B**. x yield. ^{1}H NMR (400 MHz, C_6D_6): δ 9.735 (s, 1H), 9.613 (s, 1H), 7.660 (s, 1H), 1.364 (broad s, 12H), 1.262 (td, J_{HH} = 7.90 Hz, 2.25 Hz, 18H), 0.390 (s, 9H).

Chapter 5: Synthesis and Properties of Octadehydro[12]annulenes

5.1: Motivation for Dehydroannulenes

As discussed in Chapter 1.7, antiaromatic compounds offer a unique synthetic challenge and opportunity for organic materials through potentially decreased HOMO-LUMO gaps, lowered LUMO levels that may permit air-stable device operation in n-type semiconductors, and the possibility to advantageously tune and exploit excited-state properties. However, as covered previously, antiaromatic compounds are typically quite unstable, and identifying molecules that offer sufficient stability is the first step towards investigating their applicability in practice. From there, we must apply similar principles as discussed in Chapter 2 to build up structure-function relationships in order to systematically evaluate the prospects of a given core molecule. One interesting class of fully and formally antiaromatic molecules are the octadehydro[12]annulenes, or 12-DHAs, depicted in Figure 5.1. While they are relatively simple in structure, they remain largely unexplored in recent literature, and to our knowledge only one crystal structure without aromatic endcaps has been reported thus far.[1] Their benzannulated counterparts, shown in Figure 5.1, have been much more commonly reported,[2] and evidence suggests that the electronics of benzene- or other aromatic-fused 12-DHAs are dominated by the aromatic endcaps, meaning that these dibenzooctadehydro[12]annulenes exhibit properties that differ significantly from the core dehydroannulene.[3],[4]

a. Previous works: dibenzooctadehydro[12]annulenes (12-BDHA)
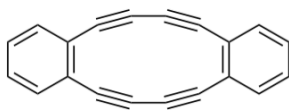
- Properties influenced by aromatic endcaps
- NICS = 22.32[a]

b. This work: octadehydro[12]annulenes (12-DHA)
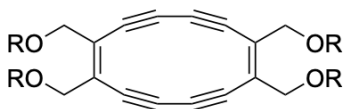
- Properties reflect antiaromatic core
- NICS = 57.36[b]

1a: R = MOM   **1d:** R = TIPS
1b: R = MOE   **1e:** R = TBDMS
1c: R = MOM   **1f:** R = TBDPS

Figure 5.1: Comparison of (a) previously reported derivatives with aromatic endcaps and (b) DHAs in this work without aromatic endcaps. [a]NICS values computed as described in the following sections. [b]NICS value shown for 1d. MOM = methoxymethyl, MOE = methoxyethyl, MOO = methoxyoctyl.

The general classification of "dehydroannulenes" encompasses numerous structures, including but not limited to those shown in Figure 5.2. The 12-membered cycle (octadehydro[12]annulene or 12-DHA) on the left in Figure 5.2 is of particular interest in this work, resulting from the copper-mediated dimerization of a *cis* ene-diyne. The larger dehydroannulenes shown in Figure 5.2 (trimers, tetramers, and higher-order oligomers) are also known and typically form in varying amounts from the same reaction conditions. The 12-membered antiaromatic dimer and 18-membered aromatic trimer (dodecadehydro[18]annulene or 18-DHA) are the most commonly observed and well-characterized of these macrocycles.
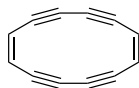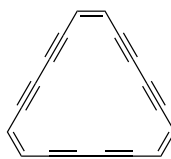
12-DHA dimer   18-DHA trimer   24-DHA tetramer
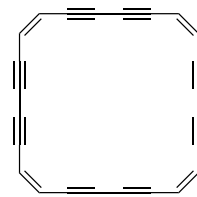
Figure 5.2: Dehydroannulene structures shown without aromatic or other substituents.

One of the most striking features of the 12-DHAs is the potential for an additional pathway for π-orbital interaction between adjacent molecules in the solid state. In addition to the face-to-face and edge-to-face packing motifs commonly observed in other organic

crystals,[5] the lack of peripheral hydrogens in 12-DHAs would theoretically allow for an additional edge-to-edge interaction between adjacent molecules as shown in Figure 5.3. Calculations of the electronic coupling of different orientations indicate that while the edge-to-edge interactions are not as strong as face-to-face π-stacking, charge transport is still possible.[6] As it is well-established that strong π-interactions and multidimensionality in π-stacking are correlated with efficient charge transport,[7] this unique structural aspect points towards the potential utility of these molecules in transistor applications. The 12-DHAs offer a conjugated π-surface that is unobstructed by peripheral hydrogens, which may allow for exceptionally close π-surface overlap that could lead to highly efficient multidirectional charge transport.

a) Face-to-face **b) Edge-to-edge**
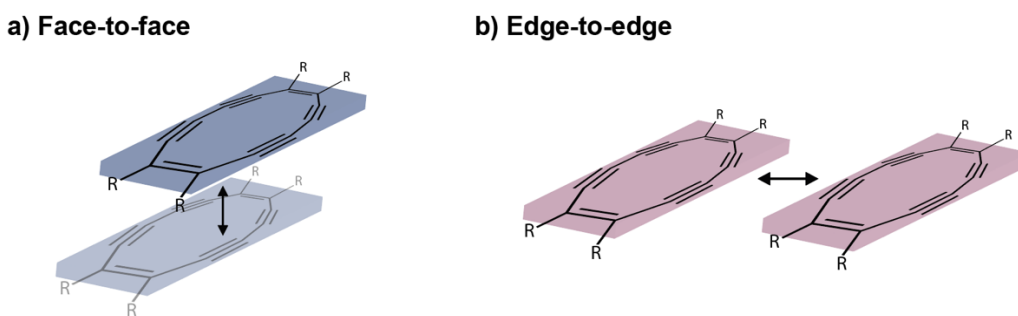
Figure 5.3: (a) Face-to-face interaction of the π-surfaces and (b) edge-to-edge interaction of the π-surfaces.

However, previous publications on this class of 12-DHAs reveal the suspected reason for their absence from extensive study: a number of the previously synthesized derivatives are quite unstable, some to the point of being unisolable.[3] This is not terribly surprising, given that these molecules are formally antiaromatic, and inherent instability is thus expected from antiaromatic molecules, as described in Chapter 1.7. The attempted synthesis of these derivatives has been reported,[3, 8] and it is suggested that the stability of future derivatives is highly dependent upon substituent effects.[1]

There are relatively few examples in the literature of 12-DHAs without aromatic endcaps; compared to other carbon cycles, this class of compounds has not been extensively studied. A 2006 review of annulene chemistry[9] summarizes the literature on 12- and 18-DHAs, and relatively few new studies have emerged in the more than a decade since. Given the absence of a wide range of DHAs from the current literature, it is believed that designing a series of derivatives, and conducting a thorough investigation of their

optical, photonic, and electronic properties, would be of interest of the organic materials community. The following sections briefly review previously published derivatives and then describe the synthesis and characterization of the derivatives prepared in this work.

5.2: Previous Work: Benzene-Fused Dehydroannulenes

The literature on dehydroannulenes can be separated into benzene-fused DHAs[10], here referred to as BDHAs, and non-benzene fused 12-DHAs, which will be referred to simply as DHAs. BDHAs dominate the majority of the literature on this class of compound, and while the characterization available is typically limited to basic optical, electronic, and computationally determined properties, there have been several BDHA derivatives published the last several decades.

Figure 5.4: Benzene-fused BDHA vs. bare DHA.

Synthetic strategies most commonly involve a Sonogashira coupling at an ortho-dihalide to produce an enediyne, followed by a copper-mediated coupling to produce the dehydroannulene as shown in Figure 5.5. It is worth noting that much of the relevant literature presents BDHAs as an intermediate to acenes or all-carbon frameworks through ring contraction-type reactions, which is one of the reasons for the relative lack of extensive characterization in the literature.[11]
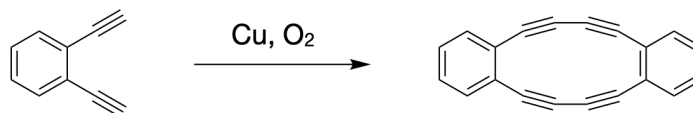
Figure 5.5: Most common synthetic strategy to BDHAs.

The parent BHDA molecule with no substituents was first synthesized in 1959 via a Glaser coupling, with basic optical and electronic properties reported.[12] The same synthetic strategy, shown in Figure 5.5, was employed for the other BDHA derivatives. The published compounds and their characterization, as available, are briefly summarized in Figure 5.6 and Table 5.1, respectively.
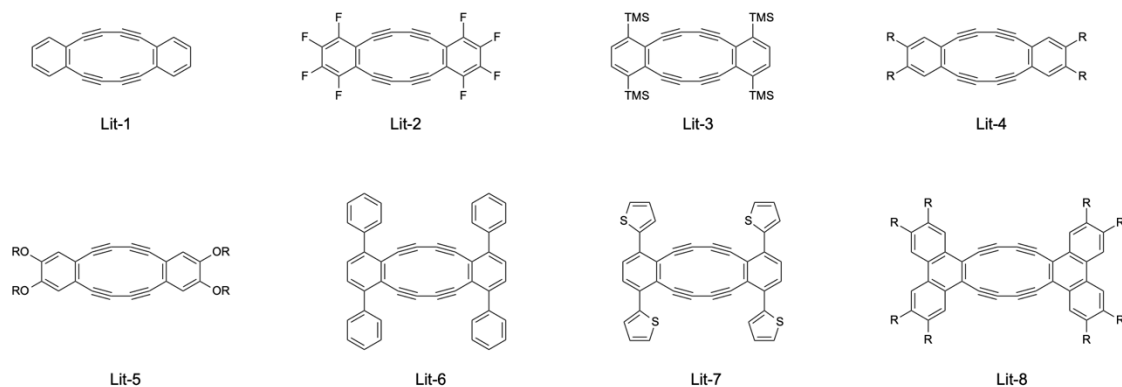
Figure 5.6: Previously published BDHAs.

As can be seen in Table 5.1, the characterization that is available for these compounds is not exhaustive. There are many gaps in the data reported, with only a few derivatives reporting NICS values, which is a measure of absolute magnetic shielding.

Table 5.1: Summary of properties of BDHAs Lit-1,[2] Lit-2,[2] Lit-3,[13] Lit-4,[14] Lit-5,[15] Lit-6,[16] Lit-7,[16] Lit-8.[17]

Compound	λ_{max} (nm)	E_{pc} (V vs. Fc/Fc+)	HOMO (eV)	LUMO (eV)	NICS	melting point (°C)
Lit-1	433	-2.00	-5.44	-2.33	N/A	N/A
Lit-2	435	-1.48	-6.15	-3.10	N/A	120 (decomposition)
Lit-3	447	N/A	N/A	N/A	N/A	N/A
Lit-4 (R = Hexyl)	305	N/A	N/A	N/A	N/A	113.5 (decomposition)
Lit-5 (R = Bu)	450	N/A	-5.08	-2.29	3.8	114 (decomposition)
Lit-6	260, 280, 330, 465	N/A	-5.32	-2.28	N/A	296 (decomposition)
Lit-7	250, 305, 240, 480	N/A	-5.43	-2.38	N/A	161 (decomposition)
Lit-8 (R = O(CH₂)₉CH₃)	274, 306, 347, 470, 559	-1.71	-5.20	-2.87	6.6	167

As noted above, literature compounds Lit-1-8 were frequently not the final product described, and so much of the characterization is limited to confirmation of structure, rather than a full examination of structure-function relationships. Of the information that is available, one can draw several conclusions. First, it should be noted that while the few NICS values provided are positive, indicating paratropicity and thus suggesting antiaromaticity, the values are relatively low, which suggests that the benzene endcaps have a significant influence on the degree of paratropicity. Second, it should be noted that

only literature compounds 6-8 reported a full UV-vis spectrum, with the remaining compounds only listing one max absorbance peak. As such, there are likely features present in those spectra that are simply not reported, and it cannot be assumed that they are absent. Finally, a majority of the literature compounds undergo thermal decomposition before melting, with the substituents having a strong effect on decomposition temperature.

5.3: Previous Work: Non-Aromatic Fused DHAs

There are very few reports of non-benzene fused DHAs. Only a handful of derivatives are known, and a number of those are highly unstable. As such, there is very little data on the relationship between derivatization and resulting optical or electronic properties of these compounds. The elucidation of structure-function relationship of these unique macrocycles is expected to be of great value towards the body of knowledge of antiaromatic small-molecule semiconductors.

The published non-benzene fused DHAs are primarily those synthesized by Anthony and Diederich[3] in the mid-1990s, including tetraethynyl DHAs and the silyl ether derivatives that were the foundation for this work.
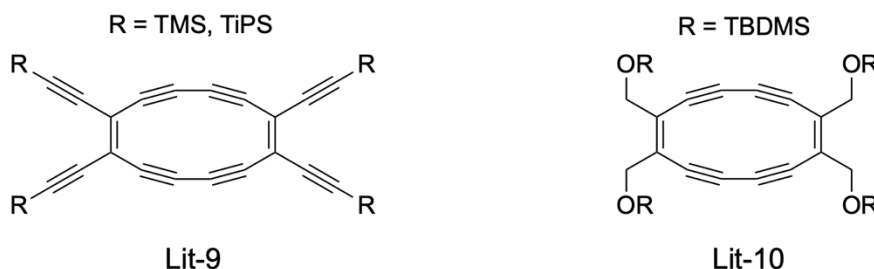
Figure 5.7: Previously synthesized DHAs Lit-9[18] and Lit-10,[3] without aromatic endcaps.

The tetraethynyl DHA Lit-9 was synthesized as the TMS and TiPS derivatives as shown in Figure 5.7. While NICS values are not reported and the absence of protons near the core prevents analysis of paratropicity by NMR, it is noted that there is a red-shift in the absorption edge of 12-DHA Lit-9 relative to the analogous 18-DHA trimer,[1] which is aromatic. This red-shift may be explained by the smaller HOMO-LUMO gap that is present in antiaromatic molecules,[19] suggesting that Lit-9 is indeed antiaromatic. Both Lit-9 derivatives show thermal decomposition prior to melting (~200 °C), main absorption peaks at approximately 340 and 350 nm (with many finer features present also), and reductions

at approximately -1.0 V versus Fc/Fc$^+$ as observed by cyclic voltammetry. Compound Lit-10 shows a characteristic double peak at approximately 280 and 305 nm with reported decomposition at 157 °C. No electrochemical data was reported for Lit-10.

More recently, several so far unpublished collaborations and projects have revealed other interesting prospects for DHAs. As 12 π-electron macrocycles, they are formally antiaromatic, as the derivatives known in the literature show evidence of paratropic ring currents.[3] One practical benefit of their antiaromaticity is the possibility for 2-electron reduction to the aromatic compound, which has been shown to be facile in other antiaromatic compounds.[20] With this potentially facile reduction comes the prospect for use in several device applications, namely as n-type semiconductors. An n-type material that is air-stable and easily reduced is of great interest to the field of organic semiconductors,[21] and some 12-DHAs may be suitable, given the results of preliminary electrochemical studies on select derivatives. The TiPS derivative of Compound Lit-9 exhibited a reversible first reduction at -0.99 V versus Fc/Fc$^+$,[18] which implies a LUMO energy of -4.11 eV. This suggests that the TiPS ethynyl DHA falls within the range for air-stable device operation.[22]

Finally, previous unpublished studies between the Anthony group and collaborators have shown that the singlet energy of DHAs is roughly double that of the triplet; as discussed in Chapter 1.5, this may indicate that the material can undergo efficient singlet fission. This is a largely unexplored but potentially useful facet of these compounds that will hopefully undergo further study once a series of stable derivatives has been identified.

5.4: Current Work: Initial Synthetic Strategy

The DHA core is based upon an enediyne substructure; as such, generation of this enediyne is the primary synthetic target. Precedence from previous researchers called for the use of commercially available mucobromic acid to get to the enediyne diol, shown below in Figure 5.8. While this enediyne is known in the literature,[23] optimization of the conditions was required.
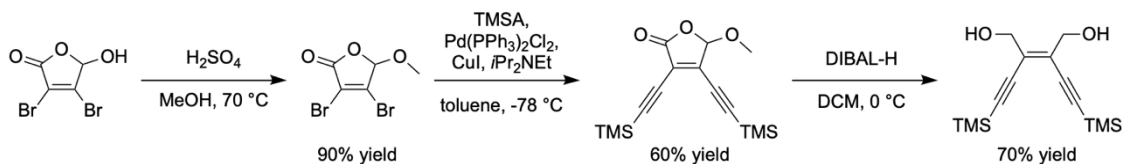
Figure 5.8: Synthetic scheme from mucobromic acid to enediyne diol. TMSA = TMS acetylene. DIBAL-H = di(*iso*-butyl) aluminum hydride.

During optimization of the Sonogashira step to increase the initially poor yield, it was determined that cooling and sealing the reaction to avoid evaporation of volatile TMS acetylene before the reaction was complete improved the yields somewhat. However, further optimizations were investigated, as the isolation of product remained quite challenging. After trying multiple catalyst and ligand combinations, it was found that lower catalyst loading results in fewer side products, simplifying the workup and allowing a greater yield of product to be more easily isolated. While yields remain around 60% for this step, the reaction is easily carried out on a 5g scale, and this enediyne is used immediately after isolation. The DIBAL reduction step was not without challenge either; initial conditions called for a significant excess of DIBAL to see completion of the reaction. This, however, was found to result in an interesting side product wherein one of ethynyl "legs" of the structure was also reduced to the alkene, shown in Figure 5.9. Not only was this side product inseparable from the desired enediyne by chromatography, but they appear to also cocrystallize and result in the disordered structure shown. This obviously prevents the formation of the desired macrocycle should any of this side product remain during the following reaction steps. Reducing the amount of DIBAL used, along with switching to commercially available DIBAL in dichloromethane as opposed to DIBAL in hexanes (which significantly improved the solubility of the resulting product and allowed a more concentrated overall reaction) resolved this issue, and the over-reduced diol was not observed following this change.
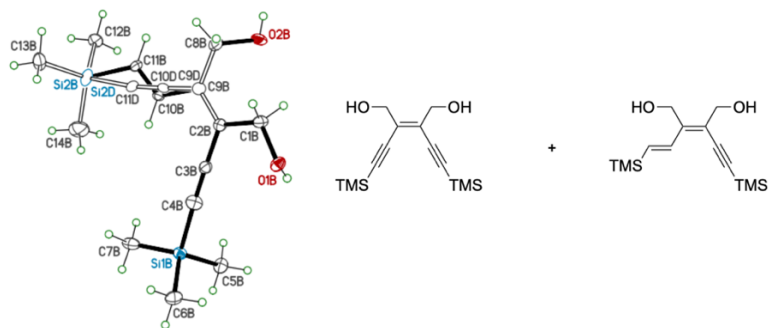
Figure 5.9: Intended and over-reduced enediyne diol.

Once the enediyne diol was obtained, the simple and established conditions shown below in Figure 5.10 were needed to obtain the alkyl ether or silyl ether derivatives 1a-f. A deprotection of the TMS group with classic conditions provided the delicate bare alkyne, which was used immediately without purification.
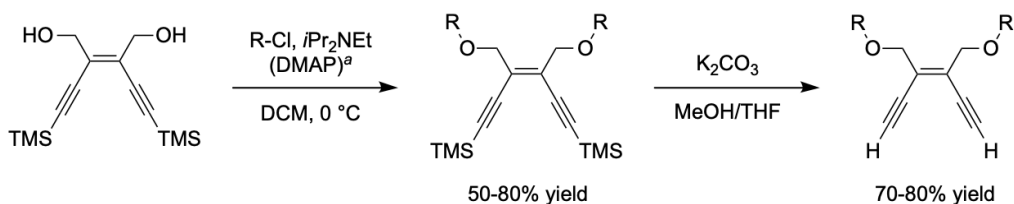
Figure 5.10: Synthetic scheme from enediyne diol to deprotected enediyne. [a]DMAP was employed for 1c-f.

The final step in the synthetic scheme is the Hay coupling, which initially employed the commonly used copper (I) chloride, which gave only modest yields at best, with many reactions failing entirely. Literature precedent suggested that copper (I) iodide offered improved yields for Hay couplings on other substrates,[24] and these conditions were utilized here as shown in Figure 5.11. An improvement in yield from approximately 30-40% with copper (I) chloride to up to 70% with copper (I) iodide was immediately noted. The authors of Ref. 24 suggest that employing 2,2-bipyridyl ligands also resulted in improved yields; this was investigated for 1a (MOM), and 2,2-bipyridyl was found to be an equivalent substitute for TMEDA, with neither an increase nor decrease in yield.
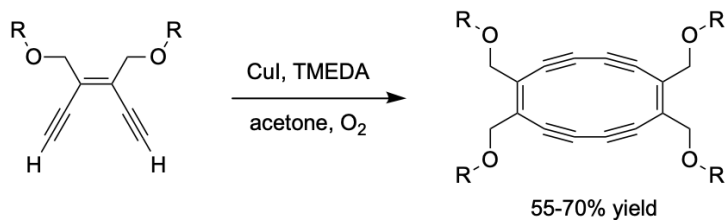
Figure 5.11: Hay coupling with deprotected enediyne.

In total, six DHAs were synthesized using the optimized conditions described in the previous section. Crystal structures were obtained for four of these: 1a (MOM), 1d (TiPS), 1e (TBDMS) and 1f (TBDPS). 1b and 1c (MOE and MOO, respectively) crystallize as extremely fine needles that have thus far proven unsuitable for XRD. The structures of all derivatives are shown below in Figure 5.12.
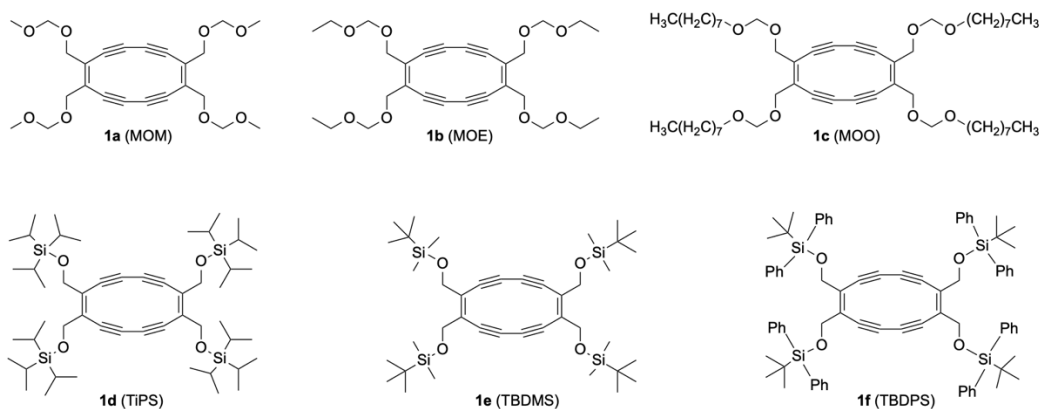
Figure 5.12: Synthesized DHAs 1a-f.

5.5: Crystal Structures and Electronic Coupling of DHAs

The crystal structures of derivatives 1a, 1d, 1e, and 1f were obtained and their bond lengths and packing motifs analyzed. Figure 5.13 shows the bond lengths and overall molecule length of each of these derivatives as obtained from their crystal structures.

Figure 5.13: Bond lengths and molecule lengths of each derivative compared to BDHA.
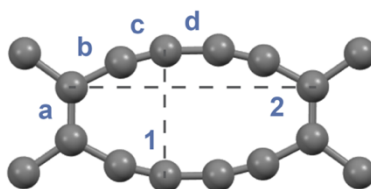
Compound	Bond Length a (Å)	Bond Length b (Å)	Bond Length c (Å)	Bond Length d (Å)	Molecule Length 1 (Å)	Molecule Length 2 (Å)
MOM	1.361	1.438	1.205	1.376	3.251	6.267
TiPS	1.360	1.431	1.208	1.376	3.291	6.247
TBDMS	1.364	1.437	1.203	1.377	3.255	6.271
TBDPS	1.360	1.434	1.207	1.373	3.305	6.243
dibenzo-DHA	1.414	1.423	1.206	1.372	3.254	6.264

The DHA chromophore is approximately 3.2 Å along the y axis and 6.2 Å along the x axis (denoted as Molecule Length 1 and 2, respectively), with slight variation between derivatives and a high degree of symmetry within individual molecules. Significant bond localization between the single, double, and triple bond lengths are observed, though there is largely consistently between these different bond lengths in each derivative. Bond localization has been observed as a way to avoid the true conjugation and destabilizing effects of antiaromaticity.[25] Bond length a is quite different between the aromatic-fused and non-aromatic-fused derivatives; in the parent BDHA, bond length a is part of the fused benzene ring and is thus delocalized.

The crystal structures show some measure of 1D π-stacking in all derivatives. Figure 5.14 shows the packing of 1a, 1d, 1e, and 1f, though it should be noted that 1f contains solvent (acetone). While there do not appear to be close edge-to-edge interactions between adjacent cores for these derivatives, 1a and 1d in particular show good face-to-face overlap.
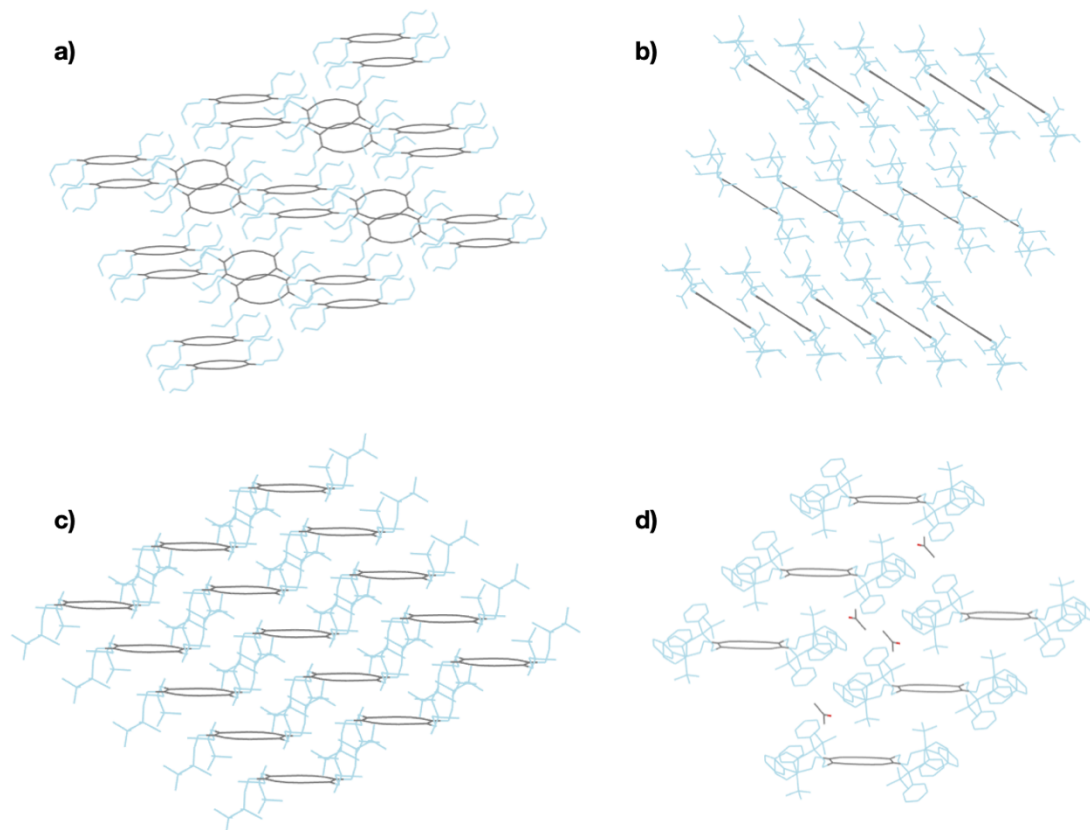
Figure 5.14: Packing motifs of 1a (a), 1d (b), 1e (c), and 1f (d).

The packing motifs show strong π-surface overlap for 1a, 1d, and 1e. In 1a, the adjacent stacks are rotated approximately 90° from each other, but in 1d and 1e, the cores are all planar throughout the motif. Between the incorporated solvent and bulky silyl groups of 1f, it is not surprising that there is no π-surface overlap in this derivative. The interplanar distances between the π-surfaces were found to be 3.447 Å for 1a, 3.470 Å for 1d, 3.567 Å for 1e, and 8.018 Å for 1f. There are carbon-carbon close contacts between the DHA cores for 1a, 1d, and 1e, as determined using the sum of the van der Waals radii plus 0.2 Å as described in previous chapters.

Electronic couplings for the derivatives that yielded a crystal structure were computed by Dr. Karl Thorley of UK using density functional theory (B3LYP/6-31G*). The HOMO-HOMO, HOMO-LUMO, and LUMO-LUMO couplings are shown in Table 5.2. The LUMO-HOMO couplings were also calculated but were identical to the HOMO-LUMO, and thus they are not shown.

Table 5.2: Electronic couplings of dehydroannulenes.

Compound	HOMO-HOMO	HOMO-LUMO	LUMO-LUMO
1a (MOM)	134.9 meV	22.6 meV	4.49 meV
1d (TIPS)	11.5 meV	81.3 meV	12.3 meV
1e (TBDMS)	50.8 meV	52.2 meV	32.9 meV
1f (TBDPS)	2.2 meV	2.9 meV	3.1 meV

Derivatives 1a, 1d, and 1e show strong electronic coupling. In particular, the HOMO-HOMO coupling of 1a and HOMO-LUMO coupling of 1d are quite large, and all of the coupling values for 1e are significant. The HH and LL electronic coupling in TiPS Pentacene have been calculated as 23 meV and 90 meV,[26] respectively, for context. The coupling values for 1f are quite low, though this is expected due to the incorporation of solvent in the crystal structure, which is likely interfering with any electronic communication between molecules that may be present. Further, the extremely bulky TBDPS groups make it unlikely to exhibit any strong π-surface overlap. Unfortunately, the LUMO-LUMO couplings for most derivatives are lower than would be expected for a high-performing n-type semiconducting material, though 1e shows some promise.

5.6: Optical, Photophysical, and Electrochemical Characterization of DHAs

The optical characterization of these dehydroannulenes showed a characteristic double peak at approximately 280 and 305 nm, with few features at longer wavelengths, as shown in Figure 5.15. The main absorption bands were characterized as a mixture of π- π* transitions by time dependent density functional theory (TD-DFT, ωB97XD/6-31G*), originating most notably from transitions from lower energy orbitals to the lowest unoccupied orbital. The TD-DFT analysis revealed a number of disallowed or very weakly allowed transitions at longer wavelengths, which correspond with the experimental peaks around 350 nm, as well as a potential extremely broad signal between 400 and 600 nm. The HOMO-LUMO transition is also predicted to be forbidden, occurring at 690 nm and

not observable by UV-vis spectroscopy. Experimental features above 500 nm are not observed. None of the derivatives exhibit fluorescence.
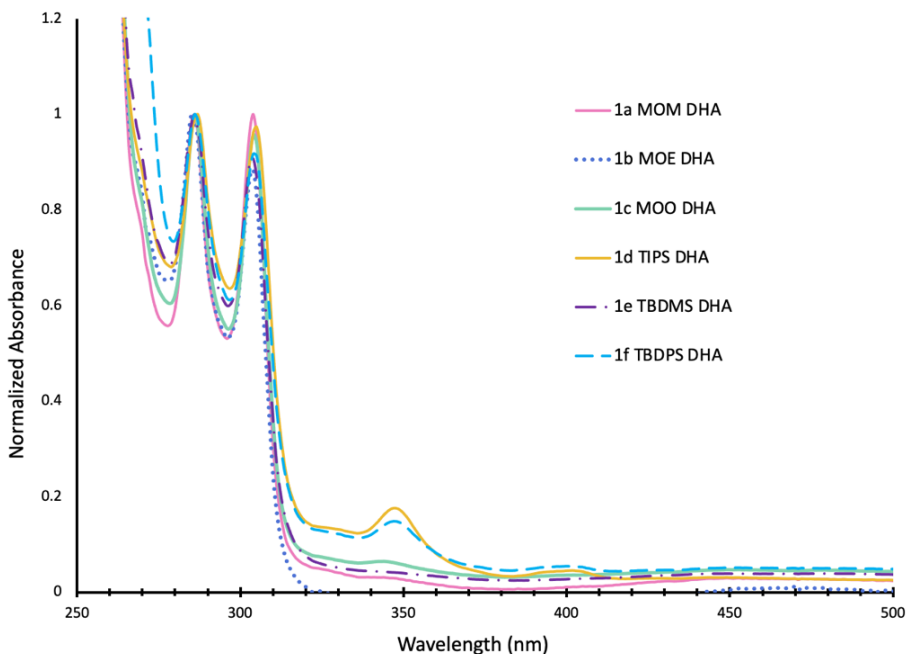
Figure 5.15: Absorbance spectra of dehydroannulenes, taken in 1,2-dichloroethane at RT, 10 μM.

Solution-state stability studies of derivatives 1a-f showed no degradation of the absorption spectrum over a period of 30 minutes as shown below in Figure 5.16. While the derivatives are quite robust in solution, exhibiting no decomposition over 30 minutes of exposure to a broad spectrum light source, it was noted that 1a in particular was not stable to prolonged storage at room temperature while in the solid state. This derivative went from fine pink needles to curled black fibers over approximately two weeks if not kept in a sealed, dark container at 0 °C. The other derivatives were stored similarly as a precaution, but decomposition was not observed over a period of several months.
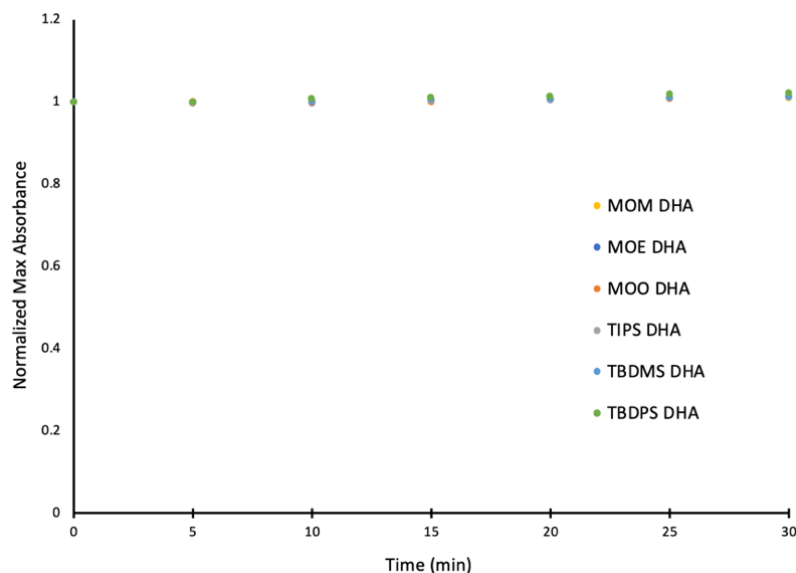
Figure 5.16: Stability of DHAs. Spectra were measured by UV-vis in 1,2-dichloroethane at RT and approximately 10 μM.

Electrochemical characterization of 1a-f was conducted using a combination of cyclic voltammetry (CV) and differential pulse voltammetry (DPV). The former shows the reduction peaks themselves, while the latter is essentially the first derivative of the CV spectrum and allows the reduction events to be easily evaluated.
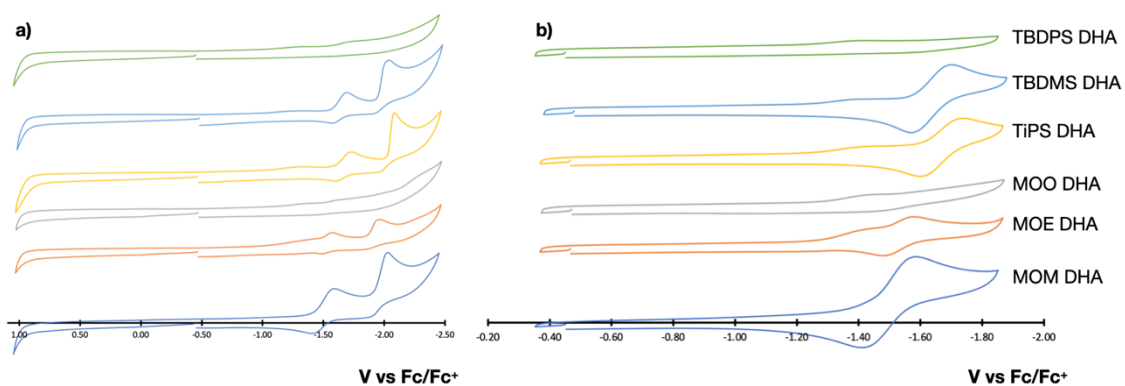
Figure 5.17: (a) Full CV spectra showing both reductions and (b) isolated first reductions of DHAs.

Electrochemical characterization of 1a-f showed at least one clear reduction for each derivative, typically two sequential reductions. Oxidations were not observed in any derivatives. In all except 1c (MOO) and 1f (TBDPS), the first reduction appears to be perfectly reversible, as shown in Figure 5.17. In 1f, a clear second reduction was not observed, though it is suspected this is due to the lack of electrochemical stability rather than a true absence of this feature. The isolated first reductions for all are shown in Figure

5.17. Interestingly, both 1c and 1f appears to break down rapidly during electrochemical experiments, despite being stable in the same solvents during other studies. The reduction values are summarized in Table 5.3. As shown, the silyl derivatives 1d-f show slightly more negative reduction values than alkyl ether 1a-c, implying that 1d-f are less easily reduced than 1a-c. The reduction values (taken from the DPV spectra) and other properties of the DHAs are summarized below in Table 5.3.

Table 5.3: Characterization of DHAs. Melting/decomposition points from DSC.

Compound	λ_{max} (nm)	E_{red} 1 (V vs. Fc/Fc+)	E_{red} 2 (V vs. Fc/Fc+)	melting point (°C)
1a (MOM)	304	-1.48	-1.95	87.37
1b (MOE)	304	-1.51	-1.87	73.05
1c (MOO)	304	-1.53	-1.97	47.39
1d (TIPS)	305	-1.65	-1.99	178.61 (decomposition)
1e (TBDMS)	304	-1.62	-1.95	166.57 (decomposition)
1f (TBDPS)	304	-1.61	N/A	146.09 (decomposition)

Melting points of derivatives 1a-f were measured using differential scanning calorimetry and recorded in Table 5.3. The ether derivatives 1a-c exhibit low melting points, with 1c (MOO) melting at only 47.39 °C. These derivatives decompose with continued heating, with an irreversible exothermic transition occurring at 93.68 °C (1a), 100 °C (1b), and 108.95 (1c). The silyl ether derivatives 1d-f decompose before melting as shown in Table 5.3.

5.7: Investigation of Antiaromaticity in DHAs

In order to attempt to demonstrate true antiaromaticity in these DHAs, several studies were conducted. First, we sought evidence of paratropic ring currents by comparing the NMR spectra of representative DHA 1b (chosen over other derivatives for its stability and solubility) with its non-aromatic TMS-protected diyne starting material. As discussed in Chapter 1.7 and in previous sections, paratropicity manifests as an upfield shift in the NMR spectrum. In the case of 1b, a clear upfield shift is observed from the diyne to the

DHA. As shown in Figure 5.18, the chemical shift for each of the protons in 1b is shifted upfield relative to those in the TMS diyne starting material. While the lack of hydrogen atoms fused to the core of the molecule is advantageous for application, as previously discussed, it was initially suspected that this may cause robust evidence of paratropicity to be absent from the NMR spectra; gratifyingly, the data in Table 3 lends experimental support to the suspected presence of paratropic ring currents in the DHA core, and suggests that this paratropicity exerts an effect on the substituent protons, particularly those in closest proximity to the core.

a) Substructure of MOE	NMR Data	
	Signal	Chemical Shift in 3b MOE diyne (ppm)	Chemical Shift in 1b MOE DHA (ppm)
	H_a	4.24	3.36
	H_b	4.52	4.31
	H_c	3.43	3.32
	H_d	1.07	1.05
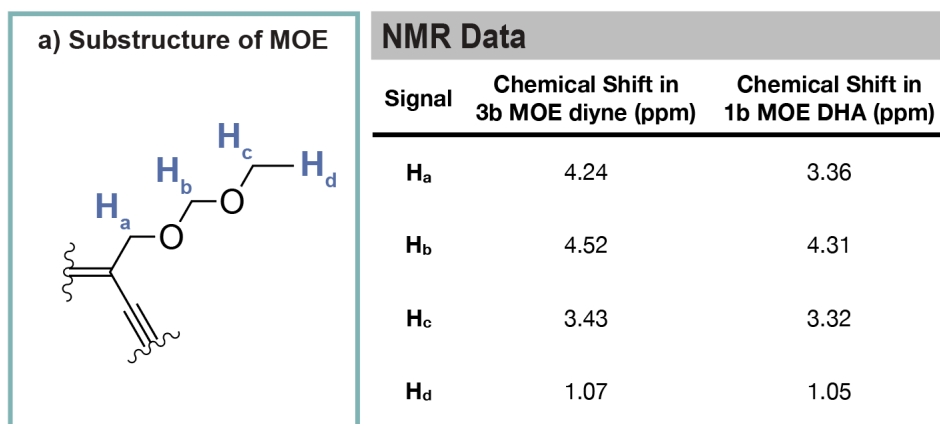
Figure 5.18: Comparison for NMR of MOE TMS diyne and 1b (MOE DHA) demonstrating upfield shift upon cyclization. NMRs were taken in d_6-benzene.

As discussed previously, nucleus-independent chemical shift is a valuable tool in assessing antiaromatic character through the quantification of magnetic shielding. The NICS values were computationally determined for the bare 12-DHA along with the representative compounds 1a and 1d, as well as the unfunctionalized 12-BDHA for a comparison of the degree of antiaromatic character in molecules with and without aromatic endcaps. These results are shown in Figure 5.19, calculated using B3LYP/6-31G* as adopted elsewhere in the literature.[27]
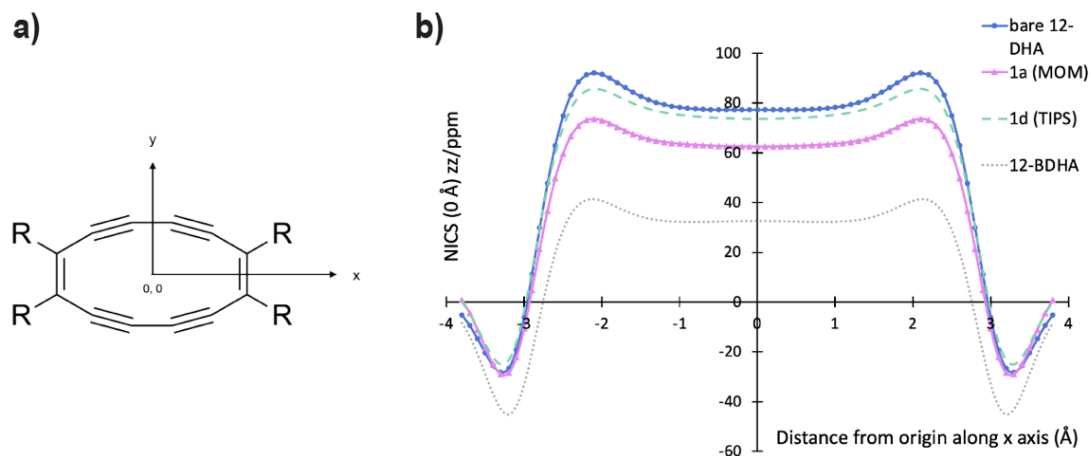
Figure 5.19: (a) x and y directions along the DHA core. (b) NICS-X scan values as calculated at y = 0 Å, z = 0 Å.

NICS-X scans[28] were performed along the x axis at y = 0 Å, at three different distances from the DHA plane (z = 0 Å, 1 Å, and 1.5 Å), with the z = 0 Å plot shown in Figure 5.19 (b), demonstrating the large paratropic ring currents across the dehydroannulene core. Unsurprisingly, the unsubstituted bare 12-DHA exhibits the most positive NICS values, which suggests the greatest degree of antiaromatic character, as it does not contain any influence from substituents. The TIPS derivative 1d shows NICS values quite similar to the bare DHA, while 1a (MOM) shows a slight reduction in NICS values compared to the unsubstituted core. As shown in Figure 5.13 above, all of the derivatives for which a crystal structure was obtained exhibit a molecule length of approximately 6.2 Å along the x axis, which correlates well with the data in Figure 5.19 (b), showing positive NICS values extending 3 Å from the origin in both directions along the x axis. While 12-BDHA shows positive NICS values, which suggests paratropicity exists in this compound as well, the aromatic endcaps show a clear influence on the NICS values, implying a reduction in paratropicity and antiaromatic character compared to the "pure" dehydroannulene. The NICS values are summarized in Table 5.4, showing the dramatic difference in NICS values in molecules with and without fused aromatic endcaps.

Table 5.4: NICS values calculated at the DHA center using B3LYP/6-31G*.

Compound	NICSzz(0)	NICSzz(1)	NICSzz(1.5)
bare 12-DHA	77.30	60.39	44.39
1a (MOM)	62.49	47.61	34.19
1d (TIPS)	73.6	57.36	42.10
12-BDHA	32.59	22.32	14.45

This is further demonstrated in the contour plots shown in Figure 5.20, representing the NICS values as they change across the x and y axes of the dehydroannulene core (NICS-XY scan). Not only is it apparent that the unsubstituted 12-DHA exhibits much more strongly positive NICS values, but Figure 5.20 also shows that the paratropic ring currents present in the dehydroannulene core extend slightly further beyond the core itself in the bare derivative but are strictly contained within the central ring in the aromatic endcapped analogue.
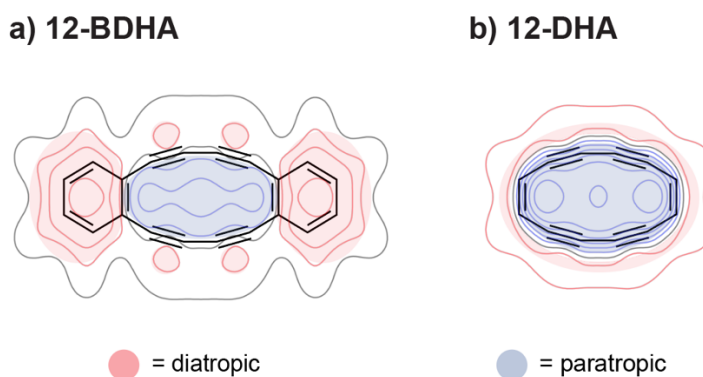
Figure 5.20: Contour plots showing the paratropicity and diatropicity of (a) unsubstituted BDHA and (b) bare DHA.

All of the data obtained suggest that the dehydroannulenes 1a-f are indeed formally antiaromatic and free of influence of aromatic endcaps, which is shown in the literature to mask the properties of the antiaromatic core. The calculated NICS values and experimental evidence of paratropicity from the NMR spectrum are particularly indicative of

antiaromaticity, though the bond length alternation identified in the crystal structures suggests that these molecules are likely stabilized by the lack of true bond delocalization.

5.8: Conclusions

In conclusion, we present an optimized synthetic route to octadehydro[12]annulenes and report six derivatives, all of which exhibit surprising stability compared to previous octadehydro[12]annulenes. Thorough optical and electrochemical characterization is provided, and strong electronic coupling is observed in several derivatives. We demonstrate the antiaromaticity of these molecules, supported by both computational and experimental data, and begin to develop structure-function relationships that will inform the design of future derivatives.

5.9: Experimental

Solvents were purchased in bulk from VWR, and other reagents were purchased from commercial sources (typically Sigma Aldrich) and were used as received. NMR spectra were measured on a 400 MHz Bruker instrument, and chemical shifts are reported in ppm and referenced to the deuterated solvents used. Melting or decomposition points were determined using a TA Instruments DSC Q100. Absorbance was measured with an Agilent Cary 60 UV-vis spectrometer and fluorescence measured with StellarNet Inc. fluorimeter. Crystal structures were collected and refined by Dr. Sean Parkin of UK using a dual-microsource Bruker D8 Venture κ-axis diffractometer (MoKα & CuKα) with large-area 'Photon-II' CMOS detector.
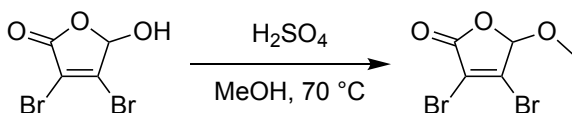
Methylation of mucobromic acid: Mucobromic acid (25 g) was dissolved in 200 mL methanol open to air. Approximately 5 mL of concentrated sulfuric acid was added slowly. The reaction mixture was refluxed overnight. Upon completion, the reaction was quenched with aqueous NaHCO₃ and extracted with ether. The organic layers were dried with magnesium sulfate and concentrated via rotary evaporation. The methylated product was

purified on silica with DCM, recrystallized with hexanes, isolated as a white solid, and confirmed by GCMS. 90% yield.
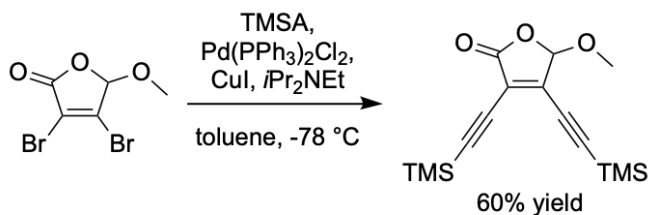
Sonogashira at ortho-dibromide: The methylated dibromo ester (5g) from the previous step was dissolved in 0.2 M toluene and 3 equivalents of iPr$_2$NEt. The reaction mixture was cooled to -78 °C, and 5 mol% Pd(PPh$_3$)$_2$Cl$_2$ and equivalent weight CuI were added in one portion and allowed to dissolve. TMS acetylene (3 equivalents) was added slowly, and the reaction vessel was sealed. The reaction mixture was stirred overnight and allowed to slowly warm to room temperature. Upon reaction completion by TLC and GC, the reaction mixture was diluted with hexanes and cooled to 0 °C. The reaction mixture was then poured over Celite and eluted with hexanes, followed by purification on silica with hexanes and ethyl acetate. The product was confirmed by GCMS, isolated as a yellow oil, and used immediately to avoid decomposition.
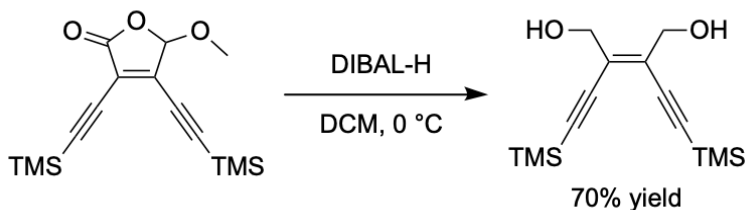
Reduction to diol: The enediyne from the previous step was dissolved in 0.1 M DCM under nitrogen and cooled to 0 °C. To this, 3.5 equivalents of DIBAL-H in DCM (1 M) were added dropwise. The reaction mixture was stirred between 6 hours-overnight. Upon completion of the reaction by TLC, approximately 10 mL of deionized water was added slowly and the reaction mixture was allowed to gel. The reaction mixture was filtered and washed with DCM and ether, leaving behind the aluminum salts. The filtrate was dried with magnesium sulfate, concentrated via rotary evaporation, and purified with hexanes and ethyl acetate. The resulting white solid was recrystallized with hexanes to give a fine

white crystalline solid. ^{1}H NMR (400 MHz, CDCl$_3$): δ 4.243 (s, 4H), 0.200 (s, 18H). Structure confirmed by single crystal X-ray diffraction.

50-80% yield
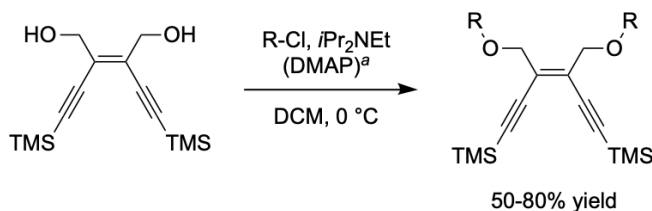
Ether functionalization: The enediyne diol (1g) was dissolved in 0.1 M DCM under nitrogen. The reaction mixture was cooled to 0 °C and 3 equivalents of iPr$_2$NEt were added slowly. The reaction mixture was stirred for approximately 30 minutes. At this point for derivatives 1c-f, approximately 15 mg of DMAP were added in one portion. For all derivatives, 2.5-4 equivalents of the corresponding silyl- or alkoxy-chloride were added slowly. The reaction mixture was allowed to stir and warm to room temperature over approximately 2 hours. Upon completion by TLC, the reaction mixture was quenched with deionized water and extracted with hexanes. The organic layers were dried with magnesium sulfate, concentrated via rotary evaporation, and purified with hexanes and ethyl acetate. The resulting products were confirmed by GCMS and isolated as colorless oils. MOE: ^{1}H NMR (400 MHz, CD$_2$Cl$_2$): δ 4.648 (s, 4H), 4.184 (s, 4H), 3.585 (q, J$_{HH}$ = 7.08 Hz, 4H), 1.190 (t, J$_{HH}$ = 7.07 Hz, 6H), 0.210 (s, 18H). MOO: ^{1}H NMR (400 MHz, CD$_2$Cl$_2$): δ 4.622 (s, 4H), 4.346 (s, 4H), 3.537 (t, J$_{HH}$ = 6.60 Hz, 3H), 3.489 (t, J$_{HH}$ = 6.55 Hz, 3H), 1.586 (m, 8H), 1.363 (broad s, 6H), 0.896 (tt, J$_{HH}$ = 6.94 Hz, 3.56 Hz, 14H), 0.263 (s, 18H).

70-80% yield
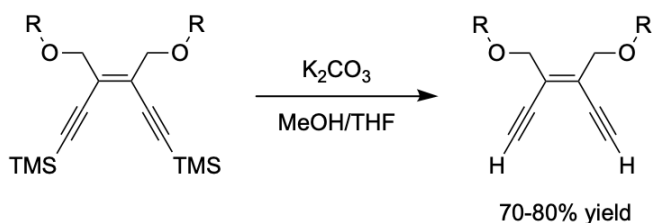
Deprotection of silyl ethynyl groups: The functionalized enediyne was dissolved in a 2:1 mixture of MeOH:THF at a concentration of approximately 0.01 M under nitrogen. To this, 2 equivalents of K$_2$CO$_3$ were added in one portion. The reaction mixture was stirred for 2

hours, and upon completion by TLC, the reaction mixture was quenched with deionized water and extracted with hexanes. The organic layers were dried with magnesium sulfate, concentrated via rotary evaporation, and used immediately without purification.
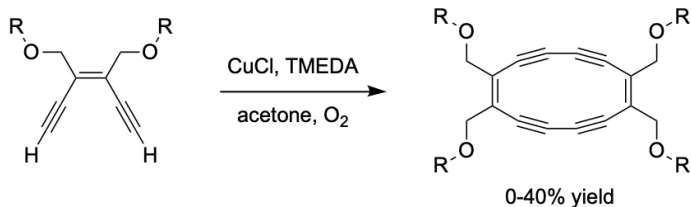
0-40% yield

Hay Coupling: The deprotected enediyne was dissolved in approximately 400 mL of acetone open to air. In a separate flask, 1 g of CuCl was dissolved in 20 mL acetone and 10 mL TMEDA. This solution was added to the dissolved enediyne in one portion. The reaction mixture was allowed to stir open to air for 3-4 days. Upon absence of starting material by TLC, the reaction was extracted with hexanes and dichloromethane, and the organic layers were dried with magnesium sulfate, concentrated via rotary evaporation, and purified with hexanes and ethyl acetate. Yields were highly variable and frequently did not yield isolable product.

55-70% yield
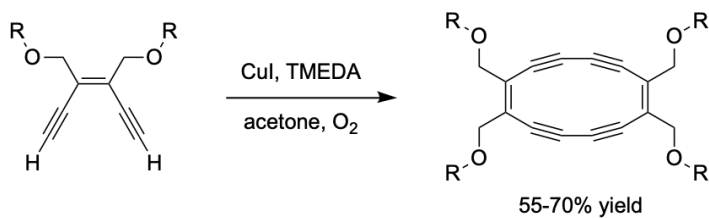
Optimized Hay Coupling: The deprotected enediyne was dissolved in approximately 400 mL of acetone open to air. In a separate flask, 1 g of CuI was dissolved in 10 mL acetone and 10 mL TMEDA. This solution was added to the dissolved enediyne in one portion. The reaction mixture was allowed to stir open to air for 1-2 days. Upon absence of starting material by TLC, the reaction was extracted with hexanes and dichloromethane, and the organic layers were dried with magnesium sulfate, concentrated via rotary evaporation, and purified with hexanes and ethyl acetate. DHAs were isolated as red or pink solids.
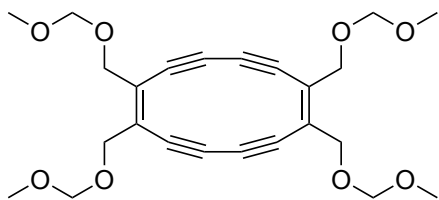
1a MOM DHA: Prepared via **Optimized Hay Coupling.** 64% yield. ^{1}H NMR (400 MHz, CDCl$_3$): δ 4.512 (s, 8H), 3.583 (s, 8H), 3.321 (s, 12H). ^{13}C NMR (101 MHz, CDCl$_3$): δ 137.641, 95.681, 95.602, 86.813, 61.823, 55.701. MS [M + Li$^+$] calculated: 451.1938, found: 451.1930. MP: 87 °C. Structure confirmed by single crystal X-ray diffraction.
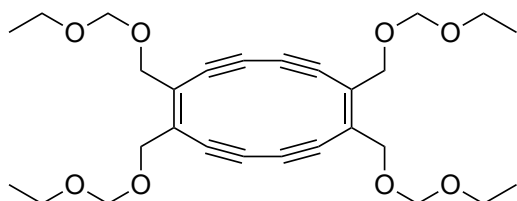
1b MOE DHA: Prepared via **Optimized Hay Coupling.** 70% yield. ^{1}H NMR (400 MHz, C$_6$D$_6$): δ 4.306 (s, 8H), 3.361 (s, 8H), 3.317 (q, J$_{HH}$ = 7.04 Hz, 8H), 1.042 (t, J$_{HH}$ = 7.04 Hz, 12H). ^{13}C NMR (101 MHz, C$_6$D$_6$): δ 138.371, 96.633, 94.253, 87.138, 63.559, 61.937, 15.253. MS [M + Li$^+$] calculated: 507.2564, found: 507.2562. MP: 73 °C.
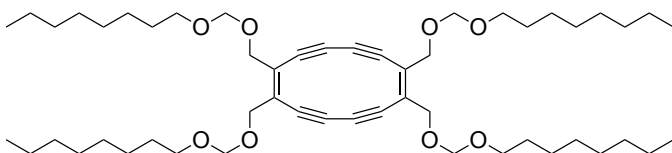
1c MOO DHA dimer: Prepared via **Optimized Hay Coupling.** 61% yield. ^{1}H NMR (400 MHz, C$_6$D$_6$): δ 4.384 (s, 8H), 3.440 (s, 8H), 3.386 (t, J$_{HH}$ = 6.57 Hz, 8H), 1.561 (m, 8H), 1.303 (m, 30H), 0.934 (t, J$_{HH}$ = 6.89 Hz, 12H). ^{13}C NMR (101 MHz, C$_6$D$_6$): δ 138.432, 96.690, 94.593, 87.251, 68.418, 62.077, 32.322, 30.158, 29.933, 29.810, 26.700, 23.145, 14.415. MS [M + Li$^+$] calculated: 843.6326, found: 843.6318. MP: 47 °C.
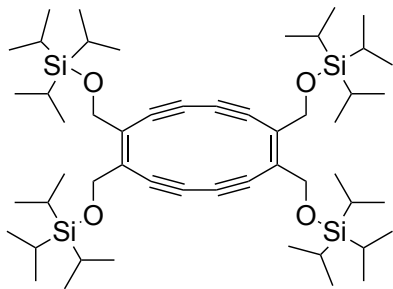
1d TIPS DHA dimer: Prepared via **Optimized Hay Coupling.** 73% yield. ^{1}H NMR (400 MHz, C$_6$D$_6$): δ 3.652 (s, 8H), 1.026 (d, J$_{HH}$ = 6.38 Hz, 72H), 0.954 (m, 12H). ^{13}C NMR (101 MHz, C$_6$D$_6$): δ 139.720, 97.012, 87.522, 59.931, 18.125, 12.196. MS [M + Li$^+$] calculated: 899.6227, found: 899.6227. Decomposition: 178 °C. Structure confirmed by single crystal X-ray diffraction.
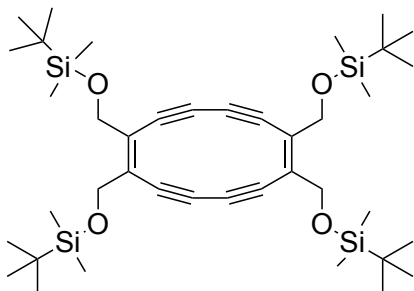
1e TBDMS DHA dimer: Prepared via **Optimized Hay Coupling.** 68% yield. ^{1}H NMR (400 MHz, C$_6$D$_6$): δ 3.635 (s, 8H), 0.847 (s, 36H), 0.026 (s, 24H). ^{13}C NMR (101 MHz, C$_6$D$_6$): δ 139.369, 96.643, 87.062, 59.032, 25.692, 18.151, -5.502. MS [M + Li$^+$] calculated: 731.4349, found: 731.4343. Decomposition: 166 °C. Structure confirmed by single crystal X-ray diffraction.
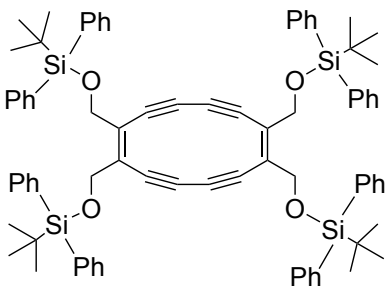
1f TBDPS DHA dimer: Prepared via **Optimized Hay Coupling.** 65% yield. ^{1}H NMR (400 MHz, CD$_2$Cl$_2$): δ 7.624 (dd, J$_{HH}$ = 6.25 Hz, 3.32 Hz, 16H), 7.185 (d, J$_{HH}$ = 1.89 Hz,

16H), 7.173 (d, J_{HH} = 2.02 Hz, 8H), 3.386 (s, 8H), 1.062 (s, 36H). ^{13}C NMR (101 MHz, CD$_2$Cl$_2$): δ 138.952, 135.868, 133.037, 130.198, 128.098, 96.297, 86.631, 59.976, 26.761, 19.331. MS [M + Li$^+$] calculated: 1227.5601, found: 1227.5602. Decomposition: 146 °C. Structure confirmed by single crystal X-ray diffraction.

Chapter 6: Summary

As introduced in Chapter 1 and demonstrated throughout this dissertation, organic materials may serve in many distinct applications. While organic materials are not intended as a replacement for silicon as high-performance semiconductors, OSCs can be applied to niche applications and offer unique properties not available from other materials. The decades of foundational research into organic semiconductors have laid the groundwork for developing structure-function relationships in organic materials and for optimizing material processing and device fabrication methods, which will continue to be crucial as these applications move forward. As many of the applications discussed herein are still in their early stages, the need for effective syntheses and rapid screening techniques are paramount. The materials covered in this dissertation are varied, with examples from several classes of molecules for which different properties are sought. Despite these differences, all of them benefit from optimization of synthetic schemes and crystal engineering to gain desired material and solid-state properties.

Chapter 2 demonstrates a series of heteroacenes and functionalization methods to these molecules, observing the resulting changes in crystal packing and optical and energetic properties with various substituents. Structure-function relationships begin to be developed for this class, particularly in regard to changing the energy levels of these materials in preparation to further employ them for singlet fission applications. Using well-established synthetic routes, a wide range of derivatives were examined, and their optical and energetic properties were evaluated. Further evaluation of the heteroacene chromophores should be centered on determining which derivatives undergo singlet fission, and identifying any relationships between crystal packing and propensity towards efficient fission. From there, the crystal engineering techniques employed for other acenes may be applied to produce additional derivatives with optimal crystal packing.

Using this foundation, the heteroacenes of Chapter 2 were functionalized with ligand groups for a hybrid organic singlet fission material-quantum dot system intended to improve the performance of silicon photovoltaics. A concise synthetic route is described, and five heteroacene carboxylic acids are presented as the basis of Chapter 3. Computational and experimental data on their energetic levels is provided, and we begin to examine trends in their predicted singlet fission properties. It is anticipated that the

energy levels are such that these materials could undergo efficient endothermic singlet fission and transfer the produced triplets to lead sulfide quantum dots, which would then emit low energy photons to be more efficiently utilized by a silicon solar cell, allowing power conversion efficiencies above the Shockley-Queisser limit to be obtained. Collaborator data demonstrating further proof of concept of this system is eagerly awaited, along with data on energy levels of the singlet fission process. Not only is it key to develop materials with the desired energy levels (which the derivatives described in Chapter 3 appear to exhibit from computational data), but the resulting ligand coverage on quantum dots must also be considered, which is crucial to a high output of photons from this system. The delicate interplay between desired energy levels, ability to efficiently transfer triplets, and possibility for sufficient ligand coverage must be carefully balanced. Further data on these variables from collaborators will help inform future derivatives.

In Chapter 4, the heteroacenes are yet again functionalized with additional substituents to obtain specific properties. In this case, a trialkylsilyl group fused to the core induced a crystal packing motif that produces pairs of isolated molecules that are strongly coupled to each other, while remaining physically and electronically separated from other pairs. Materials that exhibit this crystal packing are predicted to undergo singlet fission to produce isolated triplet pairs, and collaborators are conducting further study on these molecules to examine triplet lifetimes and the suitability of such compounds for eventual quantum computing applications.

Finally, Chapter 5 describes the synthesis and characterization of octadehydro[12]annulenes, unambiguously demonstrating the formal antiaromaticity of these molecules. An effective synthesis is reported, from which six derivatives and four crystal structures were obtained. All six derivatives exhibit surprisingly stability in solution and the solid-state, and the crystal packing indicates strong electronic coupling in multiple derivatives. One of the potential benefits of antiaromatic molecules is the obtainment of a LUMO level that may allow air-stable n-type semiconductor operation, though the typically low stability of such materials has been a barrier to exploring them further. As such, the preparation of six stable derivatives suggests exciting possibilities for future study, and the strong electronic couplings found in these dehydroannulenes supports their potential utility. This chapter demonstrates the early-stage work of crystal engineering on

this core molecule and is expected to provide a robust foundation for the design of future derivatives. Developing synthetic strategies that utilize routes other than the mucobromic acid route described here will permit a wider range of derivatives to be investigated and will allow more detailed structure-function relationships to be elucidated. The primary goals for future derivatives are lowered LUMO levels to reach the range for air-stable n-type operation and inducing packing that yields edge-to-edge interactions between adjacent cores. Utilizing a wider range of substituents to the core will be crucial towards realizing these goals.

Future work for these projects is expected to continue to rely on ever-improving structure-function relationships and synthetic optimization. As synthetic methods develop, more varied solubilizing groups and core substituents may be explored, and more thorough relationships between structure and resulting properties may be developed. The understanding of these relationships provides the basis for the future of small-molecule organic semiconductors; as the field moves towards niche applications such as those employing singlet fission or integrated organic/inorganic devices, the ability to rationally design and rapidly synthesize compounds that exhibit specific properties is paramount.

In conclusion, this dissertation demonstrates the benefit of developing structure-function relationships for core molecules such that they can be readily tuned for specialized applications. The importance of simple and scalable synthetic routes is emphasized, and effective syntheses to various functionalized materials are reported. The materials described herein are investigated with different functionalizations, and the resulting optical, energetic, and electronic properties are shown. The work in this dissertation demonstrates the importance of iterative synthesis and evaluation towards developing effective organic materials.

References

Chapter 1 References

[1] T. L. Jester, *Progress in Photovoltaics: Research and Applications* **2002**, *10*, 99-106.

[2] T. W. Kelley, P. F. Baude, C. Gerlach, D. E. Ender, D. Muyres, M. A. Haase, D. E. Vogel, S. D. Theiss, *Chem. Mater.* **2004**, *16*, 4413-4422.

[3] S. E. Root, S. Savagatrup, A. D. Printz, D. Rodriquez, D. J. Lipomi, *Chem. Rev.* **2017**, *117*, 6467-6499.

[4] S.-S. Sun, L. R. Dalton, **2008**.

[5] C. Canali, C. Jacoboni, F. Nava, G. Ottaviani, A. Alberigi-Quaranta, *Phys. Rev. B* **1975**, *12*, 2265-2284.

[6] G. Giri, E. Verploegen, S. C. B. Mannsfeld, S. Atahan-Evrenk, D. H. Kim, S. Y. Lee, H. A. Becerril, A. Aspuru-Guzik, M. F. Toney, Z. Bao, *Nature* **2011**, *480*, 504-508.

[7] G. Horowitz, *Adv. Mater.* **1998**, *10*, 365-377.

[8] Y. Sun, Y. Liu, D. Zhu, *J. Mater. Chem.* **2005**, *15*, 53-65.

[9] J. L. Brédas, J. P. Calbert, D. A. da Silva Filho, J. Cornil, *Proc. Natl. Acad. Sci.* **2002**, *99*, 5804.

[10] J. E. Anthony, A. Facchetti, M. Heeney, S. R. Marder, X. Zhan, *Adv. Mater.* **2010**, *22*, 3876-3892.

[11] V. Coropceanu, J. Cornil, D. A. da Silva Filho, Y. Olivier, R. Silbey, J.-L. Brédas, *Chem. Rev.* **2007**, *107*, 926-952.

[12] R. A. Marcus, *Reviews of Modern Physics* **1993**, *65*, 599-610.

[13] E. F. Valeev, V. Coropceanu, D. A. da Silva Filho, S. Salman, J.-L. Brédas, *J. Am. Chem. Soc.* **2006**, *128*, 9882-9886.

[14] M. D. Curtis, J. Cao, J. W. Kampf, *J. Am. Chem. Soc.* **2004**, *126*, 4318-4328.

[15] C. D. Sheraw, T. N. Jackson, D. L. Eaton, J. E. Anthony, *Adv. Mater.* **2003**, *15*, 2009-2011.

[16] J. E. Anthony, J. S. Brooks, D. L. Eaton, S. R. Parkin, *J. Am. Chem. Soc.* **2001**, *123*, 9482-9483.

[17] C. Teixeira da Rocha, K. Haase, Y. Zheng, M. Löffler, M. Hambsch, S. C. B. Mannsfeld, *Advanced Electronic Materials* **2018**, *4*, 1800141.

[18] H. Ebata, T. Izawa, E. Miyazaki, K. Takimiya, M. Ikeda, H. Kuwabara, T. Yui, *J. Am. Chem. Soc.* **2007**, *129*, 15732-15733.

[19] aW. Wei, C. Yang, J. Mai, Y. Gong, L. Yan, K. Zhao, H. Ning, S. Wu, J. Gao, X. Gao, G. Zhou, X. Lu, J. M. Liu, *J. Mater. Chem. C* **2017**, *5*, 10652-10659; bJ. Mai, N. Tang, W. He, Z. Zou, C. Luo, A. Zhang, Z. Fan, S. Wu, M. Zeng, J. Gao, G. Zhou, X. Lu, J. M. Liu, *Nanoscale Research Letters* **2019**, *14*, 169.

[20] A. Bashir, A. Heck, A. Narita, X. Feng, A. Nefedov, M. Rohwerder, K. Müllen, M. Elstner, C. Wöll, *Phys. Chem. Chem. Phys.* **2015**, *17*, 21988-21996.

[21] J.-L. Bredas, *Mater. Horizons* **2014**, *1*, 17-19.

[22] R. Mondal, C. Tönshoff, D. Khon, D. C. Neckers, H. F. Bettinger, *J. Am. Chem. Soc.* **2009**, *131*, 14281-14289.

[23] J. E. Anthony, *Angew. Chem. Int. Ed.* **2007**, *47*, 452-483.

[24] F. C. Spano, *Acc. Chem. Res.* **2010**, *43*, 429-439.

[25]   H. Fidder, J. Knoester, D. A. Wiersma, *Chem. Phys. Lett.* **1990**, *171*, 529-536.

[26]   J. E. Anthony, *Chem. Rev.* **2006**, *106*, 5028-5048.

[27]   G. C. Dacey, I. M. Ross, *Bell System Technical Journal* **1955**, *34*, 1149-1189.

[28]   Z. A. Lamport, H. F. Haneef, S. Anand, M. Waldrip, O. D. Jurchescu, *J. Appl. Phys.* **2018**, *124*, 071101.

[29]   aH. Sirringhaus, *Adv. Mater.* **2014**, *26*, 1319-1335; bL. Torsi, M. Magliulo, K. Manoli, G. Palazzo, *Chem. Soc. Rev.* **2013**, *42*, 8612-8628.

[30]   A. Rao, R. H. Friend, *Nature Reviews Materials* **2017**, *2*, 17063.

[31]   Y. Cui, H. Yao, L. Hong, T. Zhang, Y. Tang, B. Lin, K. Xian, B. Gao, C. An, P. Bi, W. Ma, J. Hou, *National Science Review* **2020**, *7*, 1239-1246.

[32]   H. Lee, C. Park, D. H. Sin, J. H. Park, K. Cho, *Adv. Mater.* **2018**, *30*, 1800453.

[33]   W. Shockley, H. J. Queisser, *J. Appl. Phys.* **1961**, *32*, 510-519.

[34]   N. J. L. K. Davis, J. R. Allardice, J. Xiao, A. J. Petty, N. C. Greenham, J. E. Anthony, A. Rao, *The Journal of Physical Chemistry Letters* **2018**, *9*, 1454-1460.

[35]   R. C. Johnson, R. E. Merrifield, *Physical Review B* **1970**, *1*, 896-902.

[36]   C. K. Yong, A. J. Musser, S. L. Bayliss, S. Lukman, H. Tamura, O. Bubnova, R. K. Hallani, A. Meneau, R. Resel, M. Maruyama, S. Hotta, L. M. Herz, D. Beljonne, J. E. Anthony, J. Clark, H. Sirringhaus, *Nat. Commun.* **2017**, *8*, 15953.

[37]   S. R. Yost, J. Lee, M. W. B. Wilson, T. Wu, D. P. McMahon, R. R. Parkhurst, N. J. Thompson, D. N. Congreve, A. Rao, K. Johnson, M. Y. Sfeir, M. G. Bawendi, T. M. Swager, R. H. Friend, M. A. Baldo, T. Van Voorhis, *Nature Chemistry* **2014**, *6*, 492.

[38]   W.-L. Chan, M. Ligges, X. Y. Zhu, *Nat. Chem.* **2012**, *4*, 840-845.

[39]   M. B. Smith, J. Michl, *Annu. Rev. Phys. Chem.* **2013**, *64*, 361-386.

[40]   D. L. Dexter, *J. Lumin.* **1979**, *18-19*, 779-784.

[41]   B. Ehrler, K. P. Musselman, M. L. Böhm, R. H. Friend, N. C. Greenham, *Appl. Phys. Lett.* **2012**, *101*, 153507.

[42]   M. Tabachnyk, B. Ehrler, S. Gélinas, M. L. Böhm, B. J. Walker, K. P. Musselman, N. C. Greenham, R. H. Friend, A. Rao, *Nature Materials* **2014**, *13*, 1033.

[43]   N. J. Thompson, M. W. B. Wilson, D. N. Congreve, P. R. Brown, J. M. Scherer, Thomas S. Bischof, M. Wu, N. Geva, M. Welborn, T. V. Voorhis, V. Bulović, M. G. Bawendi, Marc A. Baldo, *Nature Materials* **2014**, *13*, 1039.

[44]   aA. Stanger, *Chem. Commun.* **2009**, 1939-1947; bT. M. Krygowski, M. K. Cyrañski, Z. Czarnocki, G. Häfelinger, A. R. Katritzky, *Tetrahedron* **2000**, *56*, 1783-1796.

[45]   A. Stanger, *The Journal of Organic Chemistry* **2006**, *71*, 883-893.

[46]   R. Breslow, J. Brown, J. J. Gajewski, *J. Am. Chem. Soc.* **1967**, *89*, 4383-4390.

[47]   R. Breslow, *Acc. Chem. Res.* **1973**, *6*, 393-398.

[48]   E. Hückel, *Zeitschrift fur Physik* **1931**, *70*, 204.

[49]   M. Rosenberg, C. Dahlstrand, K. Kilså, H. Ottosson, *Chem. Rev.* **2014**, *114*, 5379-5425.

[50]   Z. Chen, C. S. Wannere, C. Corminboeuf, R. Puchta, P. v. R. Schleyer, *Chem. Rev.* **2005**, *105*, 3842-3888.

[51]   aJ. A. Pople, K. G. Untch, *J. Am. Chem. Soc.* **1966**, *88*, 4811-4815; bJ. Anthony, A. M. Boldi, C. Boudon, J.-P. Gisselbrecht, M. Gross, P. Seiler, C. B. Knobler, F. Diederich, *Helv. Chim. Acta* **1995**, *78*, 797-817.

[52]   V. I. Minkin, B. J. Simkin, M. N. Glukhovtsev, *Aromaticity and antiaromaticity : Electronic and structural aspects*, Wiley, New York, **1994**.

[53]   P. v. R. Schleyer, C. Maerker, A. Dransfeld, H. Jiao, N. J. R. van Eikema Hommes, *J. Am. Chem. Soc.* **1996**, *118*, 6317-6318.

[54]   Z. Chen, T. Heine, P. v. R. Schleyer, D. Sundholm, **2004**.

[55]   P. v. R. Schleyer, M. Manoharan, Z.-X. Wang, B. Kiran, H. Jiao, R. Puchta, N. J. R. van Eikema Hommes, *Org. Lett.* **2001**, *3*, 2465-2468.

[56]   I. Alkorta, I. Rozas, J. Elguero, *Tetrahedron* **2001**, *57*, 6043-6049.

[57]   A. Stanger, *J. Am. Chem. Soc.* **1991**, *113*, 8277-8280.

[58]   J. Zhang, S. Sarrafpour, T. E. Haas, P. Müller, S. W. Thomas, *J. Mater. Chem.* **2012**, *22*, 6182-6189.

[59]   R. Breslow, F. W. Foss, Jr., *Journal of Physics Condensed Matter* **2008**, *20*, 374104.

[60]   A. M. Zeidell, L. Jennings, C. K. Frederickson, Q. Ai, J. J. Dressler, L. N. Zakharov, C. Risko, M. M. Haley, O. D. Jurchescu, *Chem. Mater.* **2019**, *31*, 6962-6970.

[61]   A. Minsky, A. Y. Meyer, M. Rabinovitz, *Tetrahedron* **1985**, *41*, 785-791.

[62]   T. Nishinaga, T. Ohmae, K. Aita, M. Takase, M. Iyoda, T. Arai, Y. Kunugi, *Chem. Commun.* **2013**, *49*, 5354-5356.

[63]   H. Usta, C. Risko, Z. Wang, H. Huang, M. K. Deliomeroglu, A. Zhukhovitskiy, A. Facchetti, T. J. Marks, *J. Am. Chem. Soc.* **2009**, *131*, 5586-5608.

[64]   J. Cao, G. London, O. Dumele, M. von Wantoch Rekowski, N. Trapp, L. Ruhlmann, C. Boudon, A. Stanger, F. Diederich, *J. Am. Chem. Soc.* **2015**, *137*, 7178-7188.

[65]   C. K. Frederickson, L. N. Zakharov, M. M. Haley, *J. Am. Chem. Soc.* **2016**, *138*, 16827-16838.

[66]   J. E. Anthony, D. L. Eaton, S. R. Parkin, *Org. Lett.* **2002**, *4*, 15-18.

[67]   H. Ottosson, *Nat. Chem.* **2012**, *4*, 969-971.

[68]   M. D. Peeks, J. Q. Gong, K. McLoughlin, T. Kobatake, R. Haver, L. M. Herz, H. L. Anderson, *The Journal of Physical Chemistry Letters* **2019**, *10*, 2017-2022.

Chapter 2 References

[1]   J. E. Anthony, *Chem. Rev.* **2006**, *106*, 5028-5048.

[2]   J. E. Anthony, *Angew. Chem. Int. Ed.* **2007**, *47*, 452-483.

[3]   J. E. Anthony, J. S. Brooks, D. L. Eaton, S. R. Parkin, *J. Am. Chem. Soc.* **2001**, *123*, 9482-9483.

[4]   M. M. Payne, S. A. Odom, S. R. Parkin, J. E. Anthony, *Org. Lett.* **2004**, *6*, 3325-3328.

[5]   M. M. Payne, S. R. Parkin, J. E. Anthony, C.-C. Kuo, T. N. Jackson, *J. Am. Chem. Soc.* **2005**, *127*, 4986-4987.

[6]   J. E. Anthony, D. L. Eaton, S. R. Parkin, *Org. Lett.* **2002**, *4*, 15-18.

[7]   aJ. J. Burdett, C. J. Bardeen, *Acc. Chem. Res.* **2013**, *46*, 1312-1320; bG. B. Piland, C. J. Bardeen, *The Journal of Physical Chemistry Letters* **2015**, *6*, 1841-1846.

[8]   aF. Valiyev, W.-S. Hu, H.-Y. Chen, M.-Y. Kuo, I. Chao, Y.-T. Tao, *Chem. Mater.* **2007**, *19*, 3018-3026; bM. L. Tang, A. D. Reichardt, T. Siegrist, S. C. B. Mannsfeld, Z. Bao, *Chem. Mater.* **2008**, *20*, 4669-4676.

[9]   J. Chen, S. Subramanian, S. R. Parkin, M. Siegler, K. Gallup, C. Haughn, D. C. Martin, J. E. Anthony, *J. Mater. Chem.* **2008**, *18*, 1961-1969.

[10]   P. Wagner, *Acta Crystallographica Section E* **2006**, *62*, o5745--o5747.

[11]   C. F. Macrae, *J. Appl. Crystallogr.* **2020**, *53*, 226--235.

[12]   C. R. Swartz, S. R. Parkin, J. E. Bullock, J. E. Anthony, A. C. Mayer, G. G. Malliaras, *Org. Lett.* **2005**, *7*, 3163-3166.

[13]   S. Subramanian, S. K. Park, S. R. Parkin, V. Podzorov, T. N. Jackson, J. E. Anthony, *J. Am. Chem. Soc.* **2008**, *130*, 2706-2707.

[14]   K. Reichenbächer, H. I. Süss, J. Hulliger, *Chem. Soc. Rev.* **2005**, *34*, 22-30.

[15]   aC.-T. Chien, T.-C. Chiang, M. Watanabe, T.-H. Chao, Y. J. Chang, Y.-D. Lin, H.-K. Lee, C.-Y. Liu, C.-H. Tu, C.-H. Sun, T. J. Chow, *Tetrahedron Lett.* **2013**, *54*, 903-906; bA. Naibi Lakshminarayana, A. Ong, C. Chi, *J. Mater. Chem. C* **2018**, *6*, 3551-3563.

[16]   aK. C. Caster, C. G. Keck, R. D. Walls, *The Journal of Organic Chemistry* **2001**, *66*, 2932-2936; bE. Masson, M. Schlosser, *Eur. J. Org. Chem.* **2005**, *2005*, 4401-4405; cT. Dohi, T. Nakae, N. Takenaga, T. Uchiyama, K.-i. Fukushima, H. Fujioka, Y. Kita, *Synthesis* **2012**, *44*, 1183--1189; dT. Yamakado, S. Takahashi, K. Watanabe, Y. Matsumoto, A. Osuka, S. Saito, *Angew. Chem. Int. Ed.* **2018**, *57*, 5438-5443.

[17]   aT. Brotin, J. Waluk, J.-P. Desvergne, H. Bouas-Laurent, J. Michl, *Photochem. Photobiol.* **1992**, *55*, 335-347; bJ.-P. Desvergne, T. Brotin, D. Meerschaut, G. Clavier, F. Placin, J.-L. Pozzo, H. Bouas-Laurent, *New J. Chem.* **2004**, *28*, 234-243.

[18]   aB. Yalcouye, A. Berthelot-Bréhier, D. Augros, A. Panossian, S. Choppin, M. Chessé, F. Colobert, F. R. Leroux, *Eur. J. Org. Chem.* **2016**, *2016*, 725-732; bM. Blanchot, D. A. Candito, F. Larnaud, M. Lautens, *Org. Lett.* **2011**, *13*, 1486-1489.

[19]   aA. Tripathi, C. Prabhakar, *J. Mol. Struct.* **2020**, *1203*, 127397; bK. Niimi, E. Miyazaki, I. Osaka, K. Takimiya, *Synthesis* **2012**, *44*, 2102-2106.

[20]   M. Watanabe, W.-T. Su, Y. J. Chang, T.-H. Chao, Y.-S. Wen, T. J. Chow, *Chemistry, an Asian journal.* **2013**, *8*, 60--64.

[21]   M. J. Frisch, G. W. Trucks, H. B. Schlegel, G. E. Scuseria, M. A. Robb, J. R. Cheeseman, G. Scalmani, V. Barone, G. A. Petersson, H. Nakatsuji, X. Li, M. Caricato, A. V. Marenich, J. Bloino, B. G. Janesko, R. Gomperts, B. Mennucci, H. P. Hratchian, J. V. Ortiz, A. F. Izmaylov, J. L. Sonnenberg, Williams, F. Ding, F. Lipparini, F. Egidi, J. Goings, B. Peng, A. Petrone, T. Henderson, D. Ranasinghe, V. G. Zakrzewski, J. Gao, N. Rega, G. Zheng, W. Liang, M. Hada, M. Ehara, K. Toyota, R. Fukuda, J. Hasegawa, M. Ishida, T. Nakajima, Y. Honda, O. Kitao, H. Nakai, T. Vreven, K. Throssell, J. A. Montgomery Jr., J. E. Peralta, F. Ogliaro, M. J. Bearpark, J. J. Heyd, E. N. Brothers, K. N. Kudin, V. N. Staroverov, T. A. Keith, R. Kobayashi, J. Normand, K. Raghavachari, A. P. Rendell, J. C. Burant, S. S. Iyengar, J. Tomasi, M. Cossi, J. M. Millam, M. Klene, C. Adamo, R. Cammi, J. W. Ochterski, R. L. Martin, K. Morokuma, O. Farkas, J. B. Foresman, D. J. Fox, Wallingford, CT, **2016**.

[22]   A. Troisi, G. Orlandi, J. E. Anthony, *Chem. Mater.* **2005**, *17*, 5024-5031.

[23]   aH. L. Stern, A. J. Musser, S. Gelinas, P. Parkinson, L. M. Herz, M. J. Bruzek, J. Anthony, R. H. Friend, B. J. Walker, *Proc. Natl. Acad. Sci.* **2015**, *112*, 7656; bN.

J. L. K. Davis, J. R. Allardice, J. Xiao, A. J. Petty, N. C. Greenham, J. E. Anthony, A. Rao, *J. Phys. Chem. Lett.* **2018**, *9*, 1454-1460.

[24]   N. Nishimura, V. Gray, J. R. Allardice, Z. Zhang, A. Pershin, D. Beljonne, A. Rao, *ACS Materials Letters* **2019**, *1*, 660-664.

[25]   M. K. Bera, P. Pal, S. Malik, *J. Mater. Chem. C* **2020**, *8*, 788-802.

[26]   W. Z. Yuan, P. Lu, S. Chen, J. W. Y. Lam, Z. Wang, Y. Liu, H. S. Kwok, Y. Ma, B. Z. Tang, *Adv. Mater.* **2010**, *22*, 2159-2163.

Chapter 3 References

[1]   aN. J. Thompson, M. W. B. Wilson, D. N. Congreve, P. R. Brown, J. M. Scherer, Thomas S. Bischof, M. Wu, N. Geva, M. Welborn, T. V. Voorhis, V. Bulović, M. G. Bawendi, Marc A. Baldo, *Nature Materials* **2014**, *13*, 1039; bB. Ehrler, K. P. Musselman, M. L. Böhm, R. H. Friend, N. C. Greenham, *Appl Phys Lett* **2012**, *101*, 153507.

[2]   N. J. L. K. Davis, J. R. Allardice, J. Xiao, A. J. Petty, N. C. Greenham, J. E. Anthony, A. Rao, *The Journal of Physical Chemistry Letters* **2018**, *9*, 1454-1460.

[3]   M. Tabachnyk, B. Ehrler, S. Gélinas, M. L. Böhm, B. J. Walker, K. P. Musselman, N. C. Greenham, R. H. Friend, A. Rao, *Nature Materials* **2014**, *13*, 1033.

[4]   S. R. Yost, J. Lee, M. W. B. Wilson, T. Wu, D. P. McMahon, R. R. Parkhurst, N. J. Thompson, D. N. Congreve, A. Rao, K. Johnson, M. Y. Sfeir, M. G. Bawendi, T. M. Swager, R. H. Friend, M. A. Baldo, T. Van Voorhis, *Nature Chemistry* **2014**, *6*, 492.

[5]   N. J. L. K. Davis, J. R. Allardice, J. Xiao, A. J. Petty, N. C. Greenham, J. E. Anthony, A. Rao, *Journal of Physical Chemistry Letters* **2018**, *9*, 1454-1460.

[6]   M. L. Tang, A. D. Reichardt, P. Wei, Z. Bao, *J Am Chem Soc* **2009**, *131*, 5264-5273.

[7]   F. Valiyev, W.-S. Hu, H.-Y. Chen, M.-Y. Kuo, I. Chao, Y.-T. Tao, *Chem Mater* **2007**, *19*, 3018-3026.

[8]   Ł. Struk, J. Sośnicki, *Synthesis* **2012**, *44*, 735-746.

[9]   M. L. Tang, A. D. Reichardt, T. Okamoto, N. Miyaki, Z. Bao, *Adv Funct Mater* **2008**, *18*, 1579-1585.

[10]   M. J. Frisch, G. W. Trucks, H. B. Schlegel, G. E. Scuseria, M. A. Robb, J. R. Cheeseman, G. Scalmani, V. Barone, G. A. Petersson, H. Nakatsuji, X. Li, M. Caricato, A. V. Marenich, J. Bloino, B. G. Janesko, R. Gomperts, B. Mennucci, H. P. Hratchian, J. V. Ortiz, A. F. Izmaylov, J. L. Sonnenberg, Williams, F. Ding, F. Lipparini, F. Egidi, J. Goings, B. Peng, A. Petrone, T. Henderson, D. Ranasinghe, V. G. Zakrzewski, J. Gao, N. Rega, G. Zheng, W. Liang, M. Hada, M. Ehara, K. Toyota, R. Fukuda, J. Hasegawa, M. Ishida, T. Nakajima, Y. Honda, O. Kitao, H. Nakai, T. Vreven, K. Throssell, J. A. Montgomery Jr., J. E. Peralta, F. Ogliaro, M. J. Bearpark, J. J. Heyd, E. N. Brothers, K. N. Kudin, V. N. Staroverov, T. A. Keith, R. Kobayashi, J. Normand, K. Raghavachari, A. P. Rendell, J. C. Burant, S. S. Iyengar, J. Tomasi, M. Cossi, J. M. Millam, M. Klene, C. Adamo, R. Cammi, J. W. Ochterski, R. L. Martin, K. Morokuma, O. Farkas, J. B. Foresman, D. J. Fox, Wallingford, CT, **2016**.

[11]   S. Hirata, M. Head-Gordon, *Chem Phys Lett* **1999**, *314*, 291-299.

Chapter 4 References

[1]   aA. Steane, *Rep. Prog. Phys.* **1998**, *61*, 117-173; bL. Gyongyosi, S. Imre, *Computer Science Review* **2019**, *31*, 51-71.

[2]   D. P. DiVincenzo, *Fortschritte der Physik* **2000**, *48*, 771-783.

[3]   J. H. Jefferson, M. Fearn, D. L. J. Tipton, T. P. Spiller, *Physical Review A* **2002**, *66*, 042328.

[4]   L. Petit, H. G. J. Eenink, M. Russ, W. I. L. Lawrie, N. W. Hendrickx, S. G. J. Philips, J. S. Clarke, L. M. K. Vandersypen, M. Veldhorst, *Nature* **2020**, *580*, 355-359.

[5]   aA. Gaita-Ariño, F. Luis, S. Hill, E. Coronado, *Nat. Chem.* **2019**, *11*, 301-309; bC.-J. Yu, S. von Kugelgen, D. W. Laorenza, D. E. Freedman, *ACS Central Science* **2021**, *7*, 712-723.

[6]   M. J. Frisch, G. W. Trucks, H. B. Schlegel, G. E. Scuseria, M. A. Robb, J. R. Cheeseman, G. Scalmani, V. Barone, G. A. Petersson, H. Nakatsuji, X. Li, M. Caricato, A. V. Marenich, J. Bloino, B. G. Janesko, R. Gomperts, B. Mennucci, H. P. Hratchian, J. V. Ortiz, A. F. Izmaylov, J. L. Sonnenberg, Williams, F. Ding, F. Lipparini, F. Egidi, J. Goings, B. Peng, A. Petrone, T. Henderson, D. Ranasinghe, V. G. Zakrzewski, J. Gao, N. Rega, G. Zheng, W. Liang, M. Hada, M. Ehara, K. Toyota, R. Fukuda, J. Hasegawa, M. Ishida, T. Nakajima, Y. Honda, O. Kitao, H. Nakai, T. Vreven, K. Throssell, J. A. Montgomery Jr., J. E. Peralta, F. Ogliaro, M. J. Bearpark, J. J. Heyd, E. N. Brothers, K. N. Kudin, V. N. Staroverov, T. A. Keith, R. Kobayashi, J. Normand, K. Raghavachari, A. P. Rendell, J. C. Burant, S. S. Iyengar, J. Tomasi, M. Cossi, J. M. Millam, M. Klene, C. Adamo, R. Cammi, J. W. Ochterski, R. L. Martin, K. Morokuma, O. Farkas, J. B. Foresman, D. J. Fox, Wallingford, CT, **2016**.

Chapter 5 References

[1]   J. Anthony, F. Diederich, C. B. Knobler, *Angewandte Chemie International Edition in English* **1993**, *32*, 406-409.

[2]   T. Nishinaga, N. Nodera, Y. Miyata, K. Komatsu, *The Journal of Organic Chemistry* **2002**, *67*, 6091-6096.

[3]   J. Anthony, A. M. Boldi, C. Boudon, J.-P. Gisselbrecht, M. Gross, P. Seiler, C. B. Knobler, F. Diederich, *Helv Chim Acta* **1995**, *78*, 797-817.

[4]   J. Jusélius, D. Sundholm, *Phys Chem Chem Phys* **2001**, *3*, 2433-2437.

[5]   M. Klues, G. Witte, *CrystEngComm* **2018**, *20*, 63-74.

[6]   J. L. Brédas, J. P. Calbert, D. A. da Silva Filho, J. Cornil, *PNAS* **2002**, *99*, 5804.

[7]   V. Coropceanu, J. Cornil, D. A. da Silva Filho, Y. Olivier, R. Silbey, J.-L. Brédas, *Chem Rev* **2007**, *107*, 926-952.

[8]   T. Nishinaga, T. Kawamura, K. Komatsu, *The Journal of Organic Chemistry* **1997**, *62*, 5354-5362.

[9]   E. L. Spitler, C. A. Johnson, M. M. Haley, *Chem Rev* **2006**, *106*, 5344-5386.

[10]   O. M. Behr, G. Eglinton, A. R. Galbraith, R. A. Raphael, *Journal of the Chemical Society (Resumed)* **1960**, 3614-3625.

[11]   W. B. Wan, S. C. Brand, J. J. Pak, M. M. Haley, *Chemistry – A European Journal* **2000**, *6*, 2044-2052.

[12] G. Eglinton, A. R. Galbraith, *Journal of the Chemical Society (Resumed)* **1959**, 889-896.

[13] W. Setaka, S. Kanai, C. Kabuto, M. Kira, *Chem Lett* **2006**, *35*, 1364-1365.

[14] Q. Zhou, P. J. Carroll, T. M. Swager, *The Journal of Organic Chemistry* **1994**, *59*, 1294-1301.

[15] T. Takeda, K. Inukai, K. Tahara, Y. Tobe, *The Journal of Organic Chemistry* **2011**, *76*, 9116-9121.

[16] I. Hisaki, K. Osaka, N. Ikenaka, A. Saeki, N. Tohnai, S. Seki, M. Miyata, *Crystal Growth & Design* **2016**, *16*, 714-721.

[17] S.-i. Kato, N. Takahashi, H. Tanaka, A. Kobayashi, T. Yoshihara, S. Tobita, T. Yamanobe, H. Uehara, Y. Nakamura, *Chem Eur J* **2013**, *19*, 12138-12151.

[18] C. Boudon, J. P. Gisselbrecht, M. Gross, J. Anthony, A. M. Boldi, R. Faust, T. Lange, D. Philp, J. D. Van Loon, F. Diederich, *J Electroanal Chem* **1995**, *394*, 187-197.

[19] A. Minsky, A. Y. Meyer, M. Rabinovitz, *Tetrahedron* **1985**, *41*, 785-791.

[20] S. Miao, P. v. R. Schleyer, J. I. Wu, K. I. Hardcastle, U. H. F. Bunz, *Org Lett* **2007**, *9*, 1073-1076.

[21] X. Gao, Y. Hu, *Journal of Materials Chemistry C* **2014**, *2*, 3099-3117.

[22] H. Usta, C. Risko, Z. Wang, H. Huang, M. K. Deliomeroglu, A. Zhukhovitskiy, A. Facchetti, T. J. Marks, *J Am Chem Soc* **2009**, *131*, 5586-5608.

[23] K. L. Horvath, N. L. Magann, M. J. Sowden, M. G. Gardiner, M. S. Sherburn, *J Am Chem Soc* **2019**, *141*, 19746-19753.

[24] Z. M. Nimmo, J. F. Halonski, L. E. Chatkewitz, D. D. Young, *Bioorg Chem* **2018**, *76*, 326-331.

[25] A. Stanger, *J Am Chem Soc* **1991**, *113*, 8277-8280.

[26] Q. B. Ai, V.; Ryno, S. M.; Jarolimek, K.; Sornberger, P.; Smith, A.; Haley, M. M.; Anthony, J. E.; Risko, C., *The Journal of Chemical Physics* **2021**, *154*.

[27] M. J. Frisch, G. W. Trucks, H. B. Schlegel, G. E. Scuseria, M. A. Robb, J. R. Cheeseman, G. Scalmani, V. Barone, G. A. Petersson, H. Nakatsuji, X. Li, M. Caricato, A. V. Marenich, J. Bloino, B. G. Janesko, R. Gomperts, B. Mennucci, H. P. Hratchian, J. V. Ortiz, A. F. Izmaylov, J. L. Sonnenberg, Williams, F. Ding, F. Lipparini, F. Egidi, J. Goings, B. Peng, A. Petrone, T. Henderson, D. Ranasinghe, V. G. Zakrzewski, J. Gao, N. Rega, G. Zheng, W. Liang, M. Hada, M. Ehara, K. Toyota, R. Fukuda, J. Hasegawa, M. Ishida, T. Nakajima, Y. Honda, O. Kitao, H. Nakai, T. Vreven, K. Throssell, J. A. Montgomery Jr., J. E. Peralta, F. Ogliaro, M. J. Bearpark, J. J. Heyd, E. N. Brothers, K. N. Kudin, V. N. Staroverov, T. A. Keith, R. Kobayashi, J. Normand, K. Raghavachari, A. P. Rendell, J. C. Burant, S. S. Iyengar, J. Tomasi, M. Cossi, J. M. Millam, M. Klene, C. Adamo, R. Cammi, J. W. Ochterski, R. L. Martin, K. Morokuma, O. Farkas, J. B. Foresman, D. J. Fox, Wallingford, CT, **2016**.

[28] R. Gershoni-Poranne, A. Stanger, *Chemistry – A European Journal* **2014**, *20*, 5673-5688.

Vita
Emma Katherine Holland
Born in Memphis, TN

Education:
B.S. in Chemistry, University of Kentucky, Lexington, KY, 2016

Professional Experience:
Registered Patent Agent, June 2021

Office of Technology Commercialization Fellow, University of Kentucky, Lexington, KY, July 2019-December 2020

Honors and Awards:
University of Kentucky Singletary Scholarship, 2012-2016

Student Government Association Professional Development Scholarship, University of Kentucky, February 2021

Publications:
D. G. Bossanyi, M. Matthiesen, S. Wang, J. A. Smith, R. C. Kilbride, J. D. Shipp, D. Chekulaev, E. K. Holland, J. E. Anthony, J. Zaumseil, A. J. Musser, J. Clark. "Emissive spin-0 triplet-pairs are a direct product of triplet-triplet annihilation in pentacene single crystals and anthradithiophene films." *Nature Chemistry.* **2021**, *13*, 163-171.

C. Tyznik, J. Lee, J. Sorli, X. Liu, E. K. Holland, C. S. Day, J. E. Anthony, Y.-L. Loo, Z. V. Vardeny, O. D. Jurchescu. "Photocurrent in Metal-Halide Perovskite/Organic Semiconductor Heterostructures: Impact of Microstructure on Charge Generation Efficiency." *ACS Applied Materials and Interfaces*. **2021**, *13 (8),* 10231-10238.

E. G. Bittle, S. Engmann, A. J. Biacchi, E. K. Holland, J. E. Anthony. "Triplet exciton impact on photocurrent in diF TES ADT single crystal transistors." *Proceedings SPIE* 11476, Organic and Hybrid Field-Effect Transistors XIX, **2020**, 114760J.

A. M. Zeidell, T. Ren, D. S. Filston, H. F. Iqbal, E. K. Holland, J. D. Bourland, J. E. Anthony, O. D. Jurchescu. "Organic Field-Effect Transistors as Flexible, Tissue-Equivalent Radiation Dosimeters in Medical Applications." *Advanced Science*. **2020**, *7*, 2001522.

H. F. Iqbal, E. K. Holland, J. E. Anthony, O. D. Jurchescu. "Real-time monitoring of trap dynamics reveals the electronic states that limit charge transport in crystalline organic semiconductors." *Materials Horizons*. **2020**, *7*, 2390-2398.

M. J. Bruzek, E. K. Holland, A. K. Hailey, S. R. Parkin, Y.-L. Loo, J. E. Anthony. "Exploring Crystal Structure in Eythyne-Substituted Pentacenes, and Their Elaboration into Crystalline Dehydro[18]annulenes." *Helvetica Chimica Acta*. **2019**, *102*, e1900026.